Development and Applications of Gold Nanoparticles and Elastomeric Polymers as Biomaterials

A DISSERTATION
SUBMITTED TO THE FACULTY OF
UNIVERSITY OF MINNESOTA
BY

Allison M. Siehr

IN PARTIAL FULFILLMENT OF THE REQUIREMENTS
FOR THE DEGREE OF
DOCTOR OF PHILOSOPHY

Dr. Wei Shen, Adviser, Dr. Ronald A. Siegel, Co-Adviser

July 2021

Acknowledgments

First of all, this work would not have been possible without financial support from the GAANN fellowship, the NIH biotechnology training grant, and the NIH Institutes for Molecular Virology training grant.

I would like to acknowledge my advisor, Prof. Wei Shen, whose support, guidance, and technical advice made this work possible. I would also like to acknowledge my co-advisor, Prof. Ronald Siegel—my experience working in his lab during my undergraduate studies motivated me to pursue graduate school.

I would like to acknowledge Prof. Louis Mansky for all of his support. The virology studies completed in this thesis would not have been possible without him.

I would like to acknowledge Prof. Chun Wang for his support throughout my graduate studies.

I would also like to thank Prof. Joachim Mueller and Prof. Wei Zhang for their technical advice and support.

I want to extend my gratitude to my lab-mates, colleagues, and friends for their support and technical guidance. First, I would like to thank Dr. Bin Xu and Dr. Mengen Zhang from Prof. Shen's lab, who provided an immeasurable amount of support. I want to thank Krutika Harish Jain, Dr. Anasuya Sahoo, Dr. Davin Rautiola, and the many other members of Prof. Siegel's lab for their guidance. I want to extend my gratitude to the many members of Prof. Mansky's lab who provided advice and support along the way, including Dr. Megan Roth, Dr. Nathaniel Talledge, Dr. Emily Julik, Dr. Rayna Addabbo, Nora Willkomm, and many others. I would also like to thank Dr. Ali Crampton, Dr. Benjamin

Brummel, and Dr. Bin Xu for their advice on this thesis. Additionally, I would like to extend my thanks to the many other colleagues and friends that supported me along the way.

I would also like to recognize my parents, Susan and Brian, and my siblings for their support. I would particularly like to thank my sister Meagan for all of her guidance through this journey.

Abstract

This thesis is focused on the development and applications of two different types of biomaterials: nanoparticles and polymers. In chapter 1, I briefly review these biomaterials. In chapter 2, we develop gold nanoparticles (GNPs) that can be driven to either self-assemble or remain colloidally stable using coiled-coil protein interactions. Control over the GNP self-assembly or stability is critical for specific biomedical applications. In chapter 3, we use the self-assembling GNPs to inhibit human immunodeficiency virus type-1 (HIV-1) by adding a targeting ligand for HIV-1. However, we found our GNPs are weak inhibitors of HIV-1. Methods to improve the inhibitor design are then discussed. In chapter 4, a biomaterials-based approach is used to elucidate the structures of HIV-1 and human T-cell leukemia virus type-1 (HTLV-1). A GNP immunolabeling strategy is used to identify HIV-1 and HTLV-1 envelope proteins, critical for viral entry and targets for vaccine development. However, the immunolabelling strategy was not robust, and alternative methods to study envelope proteins are discussed. Lastly, in chapter 5, a novel elastomeric polymer is evaluated for biomedical applications. PLA-PβMδVL-PLA polymers were synthesized in this work and shown to exhibit elastomeric properties. Next, the polymers were found to be biocompatible and biodegradable both *in vitro* and *in vivo*. Overall, this thesis demonstrates the development and applications of both gold nanoparticles and elastomeric polymers as biomaterials.

Table of Contents

List of Tables

List of Figures

Chapter 1: Introduction

1.1 Biomaterials

Biomaterials, defined as "any matter, construct, or surface that interacts with biological systems", are indispensable to the field of medicine today.[1] Both natural and synthetic materials can be used as biomaterials to support, enhance, or replace natural biological functions or damaged tissues.[2] Biomaterials have a broad range of applications, including medical implants, methods to promote healing of tissues or tissue regeneration, molecular probes and imaging, biosensors, and drug delivery systems, among others.[1] The different types of biomaterials include polymers, ceramics, metals, and composites.[1,3] Additionally, nanoscale biomaterials are used in many biomedical applications. For example, nanoparticles are used as molecular probes and biosensors to aid in imaging and therapies.[4] Polymers are used for multiple applications, including medical implants, tissue engineering scaffolds, and drug delivery devices.[5,6] This thesis is focused on the development and application of nanoscale and polymeric biomaterials for different biomedical applications—this chapter provides a brief overview of these biomaterials.

1.2 Nanoparticles

Nanoparticles, one example of nanoscale biomaterials, are particles with overall dimensions on the nanoscale or under 100 nanometers.[7] Nanoparticles have properties distinct from bulk materials due to their small size. For example, nanoparticles have enhanced biological mobility over bulk materials, and therefore, are useful in biomedical applications as contrast agents or for directed drug and gene delivery.[7,8] Metal nanoparticles—especially gold nanoparticles (GNPs)—offer high thermal and chemical stability, a small size-to-volume ratio, biocompatibility, a high photothermal conversion

rate, tunable optical and electronic properties, and are easily synthesized and functionalized.[7,9,10] Due to these properties, GNPs have been used for biomedical applications ranging from controlled drug delivery, phototherapy, imaging, biosensors, and diagnostic tools.[9,11–15]

GNPs can be readily functionalized with antibodies, proteins, nucleic acids, aptamers, or other targeting ligands.[13] Functionalized GNPs have been used for many applications, namely labeling or targeting cells and proteins of interest, and therapies, like plasmonic photothermal therapies (PPTT), that require site-specific targeting.[16] One example of surface functionalization is antibody conjugation. Antibody-conjugated GNPs have been used for biomedical imaging of cancer cells, imaging of animals through computerized tomography, and gold immunolabelling to detect proteins of interest.[17–19] Most recently, antibody-labeled GNPs have been used to detect severe acute respiratory syndrome coronavirus 2 (SARS-CoV-2).[20,21] Additionally, GNPs have been functionalized with proteins and nucleic acids for gene and drug delivery applications.[4,22,23] Protein- and DNA-conjugated GNPs have also been designed for viral inhibition,[24–26] further discussed in Chapter 3 of this thesis.

Surface functionalized GNPs have also been used to design colorimetric-based diagnostic and detection methods.[27–34] These colorimetric-based methods use the unique size-dependent optical and electronic properties offered by self-assembled GNPs.[27,30,35] GNPs can be designed to self-assemble through physical and chemical cues.[36–40] Previous work used polymer-polymer, DNA-oligonucleotide hybridization, and protein-ligand mediated recognition events to guide GNP self-assembly.[38–42] The resulting size-dependent

optical properties of GNPs have been used to explore ligand-receptor interactions and detect viruses, biomolecules, and circulating tumor cells.[31,35,43–45]

Overall, GNPs are highly versatile and therefore have been widely used in biomedical applications. For many applications, control over the GNP behavior is critical. Self-assembly is desired in various applications, such as biosensing and diagnostics, whereas imaging and targeted delivery require colloidally stable GNPs, as discussed in Chapter 2.[13] In this thesis, we demonstrate control over the GNP behavior using protein-protein interactions to drive either self-assembly or colloidal stability of GNPs. We then use the protein-conjugated GNPs that exhibit self-assembly to inhibit human immunodeficiency virus type-1 (HIV-1) by adding a targeting ligand for HIV-1. Lastly, we use a biomaterials-based approach to elucidate the structures of HIV-1 and human T-cell leukemia virus type-1 (HTLV-1), in which GNPs were used as probes to identify critical structural proteins.

1.3 Polymeric biomaterials

Like nanoscale biomaterials, polymers have been used as biomaterials, finding applications in medical devices, tissue engineering scaffolds, and drug delivery devices.[5,46,47] For example, the synthetic polymers poly(lactic-co-glycolic acid) (PLGA), poly(hydroxyethyl methacrylate) (pHEMA), and poly(ethylene glycol) (PEG) have been used for decades as drug delivery devices, intraocular lens materials, contact lenses, or scaffolds for tissue engineering.[48] Natural polymers have also been used for many biomedical applications, such as hydroxyapatite and chitosan.[49] Ultimately, polymer choice depends on factors such as the anatomical location, mechanical requirements, and cell types required for an implant or device.[5,6] An additional consideration is

biocompatibility, which is defined as "the ability of a material to function with an appropriate host response in a specific application." [50] Biocompatibility is not an inherent property of a material but should be evaluated for specific biological applications.[6] Biodegradability is another property that should be considered when selecting polymers.[51] For tissue engineering and drug delivery applications, a polymeric scaffold should provide support while tissue is regenerated or while the drug is being delivered.[6,51] Once the scaffold or implant has fulfilled its function, biodegradation is ideal, as it eliminates the need for a second surgery to remove implanted material, reducing hospitalization time and health care costs and minimizing the risk of infection and complications during a second surgery.[51,52]

Some of the most commonly used polymers for medical applications that exhibit biocompatibility and biodegradability are poly(α-hydroxy esters), including poly(lactic acid) (PLA), poly(glycolic acid) (PGA), poly(lactic acid-*co*-glycolic acid) (PLGA), and poly(caprolactone) (PCL).[53] PLA has been used for bone fixation screws and drug delivery applications. PGA and PLGA copolymers have been used for DEXON commercial sutures and skin graft materials.[53] PCL has been used for long-term contraceptive devices and drug delivery devices.[53,54] Overall, these polymers have been used in many FDA-approved devices.[53] However, one drawback of poly(α-esters) is their rigid mechanical properties. Mechanical properties are critical for tissue engineering applications and biomedical implants, and the mechanical properties of an implant should be similar to that of the host tissue, as mechanical mismatch can be detrimental to an implant's success.[53–56] Therefore, for applications like soft tissue engineering, polymers should exhibit flexibility and elastomeric properties (i.e., they are highly stretchable and can completely recover after

being stretched).[57] A more detailed description of the mechanical properties required for soft tissue engineering and elastomers currently used for such applications appears in Chapter 5 of this thesis.

The development of polymers that combine these characteristics—biodegradability, biocompatibility, and biomechanical compatibility—is essential for biomedical applications. Part of this thesis (Chapter 5) is dedicated to synthesizing a novel polymer, poly(lactic acid)-*co*-poly(β-methyl-δ-valerolactone)-*co*-poly(lactic acid) (PLA-PβMδVL-PLA), that exhibits these properties and evaluating its use as an implantable biomaterial. Additionally, a second elastomer, PLA-*co*-poly(methyl-caprolactone)-*co*-PLA, was explored for potential use in biomedical applications (reported in Appendix 3).

1.4 Overview of thesis

Overall, this thesis focuses on developing and applying two different biomaterials: gold nanoparticles and elastomeric polymers. The second chapter of this thesis focuses on developing protein-conjugated GNPs that exhibit controlled self-assembly and stability. The third chapter utilizes the self-assembling GNPs developed in Chapter 2 and assesses their ability to inhibit viral infection. The fourth chapter develops a biomaterials-based approach to elucidate the structure of viruses using a GNP immunolabelling method. Lastly, the fifth chapter of this thesis reports the synthesis and evaluation of a novel polymer as an implantable material.

Chapter 2: Colloidal Stability versus Self-Assembly of Nanoparticles Controlled by Coiled-Coil Protein Interactions

This work was reproduced from the following reference with permission from the Royal Society of Chemistry: Siehr, A.; Xu, B.; Siegel, R.A.; and Shen, W. "Colloidal stability *versus* self-assembly of nanoparticles controlled by coiled-coil protein interactions." *RSC Advances.* 2019, (15) 7122-7126. doi.org/10.1039/C9SM01314H.

Synopsis

Orientational discrimination of biomolecular recognition is exploited here as a molecular engineering tool to regulate nanoparticle self-assembly or stability. Nanoparticles are conjugated with the heterodimerizing coiled-coils, A and B, which associate in parallel orientation—simply flipping the orientation of one coiled-coil results in either self-assembling or colloidally stable nanoparticles.

2.1 Introduction

Controlled nanoparticle self-assembly or stability is essential for technological development in nanomedicine and nanobiotechnology.[58,59] For example, nanoparticles used for computerized tomography imaging and plasmonic photothermal therapies are required to be highly stable under physiological conditions.[13,16] Controlled nanoparticle self-assembly has been extensively exploited to develop therapeutic methods for viral inhibition and detection technologies for biomolecules, viruses, and circulating tumor cells.[24,30–32,35,43]

Currently, the most common approach to stabilize nanoparticles is surface modification with poly(ethylene glycol) (PEG),[60–62] although approaches using zwitterionic ligands have also been proposed.[63] Self-assembly of nanoparticles into larger

hierarchical structures is typically engineered on the basis of hydrophobic interactions, electrostatic interactions, and biomolecular recognition.[64–69] Biomolecular recognition modes, such as DNA hybridization,[28,41,70] coiled-coil self-assembly,[71–73] streptavidin-biotin interactions,[74] and antibody-antigen interactions,[75] have high specificity, and have been extensively used to direct nanoparticle self-assembly. Hybridization of DNA complementary strands and self-assembly of some protein domains, such as coiled-coils, exhibit orientational discrimination,[76] making these modes more versatile in controlling self-assembly and forming nanoparticle superstructures.

Here, we report that orientational discrimination of biomolecular recognition can be used as a molecular tool to control nanoparticle self-assembly and stability. In a model system, we conjugated a pair of heterodimerizing coiled-coil proteins, "A" and "B",[77] on gold nanoparticles (GNPs). While the A protein was conjugated to the GNPs in a fixed orientation, the B protein was conjugated at either its N-terminal or C-terminal side, providing two different orientations of this domain on the particle surface. Simply flipping the orientation of B led to two completely different particle behaviors: one orientation maintaining colloidal stability of the GNPs, and the other orientation driving GNPs into large aggregates.

2.2 Experimental Section

2.2.1 Protein synthesis, purification, and characterization

The protein sequences are shown in Table 1. The proteins cysA, Bcys, nA, and nB have been previously reported,[77,78] and cysB was constructed in the Qiagen pQE9 expression vector. Each protein was expressed in the *E.coli* strain SG13009 under control of the bacteriophage T5 promoter and purified through nickel-nitrilotriacetic acid (Ni-

NTA) metal-affinity chromatography, as previously reported.[77,78] All cysteinated proteins were purified in the presence of 1 mM TCEP to reduce disulfide bonds, and Bcys and cysB were purified in the presence of 1 mM PMSF to prevent protein degradation. Purified proteins were dialyzed against water, followed by lyophilization. The proteins were characterized by using SDS-polyacrylamide gel electrophoresis and MALDI mass spectrometry on a 5800 MALDI/TOF Mass Spectrometer (AB-SCIEx).

2.2.2 Synthesis and characterization of GNPs

The Frens-Turkevich method was used to synthesize GNPs.[79] Briefly, a solution of gold (III) trichloride (Sigma Aldrich) was prepared at a concentration of 0.1 mg mL^{-1} in water and boiled under continuous stirring with a condenser apparatus attached. A solution of trisodium citrate (Sigma Aldrich) was prepared at a concentration of 11.4 mg mL^{-1} and added quickly to the boiling gold (III) trichloride solution at a volume ratio of 1.88:100. The mixture was boiled for an additional 8 minutes, resulting in citrate-capped GNPs. The GNPs were characterized by using dynamic light scattering (DLS) and UV-Vis spectrophotometry.

2.2.3 Surface modification of GNPs with proteins

The surface of GNPs was modified with cysA and cysB (cysA-cysB GNPs) or cysA and Bcys (cysA-Bcys GNPs) through the gold-thiol reaction. The solution of each cysteinated protein (50 μM) was prepared in the presence of its non-cysteinated heterodimerizing partner (75 μM) to form heterodimers (cysA/nB, cysB/nA, Bcys/nA), so that proteins covalently conjugated on GNPs would not be closely packed. Each solution was prepared in 40 mM HEPES buffer containing 5 mM TCEP (pH 7.8) and incubated for 12 hours at 4 °C. To modify GNPs, the solutions of cysB/nA and cysA/nB or the solutions

of Bcys/nA and cysA/nB were mixed at a 1:1 ratio, and the mixture was added dropwise to the GNP suspension (1.53×10^{12} GNPs mL^{-1}) while stirring at a 1:3 ratio, followed by stirring overnight. The protein-conjugated GNPs were stored at 4ºC until further use and were characterized by using dynamic light scattering (DLS) and UV-Vis Spectrophotometry.

2.2.4 Sample preparation for examining particle self-assembly

The protein-conjugated GNP suspensions and PBS (HyClone, 1X or 0.0067 м, pH 7.4) were filtered through a 0.2-micron filter (Acrodisc). A 2 mL aliquot of each protein-conjugated GNP suspension was centrifuged at 5.6krcf for 1 hour, followed by removal of 1.7 mL of the supernatant and resuspension in 1 mL of PBS. Immediately following resuspension was the Day 0 time point. Particle self-assembly was characterized using UV-Vis Spectrophotometry, Transmission Electron Microscopy (TEM), and Small Angle X-ray Scattering (SAXS).

2.2.5 Dynamic Light Scattering

Samples were filtered through a 0.2-micron filter, and DLS was measured using a 90Plus Particle Size Analyzer (Brookhaven) at 90° scattering angle. The average hydrodynamic diameter was determined using the method of cumulants. Polydispersity values lower than 0.08 were considered to be monodisperse.

2.2.6 UV-Vis Spectrophotometry

UV-Vis spectra scanned from 350 nm to 750 nm were collected at a 600 nm min^{-1} scanning rate and a 1 nm resolution on a Cary Win 300 UV-Vis spectrophotometer (Agilent Technologies).

2.2.7 GNP size and concentration

The UV-Vis spectra revealed the size of GNPs and the concentrations of GNP suspensions according to Equations 1 and 2:[80]

$$d = \exp\left(B_1 \frac{A_{SPR}}{A_{450}} - B_2\right) \qquad \textit{Equation 1}$$

$$N = \frac{A_{450} * 10^{14}}{d^2\left[-0.295 + 1.36 exp\left(-\left(\frac{d-96.8}{78.2}\right)^2\right)\right]} \qquad \textit{Equation 2}$$

where d is the diameter in nanometers, N is the concentration of GNPs in particles mL^{-1}, A_{SPR} is the absorbance at the SPR peak (or maximum peak), A_{450} is the absorbance at 450 nm, and the constants B_1 and B_2 are 3.00 and 2.20, respectively.

2.2.8 Transmission Electron Microscopy (TEM)

Samples were prepared by dropping 20 µL of a particle suspension onto a TEM grid (carbon type B, 300 mesh grid; TedPella), incubating for 20 minutes, and removing excess liquid with a KimWipe. The TEM grids were further dried for 12 hours, and TEM images were collected on a Tecnai T12 instrument operated at 100kV.

2.2.9 Small angle x-ray scattering (SAXS)

SAXS data were collected with a Cu K_α radiation source (operated at 60 kV and 0.3 Ma) at a wavelength of 1.5409 Å on SAXSlab Ganesha (Xenocs). After a sample was incubated at room temperature for the intended time, it was pipetted up and down to ensure uniform particle suspension and loaded into a quartz capillary tube with an inner diameter of 1.3 cm. The tube was sealed with 5-minute epoxy (Loctite) and allowed to dry overnight. All spectra were collected with the x-ray beam centered near the bottom of the capillary tube, with a 2 mm centered beam stop using two aperture SAXS, and were transmission

corrected and thickness corrected to the inner diameter of the tube. Filtered PBS buffer was used as the background for protein-conjugated GNPs; the supernatant collected from a centrifuged, unmodified GNP sample was used as the background for unmodified GNPs. Collection times for SAXS measurements were 1 hour for test samples and 30 minutes for background samples. Background subtraction of all SAXS spectra was completed using JADE software.

The particle center-to-center distance d was determined from the scattering vector q according to Equation 3, where d is the interparticle distance and q is the scattering vector:[40]

$$d = \frac{2\pi}{q} \qquad \textit{Equation 3}$$

The radius of gyration was determined by a Guinier plot fit to Equation 4:[81]

$$\ln(I) \approx \ln(I_o) - \frac{R_g^2 q^2}{3} \qquad \textit{Equation 4}$$

where I is scattering intensity, I_0 is the background scattering intensity, q is the scattering vector, and R_g is the radius of gyration. PRIMUS software was used.[82] The hard-sphere radius, R, was determined from the radius of gyration according to Equation 5.[83]

$$R = \sqrt{\frac{5}{3}} R_g \qquad \textit{Equation 5}$$

2.2.10 ICP-OES and TOC analysis

To determine the concentration of proteins conjugated to the surface of GNPs, cysA-Bcys and cysA-cysB GNPs were analyzed using inductively coupled plasma-optical emission spectroscopy (ICP-OES) and total organic carbon (TOC) analyses to quantify the

concentrations of gold (corresponding to GNPs) and carbon (corresponding to proteins), respectively. 50 mL of cysA-Bcys and 50 mL of cysA-cysB GNPs were centrifuged at 16.1krcf for 70 minutes. 42.5 mL of the supernatant were removed, and samples were resuspended to 50 mL in 8M urea (pH 8.0) overnight. The above centrifugation procedure was repeated an additional 5 times to remove unbound proteins thoroughly. In the final wash, 42.5 mL of the supernatant were removed, and the remaining samples were transferred to Microcon-30 Ultra Centrifugal filters (EMD Millipore) with a 30kDa molecular weight cut-off (MWCO). The samples were then washed with Milli-Q water by centrifuging the samples at 8krcf for 20 minutes. This washing procedure was completed a total of 6 times to remove excess urea. After the final washing step, samples were resuspended in 6 mL of water, transferred to an acid-washed glass vial (QorPak vial with acid proof lid), diluted with 2.743 mL of aqua regia (an acidic solution composed of 1:3 volume-to-volume of HNO_3:HCl), heated slightly to dissolve all GNPs, and then further diluted with 18.3 mL of Milli-Q water. For ICP-OES analysis, 1 mL of this solution was transferred to a new vial (acid-washed QorPak vial with acid-proof lid), followed by dilution with 5 mL of 2% HNO_3 solution. The remainder of the original solution was used for TOC analysis. All samples were stored at 4 °C before submitting for ICP-OES and TOC analyses at the Research Analytical laboratory at the University of Minnesota. Gold concentrations were analyzed using an iCap 7600 Duo ICP-OES Analyzer. A standard curve of gold ions in solution (completed in triplicate) was used to determine the concentration of gold in the GNP solution. Total organic carbon analysis was completed using an Elementar Vario TOC cube. Five samples of cysA-Bcys GNPs and five samples of cysA-cysB GNPs were analyzed.

The mass in grams per GNP (*M*) was determined by the following:

$$M = \frac{\pi}{6}\rho D^3 \qquad \textit{Equation 6}$$

In *Equation 6* above, ρ is the density of fcc gold (19.3 $^{g}/_{cm^3}$), and D is the diameter of GNPs, as determined by UV-Vis spectrophotometry.[84–86] This value was then used to determine the number of GNPs from the gold concentration determined by ICP-OES. The number of proteins was calculated from TOC using the number of carbons per protein, assuming a 1:1 ratio of cysA to Bcys (371 carbon atoms per protein) and cysA to cysB (380 carbon atoms per protein).

2.2.11 Disassembly of self-assembled GNPs

GNPs self-assembled over 10 days were transferred to a low protein binding Eppendorf tube and heated at 80 °C for 1 hour to denature the proteins. Samples were characterized using UV-Vis spectrophotometry before and after heat treatment.

2.2.12 Effect of higher protein packing density on self-assembly of cysA-Bcys conjugated GNPs

It was expected that when the packing density of conjugated proteins on the GNP surface was too high for interparticle protein-protein heterodimerization to occur, self-assembly of cysA-Bcys conjugated GNPs would be inhibited. To test this hypothesis, surface modification of GNPs was conducted without non-cysteinated coiled-coil proteins (nA and nB), which were used to prevent an excessively dense packing. The nanoparticle behavior of these GNPs was examined over a time course of 10 days.

2.2.13 Effect of lower protein packing density on colloidal stability of cysA-cysB conjugated GNPs

It was expected that when the packing density of conjugated proteins on the GNP surface was too low for intraparticle coiled-coil heterodimerization to occur, colloidal stability of cysA-cysB conjugated GNPs would be impaired. To test this hypothesis, surface modification of GNPs was conducted in the presence of 0, 5, 25, and 50 μM β-mercaptoethanol (βME), a small thiolate that competes with thiol-mediated protein binding to the GNP surface, to reduce protein packing density. The nanoparticle behavior of the resulting GNPs was examined.

2.3 Results and Discussion

2.3.1 The molecular design of nanoparticles is expected to control nanoparticle behavior

The molecular design of the nanoparticles is illustrated in Figure 1. A and B proteins have been previously shown to heterodimerize in the parallel direction through hydrophobic and electrostatic interactions.[77] Immobilizing A and B in anti-parallel orientation on the same nanoparticle results in a parallel orientation on adjacent nanoparticles, promoting interparticle protein heterodimerization and nanoparticle self-assembly (Figure 1a). Alternatively, intraparticle protein heterodimers can form when A and B are immobilized in parallel orientation on the same nanoparticle. These coiled-coils do not bridge adjacent nanoparticles, resulting in colloidal stability (Figure 1b).

2.3.2 Synthesized GNPs are 20 nm and have low polydispersity

GNPs synthesized using the Frens-Turkevich method were characterized by dynamic light scattering (DLS) and UV-Vis spectrophotometry.[79] DLS revealed a hydrodynamic diameter of 20.5±0.7 nm with a polydispersity of 0.077±0.020. The UV-Vis

spectrum showed a characteristic maximum absorbance at 518 nm, corresponding to surface plasmon resonance (SPR) of GNPs having a diameter of 16.8 nm.[80,87] The GNP concentration was determined by the ratio of the absorbance at the SPR peak to that at 450 nm as previously reported.[80]

2.3.3 Proteins are conjugated to the GNP surface through gold-thiol interactions

Two non-cysteinated coiled-coil proteins, nA and nB, and three cysteinated coiled-coil proteins, cysA, cysB, and Bcys, were synthesized (see Table 1 for protein sequences). In the cysteinated proteins, the cysteine residue was incorporated near the N-terminus of the coiled-coil domain in cysB and cysA, and near the C-terminus in Bcys. By combining heterodimers of a non-cysteinated protein with its cysteinated partner, solutions were prepared containing nA and cysB (nA/cysB), nA and Bcys (nA/Bcys), and cysA and nB (cysA/nB) in the presence of a reducing agent, tris(2-carboxyethyl)phosphine (TCEP) (75 μM and 50 μM for non-cysteinated and cysteinated proteins, respectively). These heterodimers were then conjugated to the GNPs by gold-thiol reaction. Specifically, the solutions of nA/Bcys and cysA/nB or the solutions of nA/cysB and cysA/nB were mixed at a 1:1 ratio, and the mixture was added to a GNP suspension (1.53×10^{12} GNPs mL^{-1}) at a 1:3 ratio while stirring. Solutions of coiled-coil protein heterodimers, in which one partner was non-cysteinated, were used in order to prevent an excessively dense packing of covalently conjugated proteins, which may inhibit interparticle coiled-coil heterodimerization. The GNPs modified with cysA and Bcys (denoted here as cysA-Bcys GNPs) had the two coiled-coils conjugated on the surface in anti-parallel orientation, and the GNPs modified with cysA and cysB (denoted as cysA-cysB GNPs) had the two coiled-coils on the surface in parallel orientation (Figure 1).

2.3.4 Protein-conjugated GNPs are characterized using DLS, UV-Vis, and SAXS

Immediately following protein conjugation, DLS revealed hydrodynamic diameters of approximately 35 nm for both cysA-Bcys and cysA-cysB conjugated GNPs (Table 2). The change in hydrodynamic diameter from 20 nm for unmodified GNPs to 35 nm for coiled-coil conjugated GNPs suggests an approximately 7.5 nm thick corona. This is largely consistent with the 6.3 nm length of the coiled-coil rods as previously reported[88] plus the additional small linker sequence length of ~1.6 nm (see SAXS data in section 2.3.6 for further information). The polydispersity of the protein-conjugated GNPs was the same as that of unmodified GNPs, suggesting that aggregation did not occur during or after the conjugation procedure. Colloidal stability of GNPs at this step was most likely maintained by the large excess of unbound coiled-coils in the solution, which dominated strand exchange with the noncovalently immobilized coiled-coils on the GNPs and prevented interparticle coiled-coil interactions. The protein-conjugated GNPs were also characterized using UV-Vis spectrophotometry. The maximum SPR peak of the UV-Vis spectra shifted from 518 nm for unmodified GNPs to 524 nm for both cysA-Bcys and cysA-cysB conjugated GNPs (Table 2) (Figure 2). The red-shift in the SPR peak was due to the presence of proteins bound to the GNP surface and suggests that surface modification had occurred.[87]

2.3.5 Molecular design results in colloidally stable or self-assembling nanoparticles

Nanoparticle behavior after reducing the concentration of unbound coiled-coils in solution was then examined. Specifically, each suspension was centrifuged, and 85% of the supernatant was removed, followed by resuspension in PBS at 50% of the starting suspension volume. The samples were then examined over a time course of 10 days to

observe the behavior of the protein-conjugated GNPs. The difference between the two types of protein-conjugated GNPs was first observed visually (Figure 3a). On day 0, both suspensions of protein-conjugated GNPs appeared red, as expected for non-aggregated GNPs.[87] On day 10, visible dark red and purple aggregates in a clear background were observed for the cysA-Bcys conjugated GNPs, but no visible aggregates or color change was observed for the cysA-cysB conjugated GNPs. Representative UV-Vis spectra of cysA-Bcys conjugated GNPs also exhibited a red-shift and broadening of the SPR peak over 10 days, while those of cysA-cysB conjugated GNPs remained almost unchanged (Figure 3b). It has been reported that a red-shift in the SPR peak of the UV-vis spectra occurs when GNPs form aggregates.[27,37,80,87,89] The differences in the UV-Vis spectra between the two particle samples confirm that the cysA-Bcys conjugated GNPs aggregated readily and the cysA-cysB conjugated GNPs were highly stable. As a final confirmation of disparate aggregation behaviors, TEM images (Figure 4) revealed that the cysA-Bcys conjugated GNPs formed large aggregates after 5 days, while the cysA-cysB conjugated GNPs did not form aggregates at 5 or 10 days.

2.3.6 Particle-to-particle distance is consistent with coiled-coil heterodimerization

The structure of cysA-Bcys conjugated GNP aggregates was probed using Small Angle X-Ray Scattering (SAXS). SAXS spectra on day 10 (Figure 5) exhibited a maximum peak at a q-value of 0.234 nm^{-1} for cysA-Bcys conjugated GNPs corresponding to a d-spacing of 26.8 nm (Equation 3).[40,42] SAXS spectra for cysA-cysB conjugated GNPs were of low amplitude and did not exhibit any distinct peaks on day 10 (Figure 5). Size of the unmodified GNPs was also characterized using SAXS. Fitting the scattering data to the Guinier function (Figure 6) yielded a radius of gyration (R_g) of 6.66±0.11 nm,

corresponding to a hard sphere radius of 8.60 nm (Equations 4 and 5) and a diameter of 17.2 nm, which lies between the previous estimates of particle diameter derived from DLS (20.5 nm) and SPR (16.8 nm). The particle center-to-center distance of 26.8 nm and the particle radius of 8.60 nm suggest that the surface-to-surface distance between neighboring particles was 9.6 nm. This value is largely consistent with that expected for GNP aggregates mediated by interparticle coiled-coil heterodimerization, because these coiled-coil A and B rods are 6.3 nm long[88] and both cysA and Bcys contain a few amino acid residues between cysteine and the coiled-coil domains (suggesting a linker length of 1.6 nm).

2.3.7 Self-assembly of cysA-Bcys GNPs is due to protein-protein interactions

To demonstrate that self-assembly of cysA-Bcys conjugated GNPs was due to protein-protein interactions, GNPs self-assembled for 10 days were treated at 80 °C to denature the proteins. The UV-Vis spectrum of the resulting GNP suspension was substantially different from that of the aggregated GNPs on day 10, but essentially indistinguishable from that of the pre-aggregation suspension on day 0 (Figure 7a), indicating that the self-assembled GNPs could be disassembled upon protein denaturation. The same treatment had no effect on the colloidal stability of cysA-cysB conjugated GNPs (Figure 7b).

2.3.8 ICP-OES and TOC allow for characterization of the packing density

The packing density, or the number of proteins conjugated to the GNP surface, may affect the behavior of the nanoparticles. Many different methods have been used to characterize packing density, including inductively coupled plasma-mass spectrometry (ICP-MS), nuclear magnetic resonance (NMR), circular dichroism spectroscopy (CD), and

microscale thermogravimetric analysis (μ-TGA).[90–93] NMR and CD require GNP concentrations to be measured before determining the concentration of proteins, whereas ICP-MS and μ-TGA can quantify both protein and GNP concentration simultaneously. While ICP-MS and μ-TGA are optimal methods for determining the protein packing density, access to such instrumentation is limited. Therefore, we used two simultaneous methods to determine the packing density: inductively coupled plasma-optical emission spectrometry (ICP-OES) and total organic carbon analysis (TOC). ICP-OES was used to determine the concentration of gold corresponding to the GNPs, while TOC was used to determine the concentration of carbon, which corresponds to the protein concentration.

Protein-conjugated GNPs were first washed to remove excess proteins and unbound, non-cysteinated proteins (nA and nB) followed by ICP and TOC analysis. The two proteins (either cysA/Bcys or cysA/cysB) were conjugated to the GNPs at a 1:1 ratio, and, therefore, it was assumed that the ratio of these two proteins was 1:1. From these analyses, we found that cysA-Bcys GNPs and cysA-cysB GNPs had packing densities of 826±305 and 562±136, respectively (Figure 8). The packing density on cysA-Bcys GNPs was slightly higher than that of cysA-cysB GNPs. This may be due to the extra linker structure found in the cysB protein (see Table 1 for protein sequences). However, these values were statistically insignificant (Student's t-test, p-value>0.1), which suggests that differences in packing density are not responsible for differences in nanoparticle behavior.

2.3.9 Changing the packing density changes the nanoparticle behaviors

The inclusion of non-cysteinated partners when the GNPs were conjugated with cysA, and Bcys was necessary to provide an optimal spacing between the latter coiled proteins, such that they could form interparticle coiled-coil heterodimers. In the absence

of nA and nB, the packing density of cysA and Bcys was too high to permit cysA-Bcys coiled-coil bridges between GNPs, and hence impaired GNP aggregation (Figure 9). On the other hand, reducing the packing density of cysA-cysB by conjugating these proteins in the presence of β-mercaptoethanol, a small thiolate that competes with thiol-mediated protein binding to the GNP surface, eliminated GNP colloidal stability (promoted aggregation: Figure 10), most likely due to the increased distance between cysA and cysB conjugates, and hence prevention of intraparticle cysA-cysB heterodimerization. These observations highlight the importance of both protein orientation and packing density on particle behavior.

2.4 Discussion

While previous work introduced the use of coiled-coil proteins to drive self-assembly of inorganic nanoparticles into larger hierarchical structures[71–73], this is the first demonstration that orientational discrimination of biomolecular recognition can control self-assembly versus colloidal stability of inorganic nanoparticles. In particular, colloidal stability has not been shown previously to be controlled by coiled-coil proteins. The tendency of cysA-Bcys conjugated GNPs to self-assemble and the colloidal stability of cysA-cysB conjugated GNPs as observed in these experiments suggest that interparticle and intraparticle coiled-coil heterodimerization is energetically favorable for these two types of GNPs, respectively, verifying the material design illustrated in Figure 1.

The cysA-Bcys conjugated GNPs could be stored in a colloidally stable state in the presence of a large excess of solubilized coiled-coils, and their aggregation could be triggered upon reduction in the concentration of solubilized coiled-coils. These might be important properties in practical applications, such as detection technologies.[30–32,35,43]

Future studies may include investigation of the aggregation kinetics of cysA-Bcys conjugated GNPs as a function of nanoparticle or solubilized coiled-coil concentration. In addition, the coiled-coils presented here can be easily modified with bioactive ligands or targeting moieties for both self-assembling and stable nanoparticles, via protein engineering. Thus, this approach can be tuned to create colloidally stable or self-assembling nanoparticles while maintaining the bioactivity and targeting ability of the ligands.

2.5 Conclusions

In summary, we report that orientational discrimination of biomolecular recognition can be harnessed as a molecular engineering tool to control nanoparticle self-assembly and stability. We demonstrated that when a pair of heterodimerizing coiled-coils was conjugated on the nanoparticle surface, simply flipping the orientation of one of the coiled-coils led to two completely different particle properties: one driving the nanoparticles into large aggregates and the other keeping them colloidally stable.

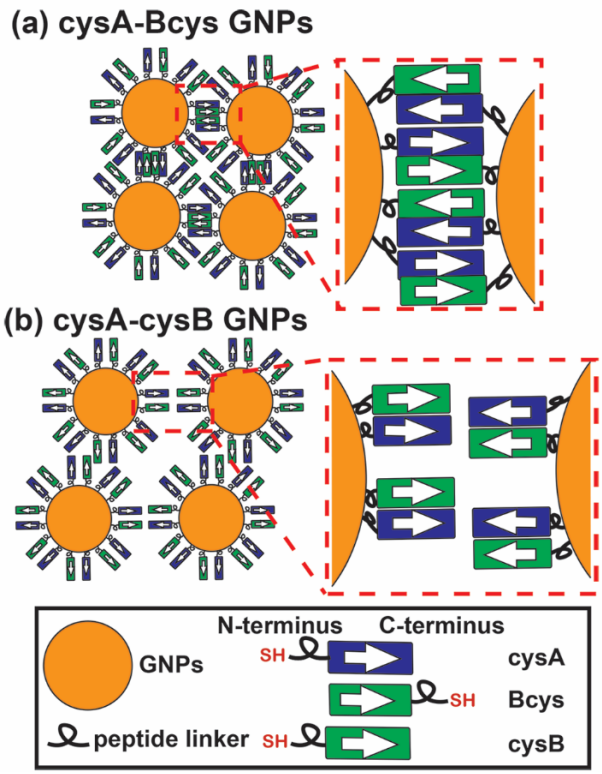

Figure 1. The molecular design of the nanoparticles. (a) When coiled-coils A and B are conjugated on nanoparticles in anti-parallel orientation, A and B on adjacent particles are parallel and form interparticle heterodimers that promote nanoparticle self-assembly. (b) When coiled-coils A and B are conjugated on nanoparticles in parallel orientation, A and B on the same particle form intraparticle heterodimers, and the nanoparticles remain colloidally stable.

Table 1. Sequences of proteins used here. The coiled-coil domains are highlighted in blue. The cysteine residues are highlighted in red.

Bcys	MRGSHHHHHHGSDDDDKWASGTSG**DLKNKVAQLKRKVRSLKD KAAELKQEVSRLENEIEDLKAKIGD**HVAPRDTSMGG**C**
cysB	MRGSHHHHHHGSDDDDKASSGSG**C**SGSGTSGTSG**DLKNKVAQ LKRKVRSLKDKAAELKQEVSRLENEEDLKAKI**GDHVAPRDTSW
cysA	MRGSHHHHHHGSDDDDKASSGSG**C**SGSGTSG**DLENEVAQLERE VRSLEDEAAELEQKVSRLKNEIEDLKAEIGD**HVAPRDTSW
nA	MRGSHHHHHHGSDDDDKASG**DLENEVAQLEREVRSLEDEAAEL EQKVSRLKNEIEDLKAEIGD**HVAPRDSW
nB	MRGSHHHHHHGSDDDDKASGTSG**DLKNKVAQLKRKVRSLKDK AAELKQEVSRLENEIEDLKAKIGD**HVAPRDTSW

Table 2. DLS and UV-Vis results. The properties of unmodified and protein-conjugated GNPs characterized with DLS and UV-Vis spectrophotometry.

	Dynamic Light Scattering		***UV-Vis spectrophotometry***
Sample	**Size (nm)**	**Polydispersity**	**Maximum SPR (nm)**
Unmodified GNPs	20.5±0.7	0.077±0.02	518
cysA-Bcys GNPs	35.2±0.4	0.069±0.018	524
cysA-cysB GNPs	35.7±0.4	0.077±0.009	524

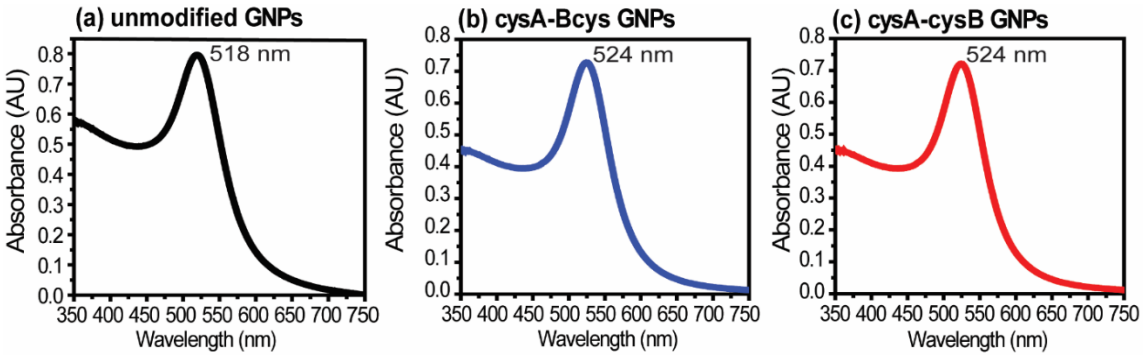

Figure 2. UV-Vis spectra of GNPs. The UV-Vis spectra for unmodified GNPs (a), cysA-Bcys conjugated GNPs (b), and cysA-cysB conjugated GNPs (c) reveal a red-shift of the maximum SPR peak from 518 nm for unmodified GNPs to 524 nm for protein-conjugated GNPs.

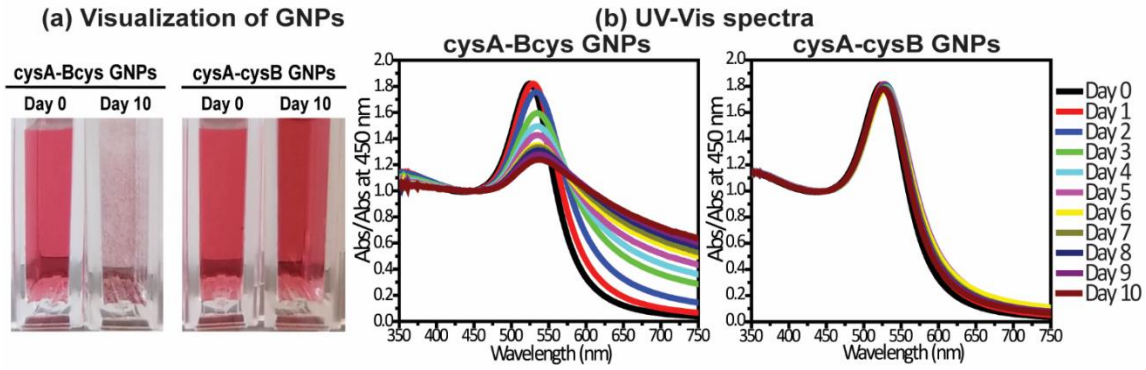

Figure 3. Self-assembly vs. stability of GNPs. (a) The suspension of cysA-Bcys conjugated GNPs exhibited visible large aggregates on day 10, while the suspension of cysA-cysB conjugated GNPs did not show any visible changes. (b) UV-Vis spectra of protein-conjugated GNPs over a time course of 10 days. The spectra of cysA-Bcys conjugated GNPs showed a broadening and a red-shift in the maximum SPR peak over time (left). The spectra of cysA-cysB conjugated GNPs remained almost unchanged (right). All spectra are normalized to the absorbance at 450 nm.

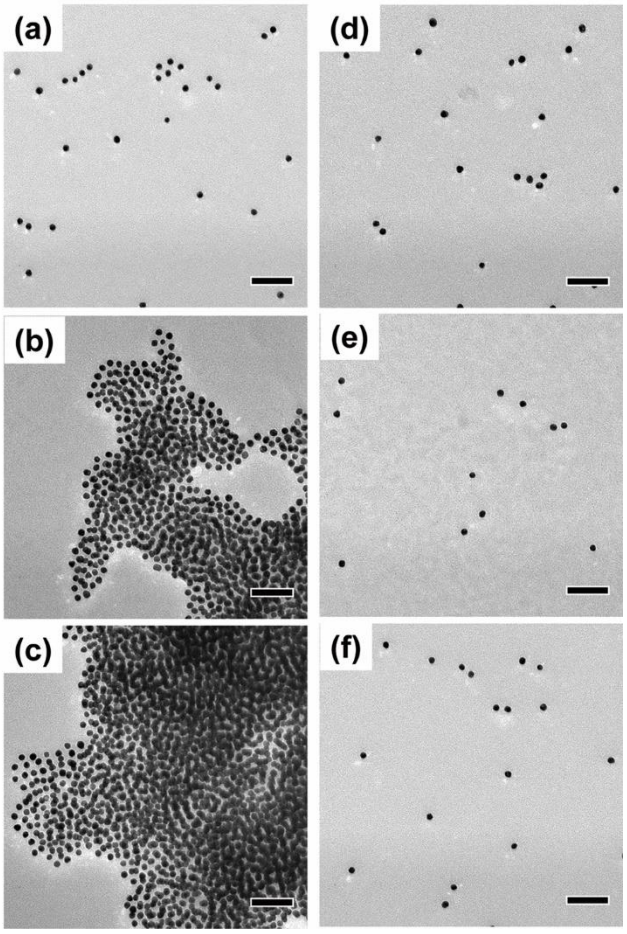

Figure 4. TEM images of self-assembled vs. stable GNPs. TEM images of cysA-Bcys GNPs (a-c) and cysA-cysB GNPs (d-f) on day 0 (a, d), day 5 (b, e), and day 10 (c, f). Scale bar is 100 nm.

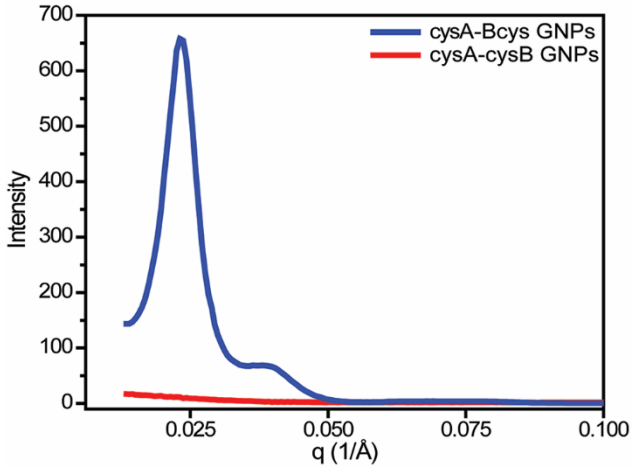

Figure 5. SAXS profiles for cysA-Bcys and cysA-cysB conjugated GNPs on day 10. The maximum peak in the spectrum of cysA-Bcys conjugated GNPs revealed a d-spacing (center-to-center distance) of 26.8 nm in the aggregates as calculated by $d = 2\pi/q$, where d is the d-spacing and q is the scattering vector.

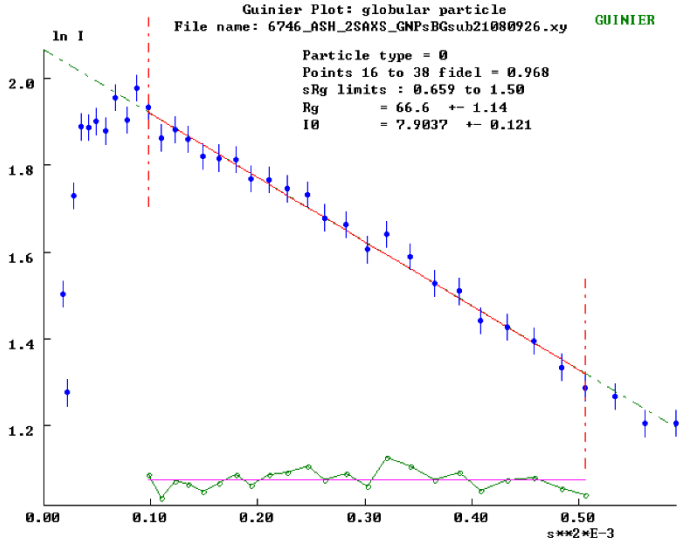

Figure 6. Guinier plot for the SAXS data collected from unmodified GNPs.

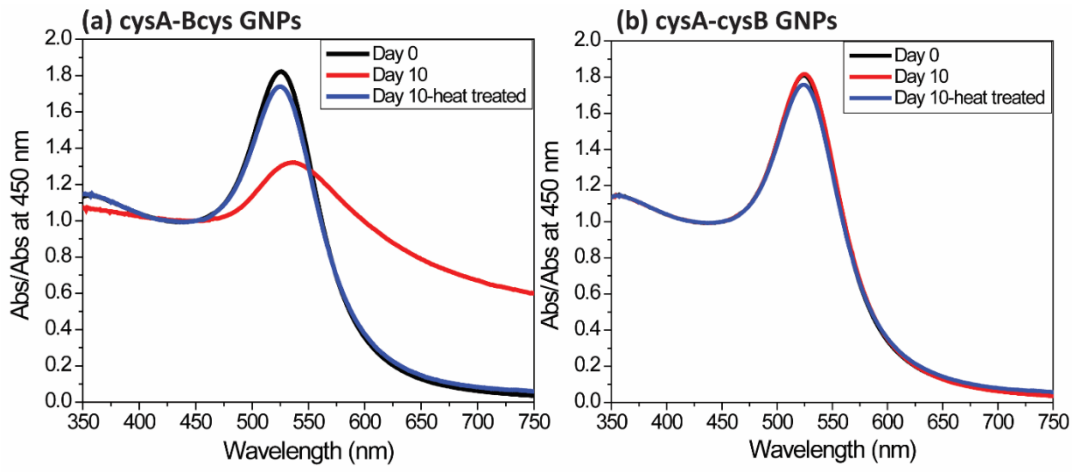

Figure 7. Disassembly of protein-conjugated GNPs. UV-Vis spectra of protein-conjugated GNPs on day 0, day 10, and day 10 followed with heat treatment at 80 °C for cysA-Bcys GNPs (a) and cysA-cysB GNPs (b). After heat treatment, broadening of the SPR peak of cysA-Bcys GNPs disappears, and the maximum SPR peak is consistent with that before assembly, suggesting that self-assembled cysA-Bcys GNPs can disassemble upon protein denaturation.

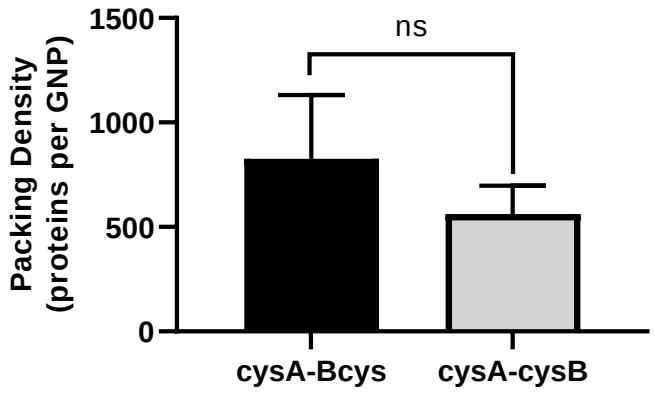

Figure 8. Packing density of protein-modified GNPs. The packing density, or number of proteins per GNP, for cysA-Bcys GNPs and cysA-cysB GNPs as determined by ICP-OES and TOC analyses. Students t-test, p-value<0.1, n=5.

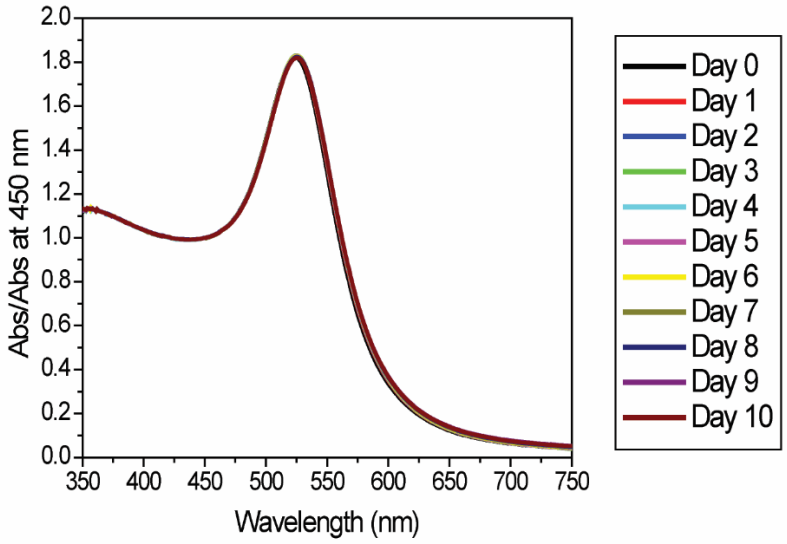

Figure 9. Behavior of GNPs with high packing density. UV-Vis spectra of cysA-Bcys conjugated GNPs prepared without non-cysteinated proteins examined over 10 days. The UV-Vis spectrum does not show broadening or a shift of the maximum SPR peak for both types of GNPs.

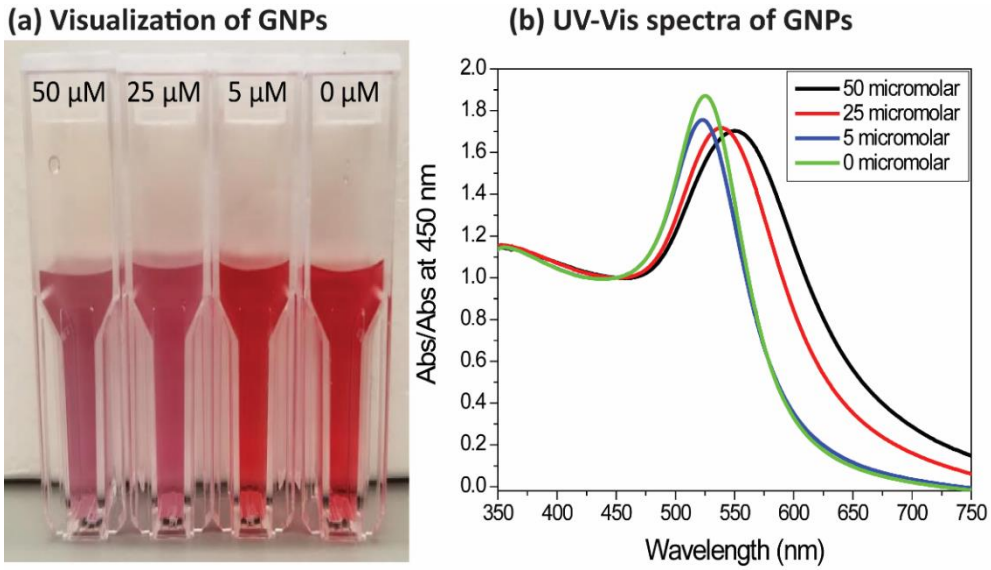

Figure 10. Behavior of GNPs with low packing density. The particle behavior of cysA-cysB GNPs prepared with varying concentrations of β-mercaptoethanol (βME) on day 0. The samples prepared with high concentrations of βME showed instability quickly, as revealed from the color of the particle suspensions (a) and the broadening and shift of the SPR peak (b).

Chapter 3: Development of self-assembling, multivalent viral entry inhibitors to block HIV-1 infection

Synopsis

This work aims to develop a new approach to HIV-1 viral entry inhibition by efficiently blocking the virus from entering host cells. HIV-1 enters host cells via interactions between its glycoprotein gp120 and the host cell receptor CD4 and co-receptors CXCR4 or CCR5. As a novel antiviral, we developed a nanoparticle-based system that displays many copies of a targeting ligand for gp120. After binding, the antiviral nanoparticles will "link up" on the virus surface, forming a cage around the virus, ultimately attenuating infection. To do this, we designed gold nanoparticles (GNPs) decorated with proteins that exhibit two unique features: (1) an antiviral targeting sequence and (2) complementary crosslinks known as coiled-coils that drive GNP self-assembly (described in Chapter 2). First, this chapter provides a brief review of viral entry inhibitors. Next, the design and structure of protein-conjugated GNPS for HIV-1 entry inhibition are described. Lastly, the ability of protein-conjugated GNPs to inhibit HIV-1 infection is reported.

3.1 Introduction

3.1.1 Viral Entry Inhibitors

Viruses establish infection in hosts through a multi-step process, starting with initial attachment and entry into host cells, followed by genome release and replication, viral protein synthesis, and the release of new viral particles.[94] Viral entry, the first step in infection, involves multiple interactions between proteins on the virus and host cell,

resulting in attachment and fusion of the virus with the host cell membrane.[94,95] Preventing viral entry into host cells serves as a target for antiviral therapies.

Entry inhibitors are a class of antiviral therapies that prevent viruses from entering cells. One mechanism entry inhibitors employ is competitive inhibition, where an antiviral blocks the interactions between viral proteins and target cell receptors preventing viral attachment to host cells. These entry inhibitors can target either viral proteins or host cell receptors.[95,96]

3.1.2 Multivalent Viral Entry Inhibitors

Multivalency results when multiple weak interactions with low binding affinity occur simultaneously, resulting in a high avidity interaction.[97] Multivalent viral entry inhibitors are more effective than their monovalent counterparts. This was first demonstrated with a multivalent display of sialic acid, an influenza entry inhibitor, in which polymers displaying sialic acid in a multivalent fashion were better inhibitors of influenza than monovalent sialic acid.[98] These multivalent competitive inhibitors increased the avidity of binding, minimized exposed surface area of viruses, and reduced the number of potential binding regions due to steric hindrance.[97,98] Since this finding, numerous platforms have been used for multivalent display of entry inhibitors, including polymers, polyglycerols, cyclodextrins, dendrimers, fullerenes, and nanoparticles to inhibit many different viruses, such as influenza, vesicular stomatitis virus, human immunodeficiency virus, and Ebola.[99–103]

Examples of polymers that have been developed as multivalent viral entry inhibitors include linear, dendritic, comb-branched, and dendrigraft polymers.[104–106] Spaltenstein and Whitesides, the first to develop multivalent entry inhibitors, used a linear

copolymer consisting of sialic acid-modified acrylamide and acrylamide derivatives to form influenza entry inhibitors.[104] Sialic acid is a cellular receptor for influenza virus, and monovalent sialic acid acts as a competitive inhibitor for hemagglutinin proteins on influenza. Whitesides et al. reported that displaying multiple sialic acid residues on a linear polymer chain mimics the polyvalency of natural host cell receptors and improves inhibition.[104] Also, Whitesides et al. proposed two different mechanisms through which viral inhibition occurs: 1) cooperative interactions, which occur when many sialic acid moieties are presented on the same polymer chain, and 2) steric stabilization, which makes the viral surface physically inaccessible to host cell receptors due to the bulky polymer.[104] Whitesides et al. then introduced different side chains in the polymer to study the effects of various polymer properties on viral inhibition, including size, charge, and hydrophobicity.[105] Side chains that increased a polymer's affinity for the viral surface improved inhibition due to steric stabilization.[105] Additional properties, such as polymer molecular weight, polymer topology, sialic acid distribution, and sialic acid content have been found to be key parameters in developing effective viral entry inhibitors, as discussed by Bianculli et al.[107]

Although linear polymers are effective viral entry inhibitors, the toxicity of poly(acrylamide)-based inhibitors presents an issue. As an alternative to linear polymers, dendritic polymers have been used as multivalent viral inhibitors because they have a high degree of functionality.[106,108] Dendritic polymers encompass a wide range of structures, including spheroidal (dendrimer), linear-dendron, comb-branched, and dendrigraft polymers.[106] Reuter et al. studied the effects of various dendritic structures on influenza infection and found that comb-branched and dendrigraft polymers were the most effective

inhibitors of influenza.[106] Papp et al. synthesized multivalent inhibitors from dendritic hyperbranched polyglycerols and polyglycerol nanogels decorated with sialic acid to evaluate the effects of size and degree of functionalization on viral inhibition. Papp found that size and sialic acid functionalization were optimal when matched to the virus size and receptor multiplicity. Additionally, larger dendrimers were found to improve inhibition compared to smaller dendrimers. Furthermore, too many sialic acid moieties on the same polymer size decreased viral inhibition, demonstrating the importance of optimizing ligand density.[108]

Host cell receptors also serve as targets for multivalent inhibitors. DC-SIGN, a host cell receptor, contributes to the transmission of Ebola, HIV, and Dengue virus. Dendrimeric scaffolds presenting *bis*-benzylamide were shown to bind DC-SIGN with high affinity and inhibit HIV and Dengue virus in infection models.[109] Overall, many different polymeric-based systems have been well characterized as viral entry inhibitors for targeting both viral and host cell receptors.

Gold nanoparticles (GNPs) have also been explored for viral entry inhibition due to their ease of characterization and functionalization.[110–113] Using GNPs as a core, peptide triazoles, a class of entry inhibitors that target HIV-1 by binding the viral glycoprotein gp120, have been presented in a multivalent fashion. The multivalent presentation of the peptide triazole, KR13, on GNPs was found to inhibit HIV-1 infection *in vitro*. KR13 peptides conjugated on GNPs were better inhibitors than KR13 alone due to their ability to bridge multiple viral proteins, highlighting one of the benefits of multivalent display.[114]

GNPs of various sizes have been functionalized with sialic acid-terminated glycerol dendrons for targeting influenza virus. Papp et al. demonstrated that larger GNPs (14 nm

in diameter) were more effective inhibitors of influenza than 2 nm GNPs. Smaller GNPs have less surface area for interactions with the viral surface, resulting in fewer multivalent interactions.[110]

GNPs can be well controlled for size and degree of functionalization, and therefore have been used to systematically explore viral entry inhibitor properties. Using GNPs decorated with polysulfates to target vesicular stomatitis virus (VSV), Vonnemann et al. demonstrated that nanoparticles larger than the virus formed virus-inhibitor aggregates and were effective inhibitors. In contrast, nanoparticles smaller than the virus diameter were found to decorate individual viruses, did not form aggregates, and were ineffective inhibitors.[115] Many GNP-based systems have been used to elucidate the mechanisms of multivalent viral entry inhibition.

3.1.3 Novel self-assembling viral entry inhibitor design

Although many multivalent viral entry inhibitors have been designed, *in situ* self-assembly has not been used for viral inhibition. Here, we describe novel GNP-based viral entry inhibitors that exhibit two key features: (1) multivalent presentation of a viral targeting ligand and (2) *in situ* self-assembly. After binding the virus, inhibitors are expected to "link up" and form a stable "cage" around the virus. This self-assembly is expected to enhance cooperativity and binding affinity of the entry inhibitors, requiring a lower concentration to cover the viral surface and attenuate viral infection.[116]

To test our hypothesis that self-assembly improves viral entry inhibition, we used human immunodeficiency virus type-1 (HIV-1) as a model virus. HIV-1 displays multiple copies of the viral glycoprotein envelope on its surface. The external subunit of envelope, gp120, interacts with the host cell receptor, CD4, and co-receptor, CXCR4 or CCR5.[117]

Here, GNPs are conjugated with two coiled-coil proteins “A” and “B”, which have been previously shown to heterodimerize and drive nanoparticle self-assembly in Chapter 2.[78,118,119] A targeting ligand for gp120, anti-gp120, is fused to coiled-coil “A” and displayed on the exterior of modified GNPs. Our viral entry inhibitors are expected to bind HIV-1 with anti-gp120 and link up on the virus in a multivalent and cooperative manner to attenuate viral infection.

3.2 Experimental Section

3.2.1 Recombinant protein expression

Recombinant protein expression was completed using the pqE-9 expression vector and was previously reported for cysA, Bcys, cysB, nA, and nB (see section 2.2.1).[78,118,119] The cysAlgp120 vector was transformed into *E.coli* strain SG13009 for expression induced by isopropyl β-D-1-thiogalactopyranoside (IPTG). After the expression of recombinant proteins, histidine-tagged recombinant proteins were purified using a Ni-NTA affinity column. The proteins were then characterized using SDS-PAGE and MALDI mass spectrometry on a 5800 MALDI/TOF Mass Spectrometer (AB-SCIEx). Circular dichroism (CD) spectroscopy (Jasco J-815 Spectropolarimeter) was completed to verify the secondary structure of the proteins. The sequence for cysA fused with anti-gp120, or cysAlgp120, is shown in Figure 12a, and sequences for all other proteins were previously reported (see Table 1).[119] Protein structures of cysA and cysAlgp120 were predicted using the Phyre2 server.[120]

3.2.2 Synthesis and characterization of GNPs

The Frens-Turkevich method[79] was used to synthesize GNPs as previously described[119] (see section 2.2.2). GNPs with a diameter of 100 nm were kindly provided by

Dr. Li Zhan from Dr. John Bischof's laboratory (University of Minnesota). The GNPs were characterized using dynamic light scattering (DLS) and UV-Vis spectrophotometry.

3.2.3 Surface modification of GNPs with proteins

The surface of GNPs was modified with either cysA and cysB (cysA-cysB GNPs); cysA and Bcys (cysA-Bcys GNPs); cysAlgp120 and cysB (cysAlgp120-cysB); or cysAlgp120 and Bcys (cysAlgp120-Bcys) through gold-thiol reaction. The surface modification of cysA-cysB and cysA-Bcys GNPS is described previously[119] (see section 2.2.3). The cysAlgp120-cysB GNPs and cysAlgp120-Bcys GNPs were prepared similarly. Briefly, the solution of each cysteinated protein (50 μM) was prepared in the presence of its non-cysteinated heterodimerizing partner (75 μM) to form heterodimers (cysAlgp120/nB, cysB/nA, Bcys/nA). Each solution was prepared in 40 mM HEPES buffer with 5 mM TCEP (pH 7.8) and incubated for 12 hours at 4 °C. To modify GNPs, the solutions of cysB/nA and cysAlgp120/nB or the solutions of Bcys/nA and cysAlgp120/nB were mixed at a 1:1 ratio and then added dropwise to the GNP suspension at a 1:3 ratio while stirring, followed by stirring overnight. The protein-conjugated GNPs were stored at 4ºC until further use and were characterized using dynamic light scattering (DLS) and UV-Vis spectrophotometry.

3.2.4 Characterization methods for protein-modified GNPs

GNPs were analyzed using DLS and UV-Vis spectrophotometry. Samples were filtered through a 0.2-micron filter, and particle size was measured using a 90Plus Particle Size Analyzer (Brookhaven) at the 90° scattering angle. The average hydrodynamic diameter was determined using the method of cumulants, and polydispersity values lower than 0.08 were considered to be monodisperse. UV-Vis spectra were collected from 350 to

750 nm on a Cary Win 300 UV-Vis spectrophotometer (Agilent Technologies) at a scanning rate of 600 nm min^{-1} and a 1 nm resolution.

3.2.5 Determining GNP concentration after protein modification

The unmodified GNP concentration was determined using UV-Vis spectrophotometry as previously reported by Haiss et al. (refer to section 2.2.7).[121] During protein conjugation, the GNPs were diluted at a ratio of 2:3, and this dilution factor was used to determine the concentration of GNPs after protein conjugation.

3.2.6 Live/dead assay

U373-MAGI-CXCR4 cells (obtained from Michael Emerman through the NIH AIDS Reagent Program, Division of AIDS, NIAID, NIH) were cultured in Dulbecco's modified Eagle's medium (DMEM; Cellgro) plus 10% FetalClone III (FC3; Hyclone) and 1% penicillin/streptomycin (Invitrogen). 1 mL of MAGI cells at a density of 35,000 cells mL^{-1} were added to a well of a 24-well plate. 24 hours after seeding, 2 mL of protein-conjugated GNPs were sterile filtered through a 0.2 μm filter into protein low-binding microcentrifuge tubes (Eppendorf). The GNPs were then centrifuged at 5.6krcf for 1 hour, followed by removing 1.7 mL of the supernatant and adding 500 or 800 μL of MAGI cell medium. The GNPs were then added to MAGI cells at final concentrations of 7.35×10^{10} and 6.30×10^{10} particles mL^{-1}, respectively, followed by culturing cells for 5 days. After 5 days, cells were stained with ethidium homodimer and calcein AM (0.1% v/v) for 30 min, washed once with PBS, and imaged in PBS using a 2.5× objective on a Zeiss Axio Observer inverted fluorescence microscope equipped with 470/525 and 550/650 excitation/emission filters.

3.2.7 Production of HIV-1 pseudotyped particles

Vector viruses were produced via transient transfection of HEK-293T17 cells as previously described.[122,123] Briefly, 10 mL 293T17 cells were seeded at a density of 4 x 10^5 cells mL^{-1} in a 10-cm dish. The polyethyleneimine (PEI) method was used to transfect DNA: 10 μg pNL43-MIG plasmid DNA, 5 μg of HIV-1 CXCR4-envelope plasmid DNA (from Dr. Eric Freed, HIV Drug Resistance Program, Frederick National Laboratory for Cancer Research, Frederick, MD, USA), and 44 μL of 1 mg/mL PEI were diluted to a total volume of 1 mL in serum-free DMEM. 1 mL of plasmid DNA/PEI solution was added to each 10-cm dish. 24 hours post-transfection, the medium was removed and replaced with 6.5 mL fresh medium. The cell culture supernatants were collected 48 hours post-transfection, centrifuged at 1000 rpm for 5 minutes, and stored at -80 °C until further use. The collected cell culture supernatants containing the virus are referred to as the virus stock solutions.

3.2.8 ELISA assay to determine the concentration of HIV-1

The concentration of HIV-1 was determined using an ELISA assay to quantify HIV-1 p24 protein (Advanced Biosciences Laboratory, Inc). The p24 concentration corresponds to the number of viral particles, where 1 ng of p24 is equivalent to 1 x 10^7 viral particles.[124] It is important to note that the concentration determined through this method is the total concentration of virions, including both infectious and non-infectious virions.

3.2.9 In vitro infectivity assays

U373-MAGI-CXCR4 cells were used for HIV-1 infectivity assays, following previously reported methods.[122] One day before infection, 1 mL of MAGI cells were plated

at a density of 35,000 cells per mL in a 24 well plate. The cell medium was removed immediately before infection, and virus stock (100 µL to 500 µL) was diluted to a total volume of 1 mL with fresh medium and added to each of the wells. The medium was replaced at 24 hours post-infection, and cells were collected at 72 hours post-infection for flow cytometry.

3.2.10 Preparation of GNPs for infectivity assays

2 mL of protein-conjugated GNPs were sterile filtered through a 0.2 µm filter into protein low-binding microcentrifuge tubes (Eppendorf). The GNPs were then centrifuged at 5.6krcf for 1 hour, and 1.7 mL of supernatant was removed. The concentrated GNPs were then mixed with virus stock at the desired concentrations, incubated for 30 minutes, and diluted to a total volume of 1 mL. This solution was then added to MAGI cells, and viral infection was evaluated using the previously described assay. A control experiment was conducted without adding GNPs (i.e., only HIV-1 was added to MAGI cells).

3.2.11 Flow cytometry

After viral infection, cells were washed in phosphate-buffered saline (PBS) and resuspended in 200 µL of 2% FC3-PBS. Expression of mCherry and eGFP was analyzed using a BD LSR-II flow cytometer (BD Biosciences). Gates were selected based on a forward scatter channel and a side scatter channel with a minimum of 10,000 gated cells per sample. mCherry and eGFP were excited with a 488-nm laser and a 561-nm laser, respectively. The percent infection was determined by dividing cells positive for both mCherry and eGFP by the total number of cells determined by flow cytometry. The relative infection (%) was determined by dividing the percent of infected cells in the presence of inhibitors by the percent of HIV-1 infected cells (without inhibitors).

3.3 Results and Discussion

3.3.1 Design of protein-modified GNPs

The design of the nanoparticles is illustrated in Figure 11. A and B proteins were previously shown to heterodimerize in the parallel direction through hydrophobic and electrostatic interactions.[77] Fusion of the anti-gp120 protein to the A protein allows for interactions between the GNPs and viral surface through the viral glycoprotein, gp120. We previously demonstrated that immobilizing A and B in anti-parallel orientation on the same nanoparticle promotes nanoparticle self-assembly, and immobilizing A and B in parallel orientation on the same nanoparticle promotes colloidal stability.[119] To investigate the effects of nanoparticles that target the virus and self-assemble along the viral surface, the A protein with anti-gp120 ligand and the B protein were immobilized in the anti-parallel orientation to make self-assembling nanoparticles (denoted as cysAlgp120-Bcys). The colloidally stable nanoparticles (denoted as cysAlgp120-cysB), with A and B protein in the parallel direction, were evaluated as a control.

3.3.2 Design and synthesis of cysAlgp120 protein

To introduce a viral targeting ligand, the anti-gp120 peptide ligand, referred to as lgp120, was fused to the cysA protein. Lgp120 has previously been reported to bind HIV-1 and competitively inhibit binding of HIV-1 gp120 to CD4.[125] The sequence of the cysA protein fused with lgp120 (denoted as cysAlgp120) is shown in Figure 12a, in which the cysteine residue (used for conjugation) is shown in red, the coiled-coil sequence is shown in blue, and the lgp120 sequence is shown in green. Lgp120 is located on the C-terminus, opposite the cysteine residue, and should appear on the exterior of GNPs after conjugation. After protein synthesis and purification, MALDI-MS and SDS-PAGE were used to

confirm the molecular weight, which was expected to be 10994 Da (Figure 12b). Additionally, the predicted theoretical protein structures for cysA and cysAlgp120 are shown in Figure 12c.[120] The addition of a short linker chain and the lgp120 peptide sequence was not expected to disrupt the coiled-coil structure required for nanoparticle self-assembly. CD spectroscopy was used to evaluate the secondary structure of cysAlgp120. The CD spectrum (Figure 12d) indicates a coiled-coil structure, as evidenced by two minima at 208 nm and 222 nm.[126] All other proteins used in this work were previously described.[77,78]

3.3.3 Conjugation of cysAlgp120 to GNPs with diameters of 20 and 100 nm

The conjugation of proteins was completed as previously described for cysA-Bcys GNPs and cysB-cysA GNPs (see section 2.3.3).[119] Three cysteinated coiled-coil proteins, cysAlpg120, Bcys, and cysB, and two non-cysteinated coiled-coil proteins, nA and nB, were synthesized (see Table 1 and Figure 12a for sequences). Protein solutions were prepared with both a cysteinated and non-cysteinated protein partner as previously described,[119] including cysAlgp120 and nB (cysAlgp120/nB), nA and cysB (nA/cysB), and nA and Bcys (nA/Bcys). These heterodimers were then conjugated to GNPs of either 20 or ~100 nm through a gold-thiol reaction. The solutions of nA/Bcys and cysAlgp120/nB or nA/cysB and cysAlgp120/nB were mixed at a 1:1 ratio and added to a GNP suspension at a 1:3 ratio while stirring. Like our previous nanoparticle design, GNPs modified with cysAlgp120 and Bcys (denoted as cysAlgp120-Bcys GNPs) had the two coiled-coils conjugated on the surface in anti-parallel orientation (and thus would self-assemble). In comparison, GNPs modified with cysAlgp120 and cysB (denoted as cysAlgp120-cysB

GNPs) had the two coiled-coils on the surface in parallel orientation (and thus would be colloidally stable).

Immediately following protein conjugation, DLS was used to evaluate the change in nanoparticle size. The hydrodynamic diameters of 20 nm GNPs after protein conjugation were approximately 36-37 nm for cysAlgp120-Bcys and cysAlgp120-cysB GNPs (Table 3). The change in hydrodynamic diameter from 20 nm for unmodified GNPs to 36-37 nm for protein-conjugated GNPs suggests an approximately 8-8.5 nm thick corona, consistent with our previous finding of approximately 7.9 nm[119] and the additional anti-gp120 peptide sequence. The polydispersity of the protein-conjugated GNPs was the same as that of unmodified GNPs, demonstrating that aggregation did not occur during or after the conjugation procedure. The protein-conjugated GNPs were also characterized using UV-Vis spectrophotometry. The maximum SPR peak of the UV-Vis spectra shifted from 518 nm for unmodified GNPs to 524 nm for both cysAlgp120-Bcys and cysAlgp120-cysB conjugated GNPs (Figure 13). The red-shift in the SPR peak suggested that proteins were bound to the GNP surface.[127]

For larger GNPs, the average size after protein modification was ~97 nm (Table 3), with a starting size of ~88 nm. These GNPs were more disperse than the 20 nm GNPs for both unmodified and modified GNPs.

3.3.4 Protein-modified GNPs are non-toxic to MAGI cells

The cytotoxicity of protein-conjugated GNPs was evaluated before completing *in vitro* infectivity assays. cysAlgp120-Bcys (self-assembling) and cysAlgp120-cysB (stable) GNPs were added 24 hours after seeding MAGI cells, a cell line designed for *in vitro* studies of HIV-1 infection.[128] After 5 days, the cells were stained with live/dead staining

and imaged (Figure 14). Few dead cells were observed for both cysAlgp120-Bcys and cysAlgp120-cysB. Additionally, the cell morphology was similar between untreated and nanoparticle-treated cells. These results suggest that protein-modified GNPs are not cytotoxic to MAGI cells after 5 days of exposure, consistent with other reports that indicate GNPs are biocompatible and non-cytotoxic.[129–131]

3.3.5 HIV-1 is not inhibited by 20 nm cysAlg120 modified GNPs

Next, HIV-1 viral particles were produced containing HIV-1 NL4-3 MIG vector (which results in a single cycle of infection and expression of mCherry and eGFP in infected cells) and pseudotyped with HIV-1 envelope protein (which contains gp120) for viral infectivity assays.[122,123] An enzyme linked immunosorbent assay, or ELISA, was used to determine the total number of viral particles by quantifying the amount of p24 protein, an HIV-1 structural protein.[124] It is interesting to note that not all viral particles produced are infectious. The ELISA assay determines the total number of viral particles but does not distinguish infectious virions from non-infectious virions. Therefore, infection was assessed before completing nanoparticle dose-response curves to determine an optimal virus concentration (>15% infected cells determined by flow cytometry).

To evaluate the inhibitory effects of cysAlgp120-Bcys GNPs (self-assembling) and cysAlg120-cysB GNPs (stable) (20 nm GNPs), nanoparticles were incubated with HIV-1 for 30 minutes and added to MAGI cells (Figure 15a). After 72 hours post-infection, the percent of infected cells was determined using flow cytometry. The percent of infected cells was normalized to infected cells not treated with GNPs. Additionally, the inhibitory effects of cysAlgp120-Bcys and cysAlgp120-cysB GNPs were compared to GNPs without

lgp120 (i.e., cysA-Bcys and cysA-cysB GNPs) to ensure inhibitory effects were due to the anti-gp120 ligand.

First, the maximum possible concentration of protein-conjugated GNPs for *in vitro* infectivity assays was determined. A concentration of 7.70 x 10^{11} GNPs mL^{-1} cysA-cysB GNPs (without anti-gp120 ligand) inhibited HIV-1 infection by ~37%, while a concentration of 3.85 x 10^{11} GNPs mL^{-1} had almost no effect (0.5 mL of the virus was added for a concentration of 2.56 x 10^{8} virions mL^{-1}). This suggested that high concentrations of protein-modified GNPs inhibit viral infection non-specifically, and thus a maximum concentration of 3.85x 10^{11} GNPs mL^{-1} was used for all future studies.

The inhibitory effects of cysAlgp120-Bcys, cysAlgp120-cysB, cysA-Bcys, and cysA-cysB were then evaluated (Figure 15b). A virus concentration of 2.56 x 10^{8} virions mL^{-1} and GNP concentrations of 3.85 x 10^{11}, 1.92 x 10^{11}, and 7.70 x 10^{10} GNPs mL^{-1} were used. Protein-modified GNPs with the anti-gp120 ligand increased viral infection instead of inhibiting infection. The percent of infected cells increased ~2.1 times and ~2.4 times for cysAlgp120-Bcys GNPs and cysAlgp120-cysB GNPs (3.85 x 10^{11} GNPs mL^{-1}), respectively, as compared to virus infected cells. CysA-Bcys and cysA-cysB GNPs showed little to no effect on infection.

3.3.6 HIV-1 is not inhibited by 100 nm cysAlg120 modified GNPs

Previous reports have shown that larger nanoparticles used for viral inhibition are more effective inhibitors than smaller nanoparticles. Vonneman et al. demonstrated that smaller nanoparticles were weak viral inhibitors, while larger nanoparticles resulted in virus-nanoparticle clusters and were stronger viral infection inhibitors.[115] Therefore, protein-modified GNPs with a diameter of ~100 nm were examined for their inhibitory

effects (Figure 15c). For this assay, nanoparticle concentrations of 8.25 x 10^8, 4.30 x 10^8, and 1.65 x 10^8 particles mL^{-1} were evaluated (with a virus concentration of 2.17 x 10^9 virions mL^{-1}). It was observed that cysAlg120-Bcys and cysAlgp120-cysB GNPs did not inhibit viral infection and had similar infectivity levels to the control GNPs without lgp120 (cysA-Bcys and cysA-cysB). Overall, these results showed that 100 nm GNPs with the anti-gp120 peptide were not effective inhibitors of HIV-1 infection. Additionally, an increase in infection was not observed for 100 nm cysAlg120-cysB or cysAlgp120-Bcys GNPs, as was observed for 20 nm GNPs.

3.3.7 Cellular internalization is not responsible for the increase in HIV-1 infection

20 nm GNPS are known to be readily internalized by cells.[132] To evaluate if the increase in infection observed in Figure 15b was due to internalization or specific interactions between HIV-1 gp120 and CD4 cell receptors, the viral infectivity assay was completed with cells lacking the HIV-1 receptor CD4. The fibroblast cell line, 3T3, and human embryonic kidney cell line, HEK-293T17, which both lack the CD4 receptor, were used. In this assay, 2.17 x 10^9 viral particles mL^{-1} (0.5 mL of virus stock) was used, and cysAlgp120-cysB and cysA-cysB GNPs at a concentration of 3.85 x 10^{11} GNPs mL^{-1} were evaluated (cysAlgp120-cysB GNPs showed the greatest increase in infectivity in Figure 15b). Neither 3T3 nor HEK-293T17 cells were infected with virions as determined by flow cytometry (Table 4). These results suggest that the increase in viral infection observed with MAGI cells is cell type-specific and does not occur from non-specific cellular uptake of nanoparticles bound to virions.

Additionally, an increase in viral infection for MAGI cells was not observed in this experiment, as previously observed (section 3.3.5 and Figure 15b). Instead, a slight

decrease in infection was observed for cysA-cysB GNPs and cysAlgp120-cysB GNPs. In these two studies, the volume of virus stock solution and the concentration of GNPs were controlled. However, the concentrations of virus stocks were different: this virus stock had a much higher concentration of virions than the previous study. However, the percent infection was similar between cells infected with only the virus in both studies (i.e., without GNPs), indicating differences in the percent of infectious virions. This resulted in differences between the ratio of GNPs to HIV-1 in each study (Table 5), suggesting that the ratio of GNPs to viral particles needs to be optimized and could be a key parameter in assessing inhibition of viral infection.

3.3.8 CysAlgp120 peptide inhibits viral infection

The viral infectivity assays with protein-conjugated GNPs showed little to no viral inhibition. Therefore, the cysAlgp120 peptide (not conjugated to GNPs) was evaluated for viral inhibition using the *in vitro* viral infectivity assay. Either cysAlgp120 or cysA was incubated with HIV-1 for 30 minutes and added to MAGI cells. After 72 hours post-infection, the cells were analyzed using flow cytometry. The inhibitory effects of cysAlgp120 and cysA peptides are presented in Figure 16. 100 μM of the cysAlgp120 peptide inhibited viral infection to ~70%, while 100 μM of cysA peptide promoted viral infection (~126%). These results suggest that the anti-gp120 ligand can inhibit viral infection. However, high concentrations of this peptide are required, which may present challenges in using this peptide to design viral entry inhibitors.

3.4 Discussion

This work aimed to develop a new approach to HIV-1 viral inhibition. The molecular design of the GNPs proposed here utilized a GNP-based platform to display an

antiviral ligand for HIV-1 multivalently**.** After binding the virus, the inhibitors were expected to link up and form a stable cage around the virus due to the heterodimerizing coiled-coils conjugated to the GNPs. The modified GNPs were expected to exhibit high affinity binding to gp120 further stabilized by the *in situ* self-assembly, blocking the virus from entering the cell. However, we observed that protein-conjugated GNPs with the anti-gp120 ligand did not inhibit viral infection.

One possible reason for this is that HIV-1 virions have very few envelope glycoproteins (or gp120 protein) expressed on the surface (in the range of 7 to 14 envelope protein per virus).[133,134] Therefore, there are very few sites in which the anti-gp120 conjugated GNPs could bind. Other viruses, such as influenza virus, have a much larger number of proteins on their exterior (influenza has ~400 hemagglutinin proteins).[134,135] These viruses may present an easier target to evaluate the self-assembling viral entry inhibitors. To test this, ADA-CM-V4 cells, designed to produce HIV-1 virus-like particles with varying amounts of gp120 protein, could be used.[136] Infectious viral particles may be produced using the ADA-CM-V4 cells with higher levels of gp120, and the inhibitory effects of the self-assembling entry inhibitors could be evaluated.

Another possible reason that the viral entry inhibitors designed here are ineffective is the protein-ligand used in these studies. Viral inhibition of cysAlgp120 protein was evaluated, and this protein was found to have a concentration at 50% inhibition (or IC_{50}) greater than 100 μM. Different peptide ligands can first be screened for their inhibitory effects for future studies, followed by fusion to the "A" protein and conjugation to GNPs. The following peptide inhibitors have previously been explored for inhibition of HIV-1 and could be alternative peptides for conjugation to GNPs:

1. WMEWDREINNYTSLIHSLIEESQNQQEKNEQELL[137]
2. LLQLTVWGIKQLQARIL[138]
3. NNLLRAIEAQQHLLQLTVWGIKQLQARILAVERYLKDQ[138]
4. AAAAKILGNQGSFLTKGPSKLAAAA[139]
5. SHTTWMEWDREINNYTSLIHSLIEESQNQQEKNEQELL[140]
6. HKQPWYDYWLLR[141]

These peptide inhibitors could replace the anti-gp120 ligand and be screened for their inhibitory effects, as they may be more effective inhibitors of HIV-1 than the anti-gp120 reported in this work.

3.5 Conclusions

In summary, protein-conjugated GNPs were designed to exhibit self-assembly and viral targeting with an anti-gp120 ligand. Towards this, a coiled-coil "A" protein was fused to an anti-gp120 ligand (cysAlgp120). Both 20 nm and 100 nm GNPs were conjugated with the heterodimerizing coiled-coil proteins, cysAlgp120 and Bcys or cysB, which were previously shown to exhibit either self-assembly or stability, respectively. Additionally, the protein-conjugated GNPs were used to inhibit HIV-1 infection; however, the GNPs showed negligible inhibition. After observing this, the inhibitory effects of cysAlgp120 protein were assessed and shown to require high concentrations to inhibit viral infection. Overall, using a different virus to evaluate the viral entry inhibitors or incorporating other targeting peptide ligands in the viral entry inhibitors may be possible approaches to overcome the minimal inhibitory effects observed here.

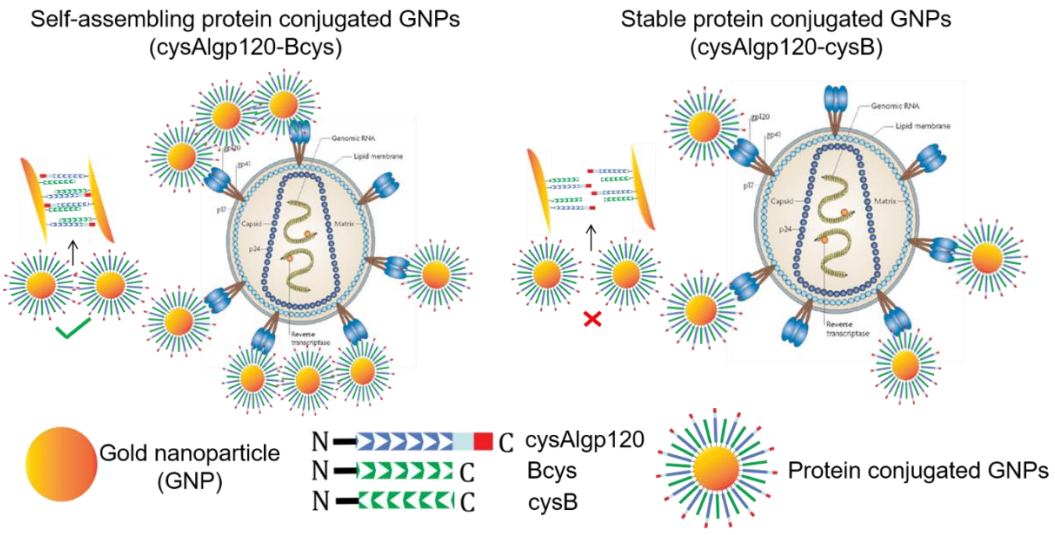

Figure 11. Design of viral entry inhibitors. The self-assembling cysAlgp120-Bcys GNPs are shown on the left, and the colloidally stable cysAlg120-cysB GNPs are shown on the right. The anti-gp120 ligand is shown in red, the cysA protein is shown in blue, and the B-related proteins are shown in green. HIV-1 image modified from Hedestam et al.[142]

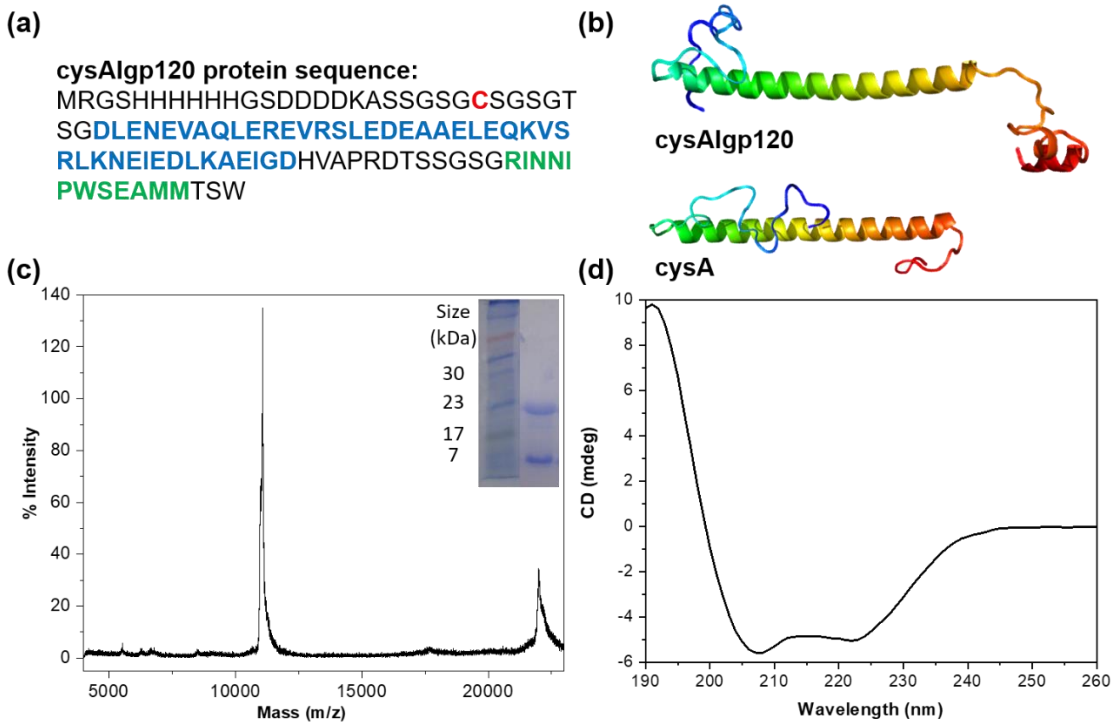

Figure 12. Structure and characterization of cysAlgp120. (a) The sequence of cysAlgp120 protein. (b) The predicted theoretical protein structures of cysAlgp120 and cysA.[120] The coiled-coil is shown as a helix in these structures. (c) MALDI-MS data for cysAlgp120 to confirm the molecular weight. The inset is SDS-PAGE results confirming the molecular weight. (d) CD spectroscopy of cysAlgp120 protein to confirm the coiled-coil structure is not disrupted after fusion of the anti-gp120 protein.

Table 3. DLS of modified and unmodified GNPs. Dynamic light scattering results of 20 nm and 100 nm GNPs before and after modification with proteins. The size and polydispersity are reported here.

Dynamic Light Scattering				
	20 nm unmodified GNPs		**100 nm unmodified GNPs**	
	Size (nm)	**Polydispersity**	**Size (nm)**	**Polydispersity**
Unmodified GNPs	20.8	0.008	88.8	0.227
cysAlgp120-Bcys	37.2	0.070	93.6	0.215
cysA-Bcys	37.6	0.044	92.8	0.235
cysAlgp120-cysB	36.4	0.029	107.7	0.240
cysA-cysB	34.6	0.054	93.5	0.250

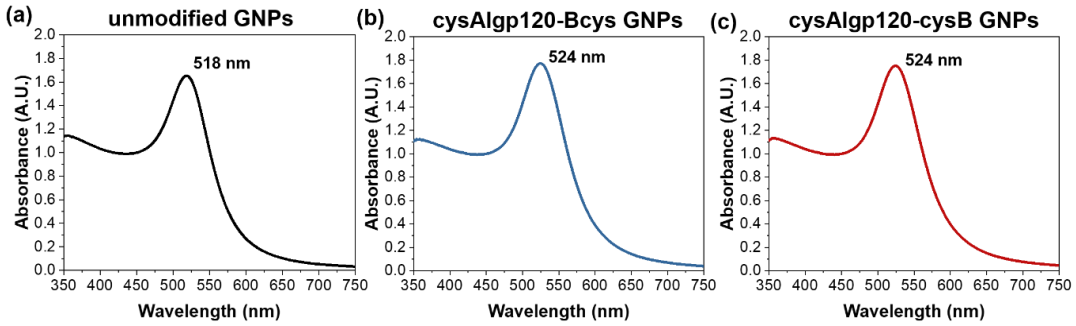

Figure 13. UV-vis spectra before and after conjugation of GNPs. The maximum surface plasmon resonance peak is labeled for each spectrum. The unmodified GNPs have an SPR peak at 518 nm while the SPR peak for cysAlgp120-Bcys and cysAlgp120-cysB GNPs are shifted to 524 nm.

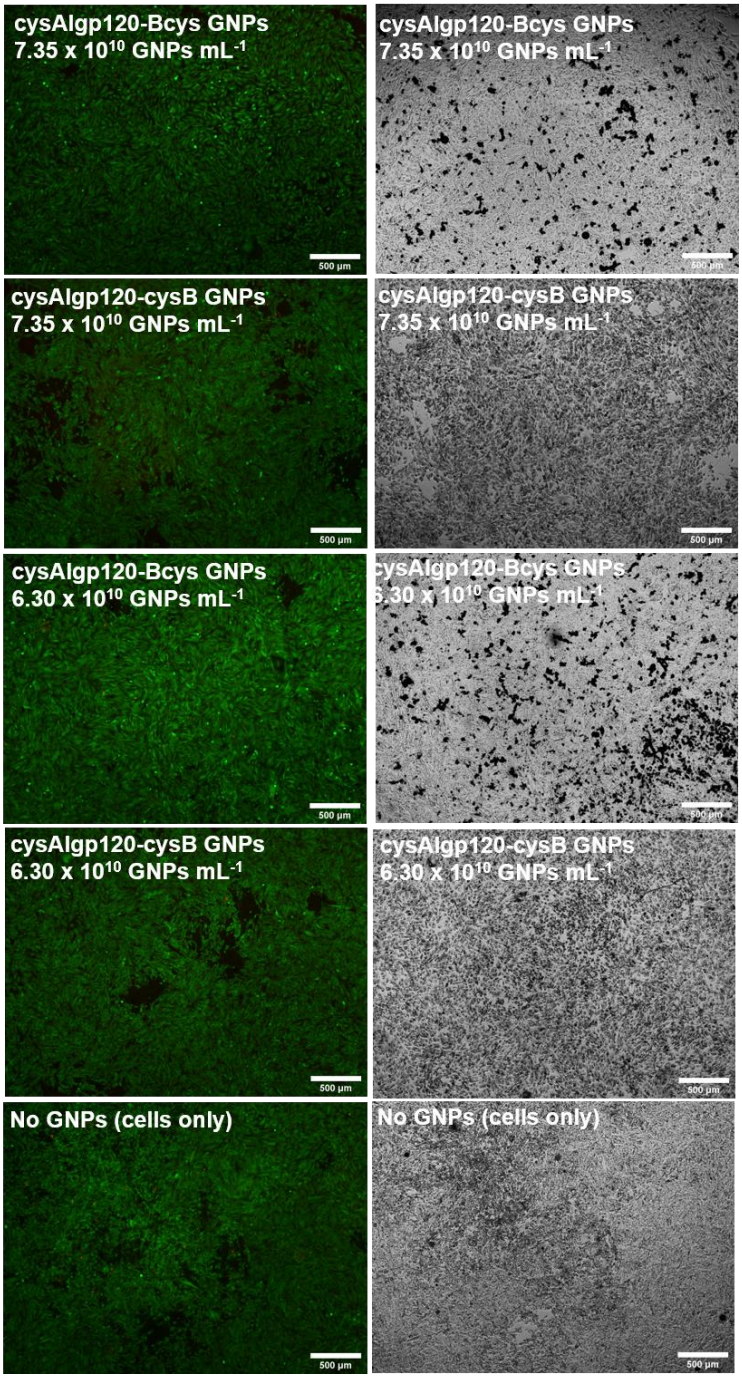

Figure 14. Cytotoxicity of protein-conjugated GNPs. Live/dead assay of protein-conjugated GNPs incubated with MAGI cells. Live cells are shown in green and dead cells are shown in red. The scale bar is 500 µm.

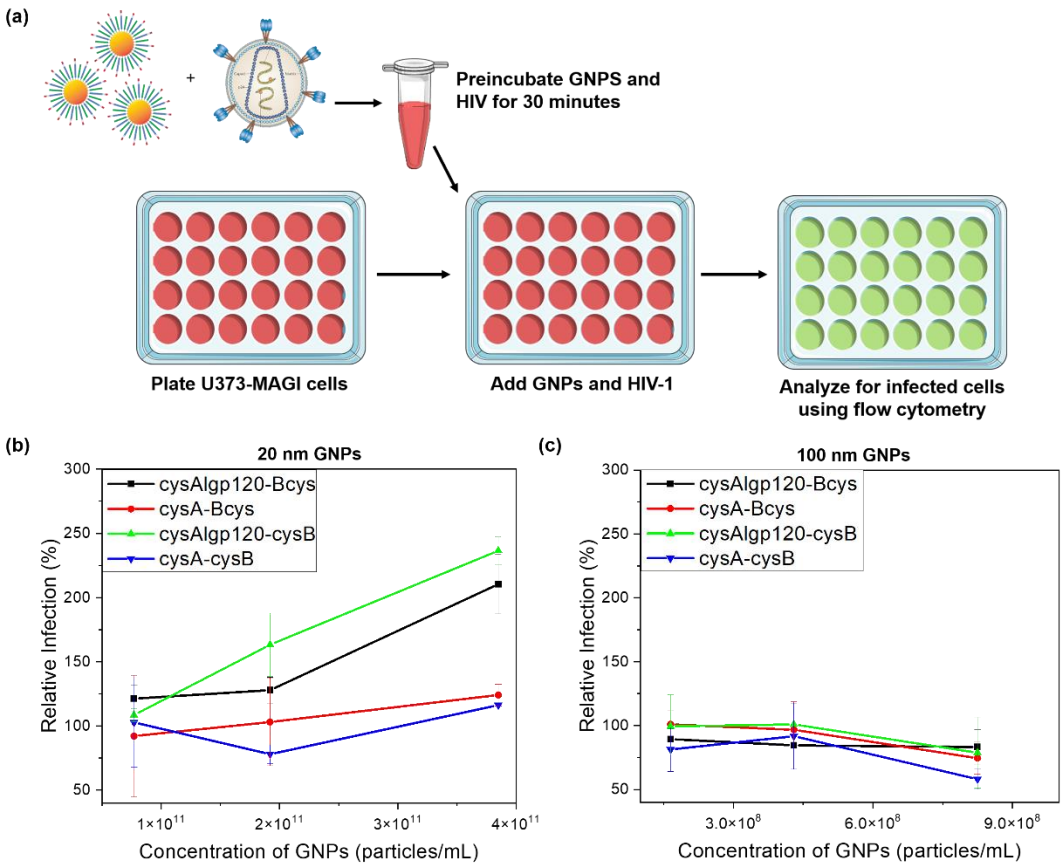

Figure 15. Inhibition of viral infection using protein-conjugated GNPs. (a) *In vitro* viral infection assay used. GNPs and HIV are preincubated for 30 minutes and added to MAGI cells. After 72 hours, flow cytometry is used to analyze the percent of infected cells. (HIV-1 image modified from Hedestam et al.[142]) (b) Inhibition of viral infection with 20 nm protein-conjugated GNPs. (c) Inhibition of viral infection with 100 nm protein-conjugated GNPs. Relative infection (%) is determined by dividing the percent of cells infected after adding GNPS and HIV-1 by the percent of cells infected after adding only HIV-1. The error bars represent standard deviation, n=3.

Table 4. Inhibition of HIV-1 infection with different cell types. Relative infection (%) is determined by dividing the percent of cells infected after adding GNPs and HIV-1 by the percent of cells infected after adding only HIV-1. Results are reported as average ± standard deviation, n=2.

RELATIVE INFECTION (%)			
	MAGI	**293T17**	**3T3**
cysAlgp120-cysB GNPs	93.0±9.4	0.0±0.0	0.0±0.0
cysA-cysB GNPs	88.9±6.4	0.0±0.0	0.1±0.1

Table 5. Variation in viral inhibition studies. The concentration of GNPs and volume of virus were controlled in these experimental replicates; however, the viral stocks in each replicate had different concentrations and amounts of infectious viral particles, resulting in differences in the ratio of GNPs to HIV-1. Results are reported as average ± standard deviation.

	Replicate 1	**Replicate 2**
Ratio of GNPs:HIV-1	1504	177
% Infection with cysAlgp120-cysB GNPs	218.1±10.0%	93.0±9.4%
% Infection with cysA-cysB GNPs	107.3±0.6%	88.9±6.4%
Virus only	100.0±4.8%	100.0±12.2%

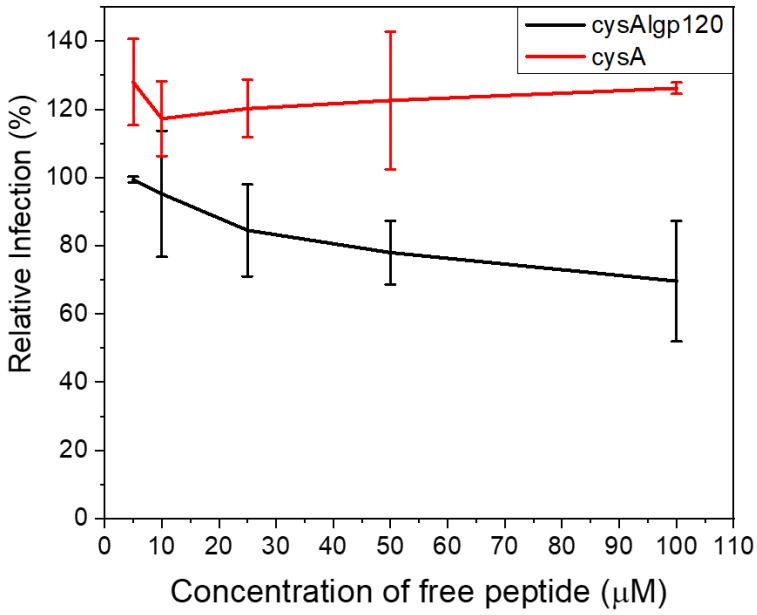

Figure 16. Inhibition of viral infection with free (unconjugated) cysAlgp120. Inhibition of viral infection with different concentrations of cysAlgp120 (black) and cysA (red) peptides. Relative infection (%) is determined by dividing the percent of cells infected after adding peptides and HIV-1 by the percent of cells infected after adding only HIV-1. The error bars represent standard deviation, n=3.

Chapter 4: Gold nanoparticle immunolabeling of HIV-1 and HTLV-1 virus-like particles

Synopsis

Envelope glycoproteins, or Env, of human immunodeficiency virus-type 1 (HIV-1) and human T-cell leukemia virus-type 1 (HTLV-1), are essential for viral entry into host cells and potential targets for both vaccine development and new antiviral therapeutics. The native distributions and stoichiometries of Env on HIV-1 and HTLV-1 virions have not been explored extensively. As an approach to characterize Env glycoproteins, a gold nanoparticle immunolabeling strategy was used, followed by imaging with electron microscopy. In this work, HIV-1 virus-like particles and HTLV-1 virus-like particles were used to optimize the nanoparticle labeling strategy. Ultimately, we aimed to elucidate the distribution and quantify Env on both HIV-1 and HTLV-1.

4.1 Introduction

According to the Joint United Nations Program for HIV/Acquired Immunodeficiency Syndrome (UNAIDS), human immunodeficiency virus (HIV) continues to be a severe public health challenge, with approximately 38 million people worldwide living with HIV and an estimated 1.7 million newly infected individuals in 2019.[143] Although great strides have been made to elucidate the physical and molecular structures of the virus and in therapy development, new infections among adults globally have not decreased significantly.[144] Vaccines are one of the most promising methods to reduce the number of new infections.[145] The HIV-1 envelope glycoprotein, or Env, serves as the primary target for vaccine development as it is the viral target for neutralizing antibody attacks.[146,147] Understanding the structure and function, as well as the distribution

and quantity of Env on the viral surface, is critical to the development of new therapeutic targets and effective vaccines.[147]

The primary function of HIV-1 Env is cell entry. HIV-1 Env is essential for the virus replication cycle as it mediates attachment to host cell receptors and co-receptors. After receptor and co-receptor binding, a conformational change occurs, resulting in fusion between the virus and host cells.[148] Env is synthesized first as a polyprotein precursor, known as gp160 in the endoplasmic reticulum. This polyprotein is cleaved by cellular proteases into a transmembrane glycoprotein, gp41, and a surface glycoprotein, gp120. Gp120 and gp41 remain associated via non-covalent interactions to form gp120/gp41 complexes, which are trafficked to the plasma membrane and either incorporated in budding virions or recycled back into the cell.[134,147] Three copies of gp120/gp41 are incorporated as a trimer into budding virions to form the protein known as Env. Env initiates the infection process in which gp120 interacts with cell receptors and gp41 mediates fusion with host cells.[149] The structures of gp120 and gp41 on HIV-1 have been well explored, and the mechanisms Env uses to traffic to the cell surface have been studied.[150–155] However, many aspects of Env are unknown, such as how HIV-1 Env is incorporated into nascent virions.[134] Additionally, the native distribution of Env on HIV-1 has not been broadly explored, and the distribution and quantification of Env on HIV-1 produced from different cell types has not been evaluated.[133] Because HIV-1 Env is critical for viral entry and is a target for vaccine development, studying the native Env distribution on HIV-1 is of interest.

Human T-cell leukemia virus type 1 (HTLV-1), which also has Env glycoproteins and is a member of the retrovirus family, is known to cause adult T-cell leukemia and

HTLV-1 associated myelopathy (or tropical spastic paraparesis).[156] Approximately 5 to 20 million people are infected with HTLV-1, and about 5% of those cases develop adult T-cell leukemia.[157] HTLV-1 enters cells through interactions between Env and host cell receptors, with CD4+ T-cells being the primary target cell *in vivo*.[156] For efficient entry of HTLV-1 into T-cells, heparan sulfate proteoglycans (HSPGs) are required.[156] Additionally, the glucose transporter type 1 (GLUT-1) and VEGF-165 receptor Neuropilin 1 (NRP-1) are necessary for viral entry. However, HTLV-1 preferentially infects new cells through direct cell-to-cell transmission, as opposed to cell-free viral infection (i.e., viruses are released from cells into the surrounding fluid and then move to infect the next cell[158]), which poses a significant challenge to HTLV-1 research.[159]

In HTLV-1 infection, Env is synthesized as a precursor protein, gp62, which is then cleaved into the gp46 and gp21 subunits. The gp21 subunit is the transmembrane unit, while gp46 is the surface subunit.[159] While a crystal structure for gp21 has been solved, the structure of gp46 is still unknown. Also, the native distribution of gp46 on the viral surface has not been explored for HTLV-1.[160] Characterizing the structure and distribution of gp46 may benefit vaccine development, as gp46 is a potential vaccine candidate for HTLV-1.[161]

This chapter presents an approach to characterize the distribution of Env glycoproteins on both HIV-1 and HTLV-1 using a gold nanoparticle (GNP)-based immunolabeling strategy. Ultimately, this work intended to develop a gold immunolabeling strategy as a robust and facile method to study Env distribution, which could further be used to understand the distribution of Env on both HIV-1 and HTLV-1. Completing these studies would broaden our understanding of the distribution, location,

and quantity of gp120 and gp46 on HIV-1 and HTLV-1, respectively, which could have implications in developing antiretroviral therapies and vaccine development.

4.2 Experimental Section

4.2.1 Materials

The anti-HIV-1 gp120 monoclonal antibody, 2G12, was obtained from the NIH AIDS reagent database (Cat# 1476). 6-nm Colloidal Gold-AffiniPure Goat Anti-Human IgG (EM grade) and 6-nm Colloidal Gold-AffiniPure Donkey Anti-Mouse IgG (EM Grade) were purchased from Jackson ImmunoResearch. Anti-HTLV-1 gp46 Antibody ((65/6C2.2.34): sc-57865) was purchased from Santa Cruz Biotechnology. All plasmids and HEK-293T17 cells were obtained from Dr. Louis Mansky's lab at the University of Minnesota.

4.2.2 Production of HIV-1 VLPs

HEK-293T17 cells were maintained in Dulbecco's modified Eagle's medium (DMEM; Cellgro) plus 10% FetalClone III (FC3; Hyclone) and 1% penicillin/streptomycin (Pen-Strep; Invitrogen). Virus-like particles (VLPs) were produced via transient transfection of HEK-293T17 cells using GenJet following the manufacturer's instructions. Briefly, 10 mL 293T17 cells were seeded at a density of 9×10^6 cells/mL in a 10-cm dish. 24 hours after cell seeding, the medium was changed and replaced with 5 mL of medium one hour before transfection. For each 10-cm dish, 15 µL of GenJet was added to 235 µL of serum-free medium, and 4 µg of HIV-1 Gag plasmid and 0.4 µg codon-optimized HIV-1 Env plasmid were added to a final volume of 250 µL per plate. The GenJet and plasmid DNA solutions were mixed and added to the cells. After 24 hours post-transfection, the supernatant was collected, centrifuged at 1800 rpm for 5 minutes, and filtered using a 0.22

μm filter. The VLPs were then centrifuged over an Optiprep gradient using high speed ultracentrifugation, as previously described.[162]

4.2.3 Production of ADA-CM-V4 VLPs

ADA-CM-V4 cells were provided by Michael B. Zwick (Scripps Institute) and maintained in DMEM with 10% FC3, 1% Pen-Strep, and 2 μg/mL puromycin. VLPs were produced via transient transfection of ADA-CM-V4 cells using GenJet and 4 μg of HIV-1 Gag plasmid as described above. These VLPs (denoted as V4-VLPs) were purified using the same method as described above.

4.2.4 Production of HTLV-1 VLPs

HTLV-1 VLPs were produced via GenJet transfection of 293T cells as described above with a 10:1 (m/m) ratio of HTLV-1 Env: HTLV-1 Gag plasmid DNA and purified as described above.

4.2.5 Gold immunolabeling of virus-like particles

Gold immunolabeling was completed following reported methods.[163] Briefly, TEM grids (TedPella, Carbon Type B, 300 mesh) were glow discharged. 4 μL of VLPs diluted in PBS were added to the TEM grid and incubated for 5 minutes. The excess solution was then removed using filter paper. A 20 μL droplet of Milli-Q water was added to a piece of Parafilm. The TEM grid was placed on the droplet of water face down. In a humidified chamber, a 20 μL droplet of blocking buffer [99 mL PBS, pH 7.4 (Hyclone), 100 μL Tween 20 (Sigma Aldrich), and 1 mL 30% bovine serum albumin (BSA, IgG free: Sigma Aldrich)] was added to a piece of Parafilm. The EM grid was transferred to this droplet face down and incubated for 15 minutes. A 20 μL droplet of primary antibody (either anti-HIV-1 gp120 or anti-HTLV-1 gp46 antibodies) prepared in blocking buffer was then added to the

humidified chamber, and the EM grid was incubated on this droplet for 1-2 hours. The excess liquid was then removed, and the EM grid was washed by placing it on a droplet of washing buffer [100 mL PBS, pH 7.4 (Hyclone), 100 µL Tween 20 (Sigma Aldrich), and 100 µL 30% bovine serum albumin (BSA, IgG free: Sigma Aldrich)]. The grid was incubated for 3 minutes, and the excess liquid was then removed—this step was repeated a total of five times. Next, the EM grid was added to a droplet of secondary antibody prepared in blocking buffer for 1 hour (either 1:20 v/v dilution in blocking buffer of 6-nm colloidal gold AffiniPure Goat Anti-Human IgG or 1:20 v/v dilution in blocking buffer of 6-nm colloidal gold AffiniPure Donkey Anti-Mouse IgG). The EM grid was washed three times in Milli-Q water as described above. Lastly, negative stain (either 2% uranyl acetate or 2% uranyl formate) was added to the EM grid for 45 seconds, and the excess negative stain was removed using filter paper. The EM grid was then allowed to dry for 2 minutes before storage.

4.2.6 Transmission electron microscopy (TEM)

VLPs (without immunolabeling) were prepared by dropping 3 µL of VLPs onto an EM grid (carbon type B, 300 mesh grid; TedPella), followed by negative staining with 2% uranyl acetate or uranyl formate. To negative stain, a sample was washed in uranyl acetate or uranyl formate twice, followed by incubating the EM grid in uranyl acetate or formate for 45 to 120 seconds. The EM grid was further dried for 12 hours. TEM images were collected on a Tecnai T12 instrument operated at 80kV or an FEI Tecnai G^2 F30 Field Emission Gun Cryo-TEM.

4.3 Results

4.3.1 Gold immunolabeling strategy to quantify gp120 and gp46

We proposed gold immunolabeling as a method to quantify the number of gp120 and gp46 proteins on the surfaces of HIV-1 and HTLV-1, respectively. The gold immunolabeling strategy (Figure 17) first involved labeling with a primary antibody that targets Env protein (either gp120 on HIV-1 or gp46 on HTLV-1). Next, a GNP-conjugated secondary antibody was introduced. The immunolabeled samples were then imaged using TEM, as GNPs are readily visualized due to their high electron density.[164] The goal was first to validate the gold immunolabeling strategy using HIV-1 virus-like particles (VLPs) with varying amounts of Env, followed by structural evaluations of HIV-1 and HTLV-1.

4.3.2 HIV-1 Env on V4-VLPs can be visualized with and without immunolabeling

HIV-1 VLPs with varying amounts of Env were first made to validate the gold immunolabeling method. The ADA-CM-V4 cell line was used to produce VLPs with high levels of Env (denoted as V4-VLPs), while the 293T cell line was used to produce VLPs with low levels of Env.[136] The V4-VLPs are reported to have an average of approximately 127 Env trimers per VLP (as determined by TEM), while HIV-1 VLPs from 293T cells have an average of roughly 2 Env trimers per VLP.[136]

As a control, we followed the methods of Stano et al. to determine the number of Env proteins without immunolabeling.[136] The V4-VLPs were negatively stained with 2% uranyl acetate and imaged using TEM, as shown in Figure 18. From these images, the presence of Env can be directly visualized using negative staining due to the high number of Env proteins present. However, quantification from these images proved difficult due to

the collapsed structure of the VLPs, which frequently occurs due to drying of the EM grid or different ionic concentrations.[165,166]

The V4-VLPs were then gold immunolabeled for Env (Figure 19). Gold immunolabeling was completed using different primary antibody (2G12) dilutions, including 1:100 and 1:1000 dilutions in blocking buffer (v/v) and a secondary antibody dilution of 1:20 in blocking buffer (v/v). A dense coating of GNPs was observed on the surface of some VLPs, consistent with the unlabeled VLPs and previous results showing a high level of Env on the VLP surface.[136] However, some VLPs did not exhibit a uniform coverage of GNPs. GNPs were not observed on the background of the EM grid and, without primary antibody, no GNPs were observed on the VLPs (Figure 19e), suggesting specific labeling of Env. The average number of Env per VLP was found to be 147±45 (the GNPs were manually counted on VLPs that exhibited uniform immunolabeling, and the resulting number was doubled to account for both faces of the VLPs). This number was consistent with the 127±31 Env per VLP previously reported.[136]

4.3.3 Gold immunolabeling of HIV-1 VLPs is not robust

The number of Env proteins on VLPs produced from 293T cells (~2±4 Env per VLP) is more similar to native HIV (~7-14) as compared to the V4-VLPs (127±31).[133,135,136,167] For this reason, VLPs produced from 293T cells were also gold immunolabeled. The HIV-1 VLPs were immunolabeled with varying concentrations of the 2G12 primary antibody, including dilutions of 1:10, 1:100 (v/v in blocking buffer), and without primary antibody. A corresponding secondary antibody dilution of 1:20 (v/v in blocking buffer) was used for all conditions. The immunolabeled HIV-1 VLPs are shown in Figure 20. For the 1:10 2G12 dilution, no immunolabeling of Env was observed on the

HIV-1 VLPs (Figure 20a). The 1:100 2G12 dilution showed very few GNPs on VLPs; however, most VLPs did not have immunolabeled Env (Figure 20b). Additionally, no immunolabeling was observed without the primary antibody (Figure 20c). These data indicated that the immunolabeling of HIV-1 VLPs was not robust, which may be due to the low number of Env proteins on HIV-1 VLPs produced from 293T cells. More work needs to be completed to optimize the immunolabeling procedure.

4.3.4 Gold immunolabeling of HTLV-1 VLPs is not robust

HTLV-1 or HTLV-1 VLPs have not been previously examined for the quantity and distribution of Env. Here, HTLV-1 VLPs were gold immunolabeled using a primary antibody targeting gp46 with dilutions in blocking buffer (v/v) of 1:10 and 1:50 and a corresponding GNP secondary antibody concentration of 1:20 (v/v in blocking buffer). The immunolabeled HTLV-1 VLPs are shown in Figure 21. EM images at both primary antibody concentrations did not show evidence of specific immunolabeling of Env on the VLPs, similar to the results observed for HIV-1 VLPs.

4.4 Discussion

The goal of this work was to quantify Env on HIV-1 and HTLV-1 using a gold immunolabeling strategy. The quantification and distribution of Env glycoprotein on HIV-1 virions have previously been studied using high-resolution 3D cryo-electron tomography.[133,167] However, this technique requires specialized equipment. Therefore, gold immunolabeling labeling was used because it is a more facile method as GNPs are readily visualized through TEM at lower resolutions. Gold immunolabeling was expected to allow higher throughput analyses to explore the glycoprotein distributions on HIV-1 and HTLV-1.

To validate the gold immunolabeling strategy, VLPs with varying numbers of Env were immunolabeled. V4-VLPs, which exhibit a high number of Env, were amenable to immunolabeling, and the number of Env per VLP was consistent with previously reported values.[136] However, HIV-1 VLPs and HTLV-1 VLPs produced from 293T cells did not show specific immunolabeling. This suggests that the number of Env trimers per VLP may be too low to observe consistent labeling, or incorporation of Env in VLPs may be non-homogenous. These results suggest that the gold immunolabeling procedure may need to be optimized, which is further discussed.

Optimization of the immunolabeling procedure may be necessary to quantify Env on HIV-1 and HTLV-1. As an alternative to electron microscopy, future work should first use fluorescence microscopy. Fluorescence microscopy offers a faster imaging method to screen different parameters for immunolabeling, as it has a wider field of view during imaging. Fluorescently conjugated secondary antibodies are commercially available, and VLPs with fluorescently labeled Gag have previously been developed.[152,158] Colocalization events of the fluorescently labeled antibody and VLP would allow a facile method to screen antibodies and antibody concentrations. Although the fluorescent-based system would not be quantitative, this approach would show whether VLPs are immunolabeled and the corresponding percentage of labeled VLPs. This would be a better method to optimize the parameters of immunolabeling as gold immunolabeling and imaging with TEM are more costly and time-consuming.

An alternative to gold immunolabeling for determining the quantities of Env on HIV-1 and HTLV-1 virions is to use high-resolution imaging methods. Previous studies with HIV-1 virions have been completed using high-resolution 3D cryo-electron

tomography. Cryo-reconstructions of HIV-1 and simian immunodeficiency virus (SIV) were conducted to show the distribution and quantify Env.[133,167] Additionally, high-resolution fluorescence imaging, such as stimulated emission depletion super-resolution fluorescence microscopy (sSTED-FCS), is another approach to quantify Env and determine Env distribution on virions.[169,170] Previous work by Chojnacki et al. determined the distribution of Env on budding virions and quantified the number of Env on HIV-1.[170] Access to high-resolution imaging instrumentation is limited, but nevertheless, these are promising methods to quantify Env on HIV-1 and HTLV-1.

4.5 Conclusions

Overall, this work aimed to quantify Env on HIV-1 and HTLV-1 and characterize its distribution using a GNP immunolabeling strategy. In this work, V4-VLPs, which have high levels of Env, were robustly immunolabeled. Additionally, the number of GNPs on the surface of the V4-VLPs were consistent with the quantity of Env previously reported. On the other hand, HIV-1 and HTLV-1 VLPs had no specific immunolabeling events, which may be due to the low quantity of Env on the viral surface. These findings indicate that gold immunolabeling has potential but may require further optimization for biologically relevant viral particles with low levels of Env protein.

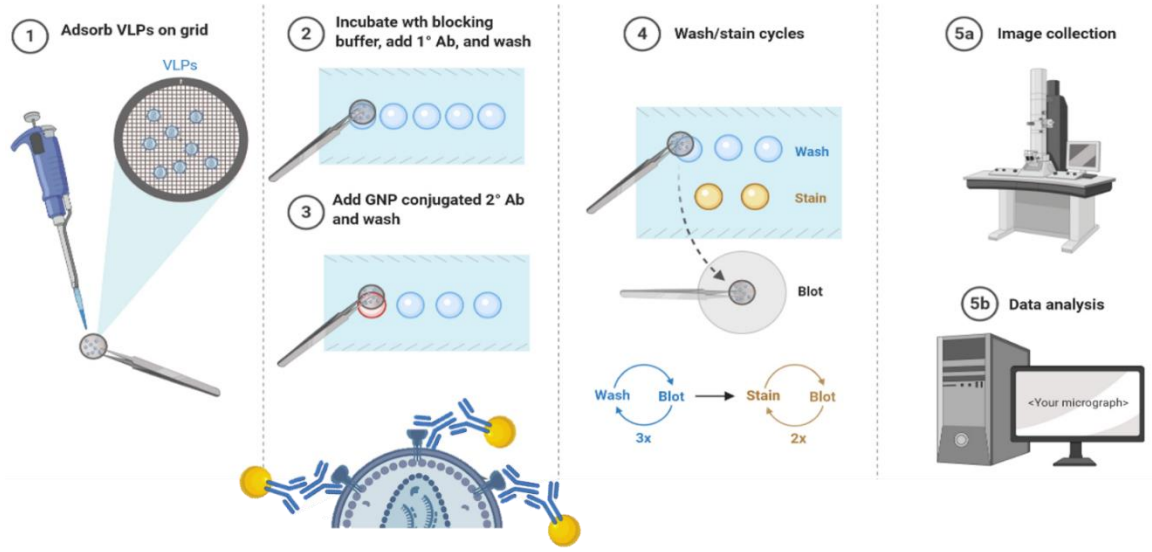

Figure 17. Scheme for nanoparticle immunolabeling strategy. VLPs are first deposited on an EM grid, followed by blocking with a blocking buffer, incubating with primary and secondary antibodies, and negative staining. Inset shows gold immunolabelled VLP. The grids were then imaged using TEM. This image was adapted from "Negative-Stain Transmission Electron Microscopy" by BioRender.com (2021). Retrieved from https://app.biorender.com/biorender-templates.

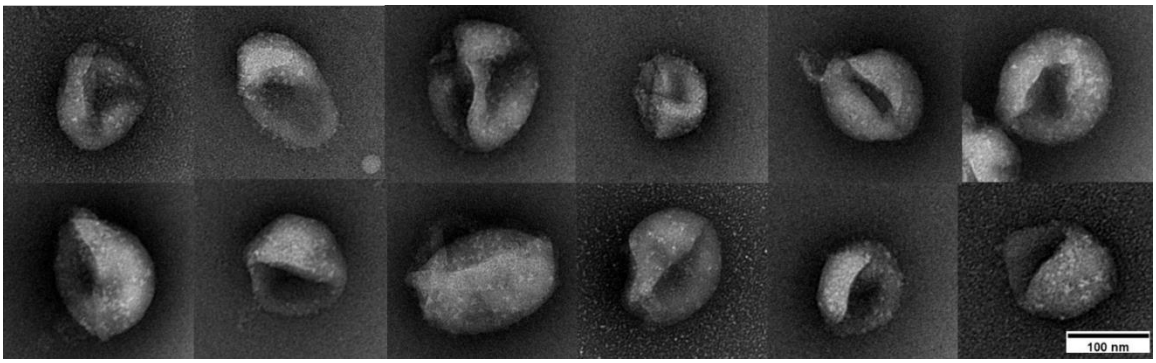

Figure 18. Negative staining of V4-VLPs. The negatively stained V4-VLPs allow for visualization of Env. The less electron dense regions (white regions) on each VLP are Env protein. Scale bar is 100 nm.

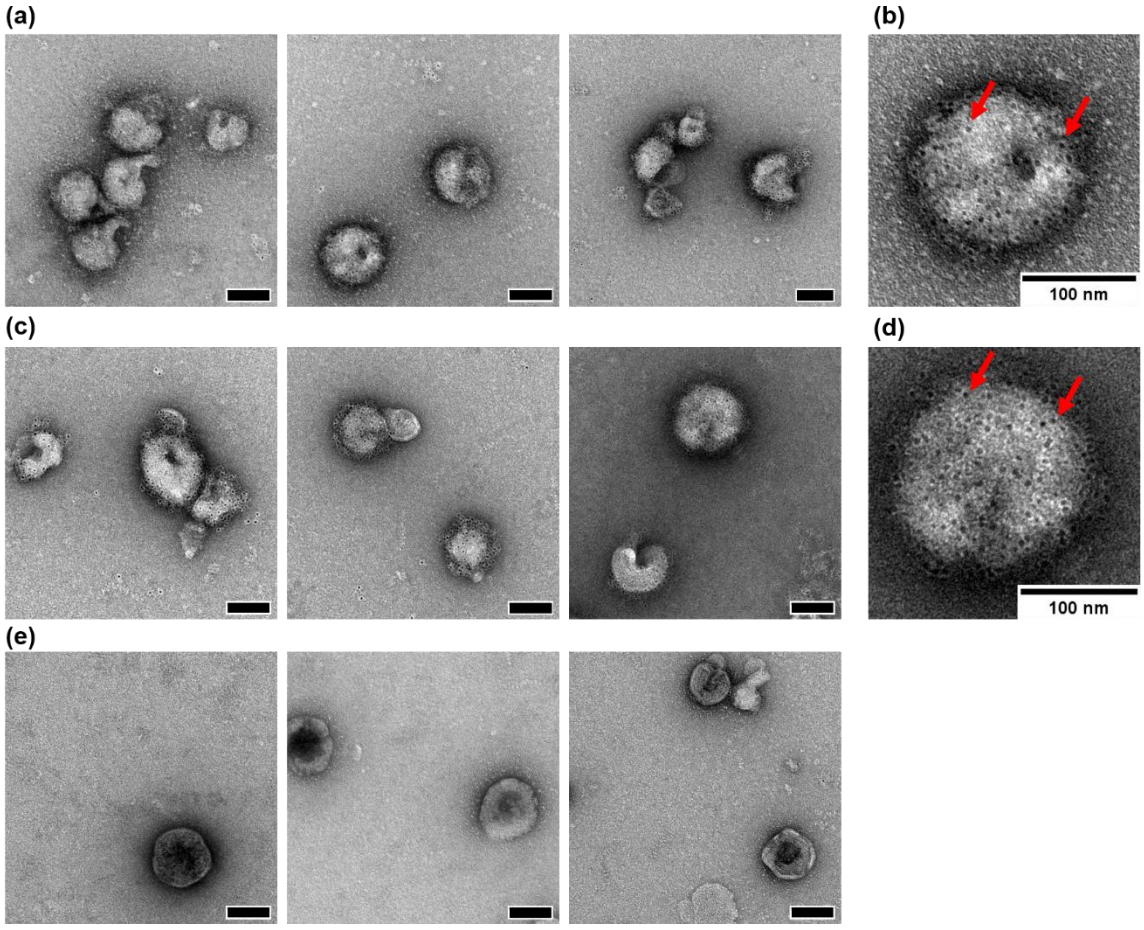

Figure 19. Gold immunolabeled V4-VLPs. V4-VLPs immunolabeled with (a) 1:100 and (c) 1:1000 primary antibody dilutions in blocking buffer. Higher magnification images of gold immunolabeled V4-VLPs with (b) 1:100 and (d) 1:1000 primary antibody. Red arrows are used to highlight the GNPs. (e) V4-VLPs immunolabeled without primary antibody (negative control). Scale bar is 100 nm.

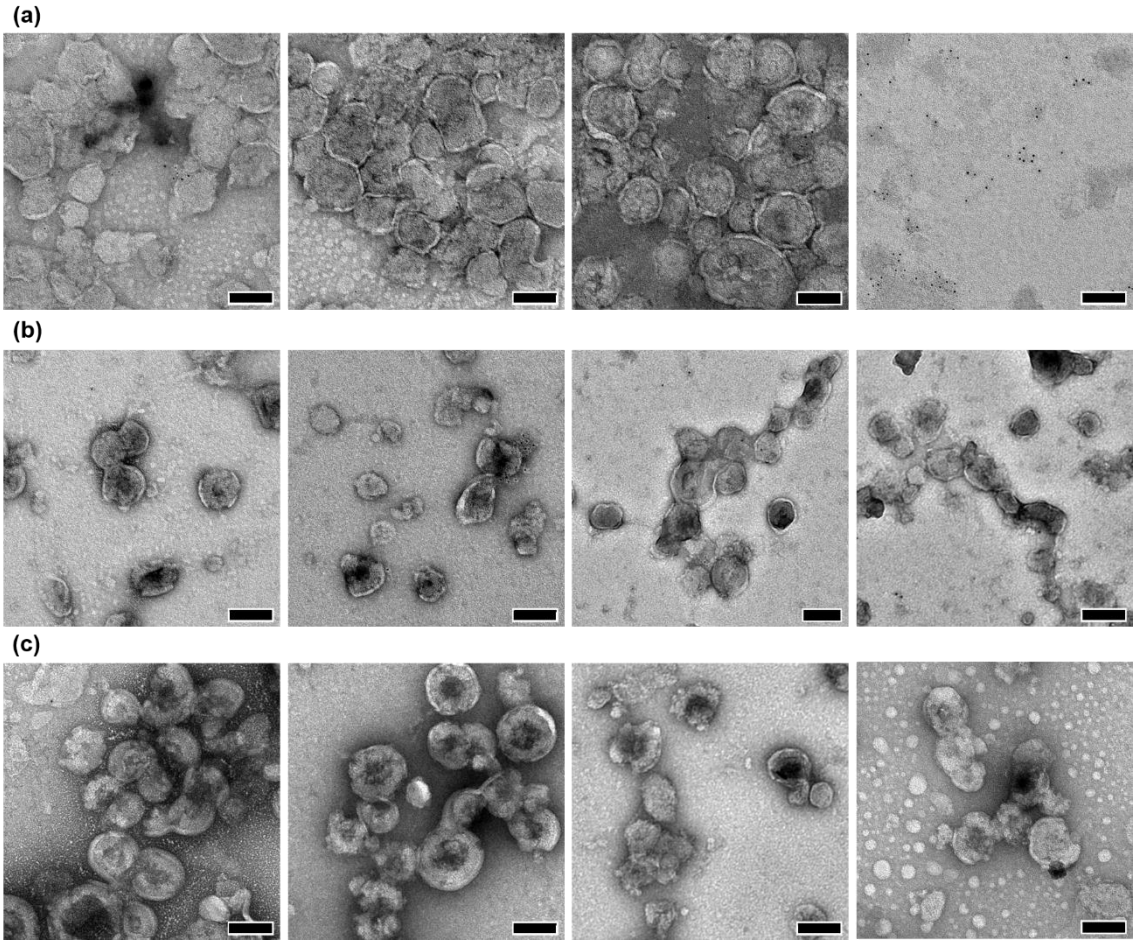

Figure 20. Gold immunolabeled HIV-1 VLPs produced from 293T cells. VLPs immunolabeled with (a) 1:10 and (b) 1:100 primary antibody dilutions in blocking buffer. (c) VLPs immunolabeled without primary antibody (negative control). Scale bar is 100 nm.

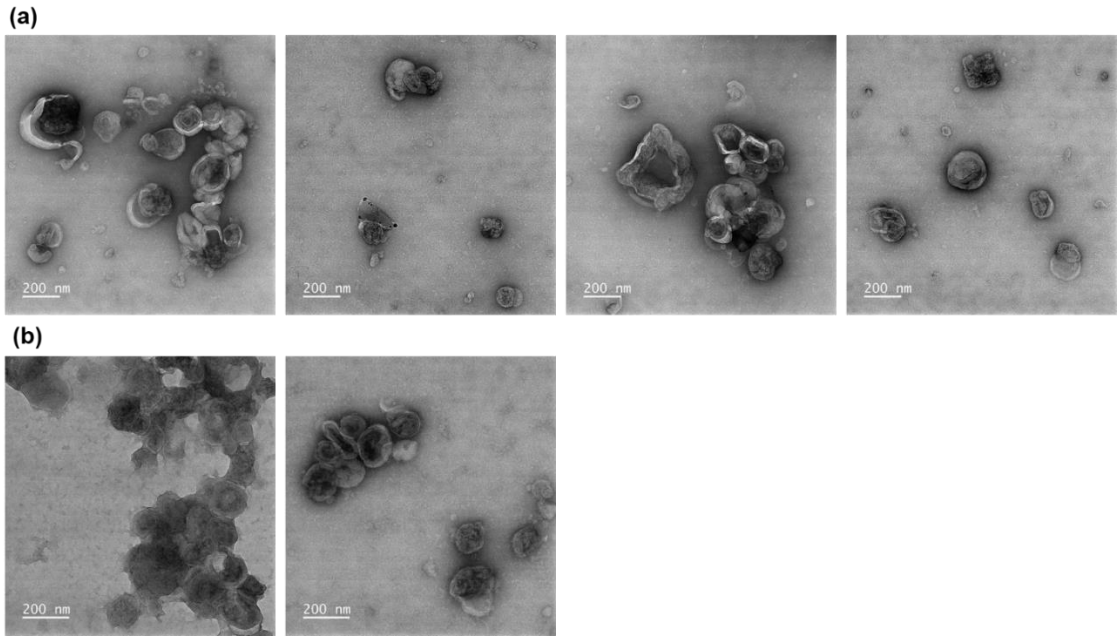

Figure 21. Gold immunolabeled HTLV-1 VLPs produced from 293T cells. VLPs were immunolabeled with (a) 1:50 and (b) 1:10 primary antibody dilutions in blocking buffer. Scale bar is 200 nm.

Chapter 5. A novel biodegradable and implantable elastomer

This work is from the following: Allison Siehr, Craig Flory, Trenton Callaway, Robert Schumacher, Ronald A. Siegel, and Wei Shen. "A novel biodegradable and implantable elastomer." (2021), in submission.

Synopsis

Biodegradable and implantable materials having elastomeric properties are highly desirable for many biomedical applications. Here we report that poly(lactide)-*co*-poly(β-methyl-δ-valerolactone)-*co*-poly(lactide) (PLA-PβMδVL-PLA), a thermoplastic triblock poly(α-ester), has combined favorable properties of elasticity, biodegradability, and biocompatibility. This material exhibits excellent elastomeric properties in both dry and aqueous environments. Elongation at break is approximately 1000% and stretched specimens completely recover to their original shape after force is removed. The material is degradable both *in vitro* and *in vivo*; it degrades more slowly than poly(glycerol sebacate) and more rapidly than poly(caprolactone) *in vivo*. Both the polymer and its degradation product show high cytocompatibility *in vitro*. Histopathology analysis of PLA-PβMδVL-PLA specimens implanted in the gluteal muscle of rats for 1, 4, and 8 weeks revealed similar tissue responses as compared with poly(glycerol sebacate) and poly(caprolactone) controls, two widely accepted implantable polymers, suggesting that PLA-PβMδVL-PLA has favorable *in vivo* biocompatibility as an implantable material. The thermoplastic nature allows this elastomer to be readily processed, as demonstrated by facile fabrication of substrates with topographical cues to enhance muscle cell alignment. These properties collectively make this polymer potentially highly valuable for applications such as medical devices and tissue engineering scaffolds.

5.1 Introduction

Biodegradable and implantable materials having elastomeric properties are highly desirable for many biomedical applications such as medical devices, tissue engineering scaffolds, and drug delivery devices.[171–174] Biocompatible and biodegradable polyesters, such as polycaprolactone (PCL), polylactic acid (PLA), polyglycolic acid (PGA), and their copolymers, have been used in many FDA-approved implantable devices.[171,175–177] However, these materials are stiff and non-elastomeric.[171,178,179] They have high Young's moduli (PCL: 0.15-0.33 GPa; PLA: 1.9-2.4 GPa; PGA: 7-14 GPa; PLGA: 1.4-2.8 GPa)[171] and small yield strains (PCL: 7.0%; PLA: 1.8-4.0%; PLGA: 0.4-2%),[180–183] beyond which the materials do not recover from deformation. Elongation at break values are low for PLA (2-6%), PGA (15-25%), and PLGA (3-10%).[171,180] The mechanical properties of these polyesters are not ideal for applications in which materials interface with soft tissues, which have elastic moduli on the order of 0.1 kPa to 1 MPa,[184,185] and particularly with those subjected to large and dynamic strains. Mechanical mismatch between tissue and an adjacent implant could greatly affect post-implantation healing and remodeling processes, possibly leading to failure of the implant.[55,171,186,187] Soft and elastomeric materials that can be easily stretched with a large, recoverable strain are highly desirable to address this problem.[183,186,188–190]

Poly(glycerol sebacate) (PGS) and poly(diol citrate) (PDC) are two of the most widely reported materials having collective properties of elasticity, biodegradability, and biocompatibility.[171,191] However, PGS and PDC are both thermosetting polyesters synthesized through polycondensation and curing by the reaction between carboxyl and hydroxyl groups, which is typically conducted at a relatively high temperature under

vacuum for an extended period of time.[171,188,191] The thermosetting nature of PGS and PDC imposes limitations on material processing; the harsh synthesis conditions make it challenging to incorporate bioactive molecules required for certain applications.[172,191–193] In addition, it has been reported that PGS with low modulus exhibits cytotoxicity.[194] Finally, materials synthesized by different authors under similar conditions do not have consistent properties, suggesting that such processes offer poor synthetic control.[195]

Elastin-based elastomers are also biodegradable, and they have been studied for various biomedical applications.[196–199] [2]These elastomers are prepared by chemically crosslinking animal-derived soluble elastin, recombinant human tropoelastin, or elastin-like polypeptides. Therefore, elastin-based elastomers are also thermosetting materials. These protein-based elastomers are expensive to produce. In addition, when protein-based materials are used as implantable materials, they generally raise concerns of immunogenicity, which needs to be carefully addressed.[171]

Thermoplastic polymers potentially have advantages over thermosetting polymers in allowing more facile material processing and better synthetic control,[171] and therefore thermoplastic elastomers that can be used as implantable materials are highly attractive. It has been reported that random copolymerization of caprolactone with glycolic acid or lactic acid yields elastomers, in which chain entanglements possibly serve as physical crosslinks.[171,200–202] However, random copolymers typically have poorly controlled molecular structures and broad molar mass distributions.[203] Thermoplastic multiblock poly(ester-urethane)s composed of PLLA and PCL blocks have also been reported to be elastomers.[187] However, these materials have Young's moduli greater than 30 MPa,[187] much stiffer than soft tissues.[184,185]

Thermoplastic poly(lactide)-*co*-poly(β-methyl-δ-valerolactone)-*co*-poly(lactide) (PLA-PβMδVL-PLA) triblock polyesters exhibit elastomeric properties.[204] These materials are highly stretchable and recover nearly completely after force is removed. The elastomeric properties are provided by the PβMδVL midblock, which is amorphous and has a low glass transition temperature (-51 °C). The PLA endblocks form physical junctions and provide mechanical strength and modulus. These polymers can be synthesized using well controlled ring opening transesterification polymerization, which allows molecular architecture, molar mass, and composition of triblock polymers to be well controlled and easily tuned.[204,205] This further allows controllable and tunable material properties, including mechanical properties and polymer degradation rates.[204] In addition, PLA-PβMδVL-PLA polymers can be synthesized through an economically viable route,[204] and their thermoplastic nature makes these polymers easily processable.[171]

However, it has never been reported whether PLA-PβMδVL-PLA polymers are suitable for biomedical applications, particularly as implantable materials. We hypothesized that these polyester-based materials would retain elastomeric properties in an aqueous environment and exhibit biocompatibility comparable to that of PGS and PCL. In this study, we examined the elastomeric properties of a PLA-PβMδVL-PLA polymer that has a Young's modulus of approximately 1 MPa in both dry and PBS conditions. We also examined degradation and biocompatibility of this material *in vitro* and *in vivo*. To demonstrate the ease of material processing, we fabricated cell culture substrates with topographical cues and examined muscle cell alignment on these substrates.

5.2 Experimental Section

5.2.1 Synthesis of β-methyl-δ-valerolactone

β-methyl-*δ*-valerolactone (βMδVL) was synthesized from 3-methyl-1,5-pentanediol as previously reported.[206] Briefly, 3-methyl-1,5-pentanediol (1 L; TCI America) and copper chromite (50 g, Sigma Aldrich) were added to a 2L two neck, round bottomed flask. The flask was fitted with a thermometer adapter in one neck and a Dean-Stark apparatus coupled to a condenser in the other neck. The condenser was connected with a bubbler filled with silicone oil. The flask was heated to 240 °C while stirring, and the reaction was continued for 20 hours.

After cooling, the product was purified via four fractional distillations under reduced pressure; during each distillation, the initial distillate collected at 38 °C-54 °C and 53.3 Pa (approximately 5%) was discarded, and the βMδVL product was collected at 55 °C and 53.3 Pa. The first fractional distillation was performed for the crude product over copper chromite. To further remove a minor impurity, 4-methyl-3,4,5,6-tetrahydro-2H-pyran-2-ol (which could be detected at 5.3 ppm in ^{1}H NMR spectrum), phosphorus pentoxide (5 g, Sigma Aldrich) was added to the product collected in the first distillation and stirred at 120 °C for 12 hours to dehydrate the impurity, followed by a second fractional distillation. To thoroughly remove water, the collected βMδVL was dried over calcium hydride for 2 days, followed by another fractional distillation; this drying step was repeated twice. ^{1}H NMR was used to confirm high purity of βMδVL. ^{1}H NMR shifts for βMδVL (500 MHz, $CDCl_3$, 25 °C): δ 4.40 (−O-C**H$_2$**-CH_2−); 4.26 (−O-C**H$_2$**-CH_2−); 2.66 (−CO-C**H$_2$**-CH(CH_3)−); 2.12 (−CO-C**H$_2$**-CH(CH_3)−); 2.10 (−CO-CH_2-C**H**(CH_3)−); 1.95 (−CH(CH_3)-C**H$_2$**-CH_2-); 1.54 (−CH(CH_3)-C**H$_2$**-CH_2−); 1.08 (−CH(C**H$_3$**)-CH2-CH2−).

5.2.2 Synthesis and purification of poly(β-methyl-δ-valerolactone)

Poly(*β*-methyl-*δ*-valerolactone) (PβMδVL) was synthesized through solvent-free ring-opening polymerization of βMδVL at room temperature as previously reported.[205] All the reagents and glassware were dried thoroughly prior to use, and the reaction was set up in a glove box with inert atmosphere. The monomer βMδVL (100 g) and the initiator 1,4-benzenedimethanol (BDM, Acros Organics, 138 mg) were added to a pressure vessel and stirred until BDM was completely dissolved, followed by addition of the catalyst diphenyl phosphate (DPP, Sigma Aldrich) at a monomer:catalyst molar ratio of 400:1. The amount of BDM added in the reaction mixture was determined from the desired molar mass of 100 kDa for PβMδVL and an assumption of 85% conversion. The pressure vessel was sealed and polymerization was continued for 20 hours at room temperature, followed by quenching with triethylamine (Macron Fine Chemicals) at a triethylamine:catalyst molar ratio of 5:1. To purify PβMδVL, the reaction mixture was dissolved in dichloromethane and the solution was added in cold methanol dropwise while stirring to precipitate the polymer, followed by drying the polymer under vacuum for 48 hours. Success of polymerization and polymer purity were verified by ^{1}H NMR. The percentage of monomer conversion was determined from the ^{1}H NMR spectrum of unpurified product according to the following equation:

$$\frac{Intregral\ of\ P\beta M\delta VL\ peak}{Integral\ of\ \beta M\delta VL\ peaks + Integral\ of\ P\beta M\delta VL\ peak} * 100 = \%\ conversion \qquad Equation\ 7$$

in which the PβMδVL peak at 4.12 ppm corresponds to the two methylene protons (−O-C**H$_2$**-CH$_2$−) and the βMδVL peaks at 4.40 ppm and 4.26 ppm correspond to the two methylene protons adjacent to the ester group (−O-C**H$_2$**-CH$_2$−). Size exclusion chromatography coupled with multi-angle laser light scattering (SEC-MALLS) was used

to determine molar mass of synthesized PβMδVL. ^{1}H NMR shifts for PβMδVL (500 MHz, $CDCl_3$, 25 °C): δ 4.12 (−O-C**H$_2$**-CH_2−); 2.31 (−CO-C**H$_2$**-CH(CH_3)−); 2.18 (−CO-C**H$_2$**-CH(CH_3)−); 2.08 (−CH_2-C**H**(CH_3)-CH_2−); 1.70 (−CH(CH_3)−C**H$_2$**−CH_2−); 1.53 (−CH(CH_3)-C**H$_2$**-CH_2−); 0.98 (−CH_2-CH(C**H$_3$**)-CH_2−). ^{13}C NMR shifts for PβMδVL (126 MHz, $CDCl_3$, 25 °C): δ 172.63 (-CH_2-**C**O-O-); 62.30 (-CH_2-**C**H_2-O-); 41.50 (-CH(CH_3)-**C**H_2-CO-); 35.11 (-CH_2-**C**H_2-CH(CH_3)-); 27.42 (-CH_2-**C**H(CH_3)-CH_2-); 19.51 (-CH_2-CH(**C**H_3)-CH_2-).

5.2.3 Synthesis of PLA-PβMδVL-PLA

PLA-PβMδVL-PLA was synthesized by extending the bifunctional telechelic PβMδVL (having one hydroxyl group on each end and serving as a macroinitiator) through ring-opening polymerization of lactide as previously reported.[205] Polymerization was conducted in a glove box with inert atmosphere. A solution of D,L-lactide (1M, Ortec) was prepared in anhydrous toluene (Sigma Aldrich) and added to PβMδVL in a pressure vessel (38.5 g PβMδVL, 9.2 g lactide, 98 mL toluene), and the mixture was heated to 145 °C while stirring until PβMδVL was fully dissolved. The catalyst tin (II) ethylhexanoate (Sigma Aldrich) was dissolved in anhydrous toluene (6.87 mg/mL) and added to the reaction mixture to a final mass of 20.7 mg. The reaction was carried out at 140 °C for 6 hours and quenched by cooling to room temperature.

To purify PLA-PβMδVL-PLA, the reaction mixture was dissolved in dichloromethane and the solution was added to cold methanol dropwise to precipitate the polymer. The precipitated polymer was dissolved in chloroform, followed by addition of activated charcoal (Sigma Aldrich) to thoroughly remove the catalyst. The charcoal was removed through filtration, first through Coarse Porosity Filter Paper (Fisher, P8) and then

through Glass Microfiber Filter Paper (GE Healthcare Life Sciences Whatman, 0.1 µm pore size), and the polymer was precipitated in cold methanol. Purification with activated charcoal was repeated twice. The polymer was dried for 24 hours in a fume hood, followed by drying under vacuum (101.5 kPa) for a minimum of 3 days to thoroughly remove the solvent.

PLA-PβMδVL-PLA synthesis was characterized by SEC-MALLS, ^{1}H NMR, and ^{13}C NMR. SEC-MALLS was used to determine molar mass of the synthesized polymer and its distribution; an increase in molar mass as compared with that of PβMδVL and a unimodal distribution were expected for successfully synthesized PLA-PβMδVL-PLA. ^{1}H NMR and ^{13}C NMR were used to confirm the presence of PLA endblocks. The weight percentage of PLA endblocks was determined from the ^{1}H NMR spectrum according to the following equation:

$$\frac{(integral\ of\ PLA\ peak * 144.1)}{(integral\ of\ P\beta M\delta VL\ peak * 114.2) + (integral\ of\ PLA\ peak * 144.1)} = \%\ PLA \qquad \textit{Equation 8}$$

in which the PLA peak at 5.16 ppm corresponds to the methine protons (-O-C**H**(CH_3)-CO-) and the PβMδVL peak at 4.12 ppm corresponds to the methylene protons (−O-C**H$_2$**-CH_2−). ^{1}H NMR shifts for PLA-PβMδVL-PLA (500 MHz, $CDCl_3$; 25 °C): δ 5.16 (−O−C**H**(CH_3)−CO−); 4.12 (−O-C**H$_2$**-CH_2−); 2.31 (−CO-C**H$_2$**-CH(CH_3)−); 2.18 (−CO-C**H$_2$**-CH(CH_3)−); 2.08 (−CH_2-C**H**(CH_3)-CH_2−); 1.70 (−CH(CH_3)−C**H$_2$**−CH_2−); 1.58 (−O−CH(C**H$_3$**)−CO−); 1.53 (−CH(CH_3)-C**H$_2$**-CH_2−); 0.98 (−CH_2-CH(C**H$_3$**)-CH_2−). ^{13}C NMR shifts for PLA-PβMδVL-PLA (126 MHz, $CDCl_3$, 25 °C): δ 172.63 (-CH_2-**C**O-O-); 169.40 (-**C**O-CH(CH_3)-); 69.00 (-CO-**C**H(CH_3)-O); 62.30 (-CH_2-**C**H_2-O-); 41.50 (-

CH(CH_3)-**C**H_2-CO-); 35.11 (-CH_2-**C**H_2-CH(CH_3)-); 27.42 (-CH_2-**C**H(CH_3)-CH_2-); 19.51 (-CH_2-CH(**C**H_3)-CH_2-); 16.65 (-CO-CH(**C**H_3)-O-).

5.2.4 NMR Spectroscopy

^{1}H NMR and ^{13}C NMR spectroscopy was performed at 25 °C on a 500 MHz Bruker Avance III HD with a SampleXpress spectrometer. ^{1}H NMR spectra were acquired with 64 scans, and ^{13}C NMR spectra were acquired with 128 scans. Solutions were prepared in 99.8% $CDCl_3$ with 1% (v/v) tetramethylsilane (TMS, Cambridge Isotope Laboratories) or D_2O (Cambridge Isotope Laboratories). Chemical shifts are reported in ppm with respect to the TMS standard (set to 0.00 ppm) or D_2O (set to 4.70 ppm) as a reference.

5.2.5 Size Exclusion Chromatography

Molar masses and dispersity of polymers were characterized by SEC-MALLS. The SEC instrument was equipped with three successive Phenomenex Phenogel-5 columns, a Wyatt Technology DAWN DSP multi-angle laser light scattering (MALLS) detector, and a Wyatt Optilab EX RI detector. Polymer samples were prepared at a concentration of 2 mg/mL, and 100 µg of polymer was injected for each analysis, which was performed at 25 °C with THF as the mobile phase (at a flow rate of 1 mL/min). Molar mass and dispersity were determined from chromatograms using Astra software (Wyatt Technologies). The dn/dc value of PLA-PβMδVL-PLA used for the analysis was 0.059 mL/g, as calculated from the weighted average of the dn/dc values of the PβMδVL and PLA blocks (0.0625 mL/g[205] and 0.042 mL/g,[207] respectively) using the weight percentages determined by ^{1}H NMR.

5.2.6 Polymer fabrication

Polymer films (approximately 0.3 mm thick) were fabricated for examining mechanical properties, *in vitro* cytotoxicity, and *in vitro* degradation. PLA-PβMδVL-PLA (1 g) was sandwiched between two Teflon sheets and compressed at 120 °C and 454 kg for 5 mins in a Carver press (Carver 4386 hot press) to yield a film. To fabricate PCL (Sigma Aldrich, M_n=45kDa) or PLA (NatureWorks, M_n=80kDa) controls, 10 mL of polymer solution (20% w/v, dissolved in chloroform) was poured into a 9-cm petri dish, followed by drying in a fume hood for 48 hours and then in a vacuum oven (101.5 kPa) for 3 days. The dried PCL or PLA was sandwiched between two Teflon sheets and compressed at 60 °C (for PCL) or 180 °C (for PLA) and 454 kg for 5 mins in the Carver press to yield a film. To fabricate the PGS control, 0.8 grams of Regenerez poly(glycerol sebacate) resin (Secant Group) was placed in a 5-cm glass petri dish and cured in a vacuum oven (101.5 kPa) at 130 °C for 3 days to yield a film. Specimens for mechanical testing were cut from films using a dog bone shaped dye (14 mm gauge length), and specimen thicknesses were measured with a caliper. Specimens for evaluating *in vitro* cytocompatibility and degradation were cut using 8 mm or 6 mm biopsy punches.

PLA-PβMδVL-PLA cell culture substrates with a microgroove surface topography were fabricated by thermocompression. A micropattern (10 μm groove/ridge width; 1 μm depth) was fabricated on a silicon wafer and transferred to poly(dimethyl siloxane) (PDMS) through molding as previously reported.[208] To transfer the micropattern from PDMS to PLA-PβMδVL-PLA, the patterned PDMS mold and a PLA-PβMδVL-PLA film (placed on a 18 mm×18 mm glass coverslip), respectively, were heated to 180 °C for 10 min on a platen of a Carver Press. The hot PDMS mold was then placed on the hot PLA-

PβMδVL-PLA film immediately (the patterned side of PDMS interfaced with PLA-PβMδVL-PLA), and a 250 g weight was placed on the top of the PDMS until cooled to room temperature, resulting in a patterned PLA-PβMδVL-PLA film. Non-patterned PLA-PβMδVL-PLA controls were fabricated through a similar thermocompression procedure in which the patterned PDMS was replaced with flat PDMS.

Disk shaped specimens (6 mm in diameter and 3 mm thick) of PLA-PβMδVL-PLA and controls (PGS and PCL) were fabricated for animal studies. To prepare PLA-PβMδVL-PLA specimens, 3 g of the polymer was placed in a mold cavity (16 mm in diameter and 3 mm high) sandwiched between two Teflon sheets and heated to 180 °C for 5 min in a Carver press (Carver 5370 AutoFour/4819 ASTM Molding Laboratory Press), followed by pressing at 363 kg for 10 min and with 2268 kg for 5 min sequentially. The polymer was cooled in the press using water injected cooling to room temperature, and then removed from the mold. PLA-PβMδVL-PLA disks were cut to size using a 6-mm biopsy punch. To prepare PCL specimens (Sigma Aldrich, 45kDa), polymer pellets were placed in a mold cavity (6 mm in diameter and 3 mm high) sandwiched between two Teflon sheets and heated to 85 °C for 5 min in the Carver press, followed by pressing at 363 kg for 10 min and at 2268 kg for 5 min sequentially. The polymer was cooled in the press using water injected cooling. To prepare PGS specimens, 8 g of Regenerez poly(glycerol sebacate) resin was placed in a 5 cm glass petri dish and cured in a vacuum oven (101.5 kPa) at 130 °C for 3 days to yield a 3 mm thick product. Disks 6 mm in diameter were punched out using a biopsy punch.

5.2.7 Tensile testing

Uniaxial extension tests of dry and wet specimens were performed at a strain rate of 10 mm/min on a Shimadzu AGS-X tensile tester to reveal elongation at break and ultimate tensile strength. Wet specimens were incubated in PBS at 37 °C for 24 hours and removed from the solution and patted dry with a KimWipe immediately prior to mechanical testing.

Tensile hysteresis tests in both dry and wet conditions were performed on a TestResources 100Q Tensile Tester equipped with a liquid bath. To perform tests in the wet condition, specimens were incubated in PBS at 37 °C for 24 hours, and then loaded in tensile tester grips and submerged in a bath filled with PBS for measurement. Tests were performed with a maximum strain of 50% and a strain rate of 10 mm/min for 20 cycles. Young's modulus was determined from the low strain region (0–5%) of the extension curve in the first cycle.[209] Hysteresis loss was calculated by dividing the area between the extension and contraction curves by the total area under the extension curve.[206]

Tensile set was measured for dry and wet specimens on a TestResources Q100 Tensile Tester following ASTM standard D412-16.[210] Specimens were stretched to 50% strain within 15 seconds, held at 50% strain for 10 minutes, and retracted to the starting position at a rate of 10 mm/min. After the grip was returned to its starting position, specimens were removed from the tensile tester followed by measuring specimen length using a caliper immediately and every 10 minutes afterwards. Tensile set was calculated by dividing the change in specimen length (with respect to the initial length) by the initial length**.**

5.2.8 In vitro *degradation of PLA-PβMδVL-PLA*

The initial mass of each polymer film (8 mm in diameter and approximately 0.3 mm thick) was recorded. Each film was soaked in Pen-Strep (5%) for 2 hours for sterilization, washed with PBS three times, placed in 6 mL of PBS or PBS containing 2000 IU/mL lipase from *T. lanuginosus* (Sigma Aldrich, >100,000 IU/mL), and incubated at 37 °C on a rotational shaker. PBS and lipase solution were both adjusted to pH 7.2 and sterilized by filtration prior to use. The solution in each sample was changed weekly. At a predetermined time point, a sample was rinsed with water, patted dry, and dried under vacuum to constant weight (no weight change for 3 days). The mass of the dried sample was recorded and compared with the initial mass. The sample was then dissolved in THF and subjected to SEC-MALLS analysis to reveal the change in molar mass.

5.2.9 In vitro *cytocompatibility of PLA-PβMδVL-PLA*

In vitro cytocompatibility of PLA-PβMδVL-PLA was examined by live/dead staining and Alamar Blue assay. PGS, PCL, PLA, and standard tissue culture polystyrene (TCPS) were used as controls. For live/dead staining, polymer films (8 mm in diameter) were adhered to glass coverslips with a thin layer of autoclaved vacuum grease, soaked in Pen-Strep (5%) for 2 hours for sterilization, washed with PBS three times, and placed in a well of a 24-well plate. The films and TCPS were soaked in culture medium (DMEM with 10% FBS and 1% Pen-Strep) overnight, followed by seeding NIH 3T3 fibroblasts at a density of 50,000 cells per well. Cells were cultured for 24 hours and stained with ethidium homodimer and calcein AM.

For Alamar Blue assay, polymer films (6 mm in diameter) were soaked in Pen-Strep (5%) for 2 hours for sterilization and washed with PBS three times. The films were

each affixed to the bottom of a well in 96-well plates by a thin layer of autoclaved vacuum grease. The films and TCPS were soaked in cell culture medium overnight, followed by seeding 3T3 fibroblasts or C2C12 cells at a density of 5,000 cells per well. The cells were cultured in 100 μL of phenol red-free culture medium for 24 hours, followed by Alamar Blue assay.

The result from Alamar Blue assay performed for cells cultured for 24 hours reflects combined effects of the material cytocompatibility and the cell adhesive property of a material. To decouple these effects and evaluate only material cytocompatibility, PLA-PβMδVL-PLA films and controls were coated with Matrigel (130 μg/mL in PBS) at 4 °C overnight, followed by seeding 3T3 fibroblasts at a density of 5,000 cells per well. In addition, culture medium was changed at 4 hours after cell seeding to remove non-adherent cells for all the samples, and Alamar Blue assay was performed at both 24 hours and 4 hours (as a normalization reference). The increase in cell number between 4 hours and 24 hours (the ratio of the Alamar Blue signals at these two time points) reflected material cytocompatibility. Experiments were performed in triplicate.

5.2.10 In vitro *cytocompatibility of the degradation product of PβMδVL*

The degradation products from complete hydrolysis of PβMδVL and PCL are 5-hydroxy-3-methyl-pentanoic acid and 6-hydoxy-caproic acid (or the carboxylate salts depending on the pH), respectively. To evaluate their cytocompatibility, these two compounds were synthesized through hydrolysis of β-methyl-δ-valerolactone and ε-caprolactone, respectively, as previously reported.[211] To synthesize sodium 5-hydoxy-3-methyl-pentanoatate, 0.117 mL of βMδVL was slowly added to 1.116 mL of aqueous solution containing 0.0077 moles of NaOH while stirring (1/5 of the βMδVL was added

every 30 minutes). To synthesize sodium 6-hydoxycaproate, 0.171 mL of ε-caprolactone was slowly added to 1.147 mL of aqueous solution containing 0.0077 moles of NaOH in a similar manner. Each mixture was stirred for 24 hours, and the pH value was checked to confirm complete consumption of NaOH. To remove unreacted lactone, the reaction mixture was mixed with dichloromethane (the volume ratio of DCM to the reaction mixture was 3:1) thoroughly in a separatory funnel, and allowed to separate for 6 hours. The carboxylate salt product in the water fraction was collected and lyophilized. Purity of the product was confirmed by ^{1}H NMR. ^{1}H NMR shifts for sodium 5-hydroxy-3-methylpentanoate (500 MHz, D_2O; 25 °C): δ 3.56 (-OH-C**H$_2$**-CH_2); 2.12 (-$CH(CH_3)$-C**H$_2$**-CO-); 1.86-1.90 (-$CH(CH_3)$-C**H$_2$**-CO-) and (-CH_2-C**H**(CH_3)-CH_2-); 1.48 (-CH_2-C**H$_2$**-$CH(CH_3)$-); 1.35 (-CH_2-C**H$_2$**-$CH(CH_3)$-); 0.83 (-CH_2-CH(C**H$_3$**)-CH_2-). ^{1}H NMR shifts for sodium 6-hydroxycaproate (500 MHz, D_2O; 25 °C): δ 3.51 (-HO-C**H$_2$**-CH_2-); 2.10 (-CH_2-C**H$_2$**-CO-); 1.49 (-OH-CH_2-C**H$_2$**-CH_2-); 1.47 (-CH_2-C**H$_2$**-CH_2-CO-); 1.25 (-CH_2-C**H$_2$**-CH_2-).

Cytocompatibility of sodium 5-hydroxy-3-methyl-pentanoate and sodium 6-hydoxy-caproate was evaluated by examining dose response curves of cell viability. Fibroblasts (3T3) were seeded in 96-well plates at a density of 5,000 cells per well and cultured in 100 µL of medium for 24 hours. The medium was replaced with serum-free DMEM medium containing a test compound or no test compound (control), and the samples were incubated for an additional 24 hours, followed by Alamar Blue assay. Fluorescence intensity of each sample containing a test compound was normalized to that of the control. A dose–response curve of normalized cell viability was plotted, and TD_{50}

(median toxic dose) was determined using GraphPad Prism 9.0. Experiments were performed in triplicate.

5.2.11 Live/dead staining and Alamar Blue assay

For live/dead staining, cells were incubated with ethidium homodimer and calcein AM (0.1% v/v) for 30 min in the dark, followed by washing with PBS. Samples were imaged with a 5× objective on a Zeiss Axio Observer inverted fluorescence microscope equipped with 470/525 and 550/650 excitation/emission filters. Polymer films were placed on a glass slide, with the side having cells facing down, for imaging. Cells cultured on TCPS were imaged directly in culture wells.

For Alamar Blue assay, cells were cultured in 96-well plates in 100 µL of phenol red-free culture medium. Alamar Blue reagent (Bio-Rad, 11 µL) was added to each well, followed by incubation in a tissue culture incubator for 4 hours. The culture medium in each sample (100 µL) was transferred to a new 96-well plate, and fluorescence intensity was measured at excitation/emission wavelengths of 560/590 nm using a BioTek Cytation 3 Cell Imaging Multi-Mode plate reader.

5.2.12 Characterization of C2C12 cells cultured on micropatterned PLA-PβMδVL-PLA

Patterned and non-patterned PLA-PβMδVL-PLA films processed through thermocompression were cut to 9 mm×9 mm in size, sterilized in 5% Pen-Strep for 2 hours, and washed with PBS three times. Each film was placed in a well of a 24-well plate and coated with Matrigel (130 µg/mL in PBS) at 4 °C overnight. The TCPS control was treated with Matrigel in the same manner. C2C12 cells were seeded at a density of 475,000 cells per well and cultured in growth medium (DMEM with 20% FBS, 1% Pen-Strep, and 1% Glutamax) for 24 hours, and then switched to differentiation medium (DMEM with 2%

Horse serum and 1% Pen-Strep) to initiate differentiation. Medium was changed gently every 2 days. At pre-determined time points, live/dead assay or immunofluorescent staining for myosin heavy chain (MHC) were performed.

For immunofluorescent staining, cells were fixed with 4% paraformaldehyde, permeabilized with 0.01% Triton X-100, and blocked with 5% bovine serum albumin. Samples were incubated with the primary antibody MF20 (targeting MHC, 1:100, Developmental Studies Hybridoma Bank) at 4 °C overnight, followed by washing with PBS three times. Samples were then co-stained with AlexaFlour-488 conjugated donkey anti-mouse IgG (1:50, Jackson ImmunoResearch) and Hoechst 33342 at room temperature for 2 hours, followed by washing with PBS three times. Samples were imaged with a 5× objective on a Zeiss Axio Observer inverted microscope equipped with 365/445 and 470/525 excitation/emission filters.

Fusion index, length, and alignment of myotubes were analyzed from the acquired images. Fusion index (the ratio of nuclei within myotubes that contain three or more nuclei to the total nuclei) was determined using MyoCount software.[212] Myotube length was characterized by manually drawing a line along a myotube between its two endpoints in FIJI/ImageJ and measuring the length of the line segment. Quantitative analysis of cell alignment with respect to microgroove direction was performed as previously reported.[208]

5.2.13 In vivo biocompatibility and degradation

Disk shaped specimens (6 mm in diameter and 3 mm thick) of PLA-PβMδVL-PLA and controls (PGS and PCL) were each weighed and sterilized with ethylene oxide gas. Specimens were implanted under the fascia of the right or left gluteal muscles of female Sprague-Dawley rats; animals having a PLA-PβMδVL-PLA specimen implanted on one

side had either a PGS or a PCL control on the other side. The surgical procedures and animal care followed an approved IACUC protocol in compliance with the regulations of the University of Minnesota and the NIH. Briefly, analgesic buprenorphine SR-LAB was administered for post-operative pain relief and the animals were anesthetized with isoflurane. In a sterile field, an incision was made in the skin of the flank over the gluteal muscle to expose the muscle, and a polymer specimen was implanted into the muscle. The incision was closed with a suture. Shams were performed with identical surgical procedures except that no specimen was implanted. At predetermined time points, animals were sacrificed, and specimens were harvested for examination of *in vivo* biocompatibility or degradation.

For biocompatibility evaluation, three specimens, each with surrounding gluteal muscle attached, were harvested at every time point for each polymer. Specimens were fixed in 10% neutral buffered formalin and stained with Hematoxylin and Eosin (H&E), followed by histopathologic evaluation performed by a board-certified veterinary pathologist who was blinded to the identity of each slide. Samples were evaluated for inflammation, granulation tissue formation, foreign body giant cell formation, and thickness of the fibrovascular connective tissue capsule surrounding the implant.

For *in vivo* degradation evaluation, specimens were explanted (four for each polymer at every time point) and the surrounding tissue was completely excised. Each sample was washed with water extensively, patted dry with a KimWipe, and dried in a desiccator to constant weight (no weight change over 3 days). The mass of each sample was recorded and compared to the pre-implantation mass to determine mass loss. The

specimen was then dissolved in THF and subjected to SEC-MALLS analysis to assess change in molar mass of the explanted polymer.

5.2.14 Statistical analyses

Statistical analyses were performed using GraphPad Prism 9.0. Unpaired Welch's t-test, Welch's one-way ANOVA followed by Dunnett's multiple comparison post hoc test, Welch's one-way ANOVA followed by Games-Howell multiple comparison post hoc test, or two-way ANOVA followed by Tukey's HSD multiple comparison post hoc test was performed, as indicated in figure legends. Statistical significances are indicated as *p < 0.05, **p < 0.01, ***p < 0.001, and ****p < 0.0001.

5.3 Results and Discussion

5.3.1 A soft PLA-PβMδVL-PLA polymer was designed and synthesized

The objective of this study was to examine the feasibility of using PLA-PβMδVL-PLA elastomers for biomedical applications in which these polymers may interface with soft tissues or organs. It has been reported that matching mechanical properties between tissue and an adjacent implant benefits implant function.[55,190,213] Therefore, we focused on a soft PLA-PβMδVL-PLA material with Young's modulus of approximately 1 MPa, which could potentially interface with many soft tissues.[172,214–216] Mechanical properties of PLA-PβMδVL-PLA elastomers are affected by block compositions, and it has been reported that the Young's modulus of a PLA-PβMδVL-PLA polymer having a 70 kDa midblock and 16.8 kDa endblocks is 1.93 MPa.[204] We expected that a PLA-PβMδVL-PLA polymer with a 100 kDa midblock and 10 kDa endblocks would be softer.

The PLA-PβMδVL-PLA polymer with this designed structure was synthesized using a two-step method as reported previously.[204,205] The rubbery midblock, PβMδVL,

was synthesized through ring opening polymerization of βMδVL, followed by ring opening polymerization of lactide with the bifunctional telechelic PβMδVL as a macroinitiator to yield PLA-PβMδVL-PLA (Figure 22). The βMδVL monomer was synthesized from 3-methyl-1,5-pentanediol, as confirmed by ^{1}H NMR (Figure 23). Successful synthesis of PβMδVL from βMδVL was confirmed by ^{1}H NMR (Figure 24 and 25): the peaks corresponding to the two βMδVL methylene protons (−O-C**H$_2$**-CH$_2$−) at 4.40 ppm and 4.26 ppm decreased, and a single resonance peak corresponding to the two PβMδVL methylene protons (−O-C**H$_2$**-CH$_2$−) at 4.12 ppm was detected. The percentage of monomer conversion was 92%, as calculated from the ^{1}H NMR spectrum of the non-purified sample (Figure 24) according to Equation 7. Successful synthesis of PβMδVL was further confirmed by ^{13}C NMR (Figure 26). SEC-MALLS characterization of purified PβMδVL revealed the molar mass (M_n=97.4 kDa, M_w=116.3 kDa, Đ=1.19), which was close to the targeted molar mass of 100kDa.

Successful synthesis of PLA-PβMδVL-PLA was confirmed by ^{1}H NMR, ^{13}C NMR, and SEC-MALLS. The presence of PLA in the triblock polymer was confirmed by the chemical shift at 5.3 ppm corresponding to the methine proton in the ^{1}H NMR spectrum (Figure 27), and was further confirmed by three chemical shifts in the ^{13}C NMR spectrum (169.40 ppm (-**C**O-); 69.00 ppm (-**C**H(CH$_3$)-); 16.65 ppm (-CH(**C**H$_3$)-)) (Figure 28). The SEC chromatogram shifted to a shorter elution time (corresponding to larger molar mass) as compared with that of PβMδVL and showed a unimodal distribution, suggesting that PLA blocks were linked to the telechelic PβMδVL as opposed to formation of PLA homopolymer (Figure 29). The molar mass of PLA-PβMδVL-PLA revealed by SEC-MALLS (M_n=123.2 kDa, M_w=143.1 kDa, Đ=1.16) was close to the targeted molar mass

(10 kDa for each PLA endblock). The weight percentage of the PLA block determined from the ^{1}H NMR spectrum was 15.9% according to Equation 8.

5.3.2 The PLA-PβMδVL-PLA polymer exhibits elastomeric properties in both dry and wet environments

All mechanical property tests were performed in both dry and wet (PBS) conditions. Tensile hysteresis tests of 20 cycles, the stress-strain curves of which are shown in Figure 30a, revealed Young's modulus and hysteresis loss. Young's moduli were 1.11 ± 0.20 MPa and 0.715 ± 0.10 MPa for the dry and wet conditions, respectively, as determined in the low strain region (0–5%) of the extension curve in the first cycle. These values are on the same order of magnitude as the moduli of many soft tissues.[172,214] In the dry condition, hysteresis loss was 40% after the first cycle and then stabilized at around 34% after the second cycle, a trend also observed for conventional rubber bands[217] (Figure 30b). Hysteresis loss of the polymer in the wet condition exhibited a similar trend, with values slightly higher than those in the dry condition: it was 44% after the first cycle and then stabilized at around 37% after the second cycle (Figure 30b).

Uniaxial extension tests were performed to characterize ultimate tensile strength and elongation at break. The stress-strain curves shown in Figure 30c revealed ultimate tensile strengths of 1.12 ± 0.24 MPa and 0.934 ± 0.05 MPa and elongation at break values of 1065 ± 65.9 % and 931.7 ± 100.0 % for dry and wet conditions, respectively.

Tensile set, defined as the remaining strain after a specimen has been stretched and allowed to retract in a specified manner,[210] was measured to assess whether PLA-PβMδVL-PLA specimens could recover their shape completely after stretching. According to ASTM standard D412-16,[210] each specimen was stretched to 50% strain within 15 seconds, held

at 50% strain for 10 minutes, and retracted to the starting position at a rate of 10 mm/min. The specimen was removed from the tensile test apparatus, and remaining strain was measured at subsequent time points (Figure 30d). Initial tensile sets were 10% and 13% for the dry and wet conditions, respectively. After 10 minutes, tensile sets were approximately 4% for both conditions. Complete recovery was observed at approximately 40 minutes for both conditions.

Previous studies only reported mechanical properties of PLA-PβMδVL-PLA in the dry condition.[204] In the present study, we characterized mechanical properties of the polymer in dry and wet conditions in parallel to evaluate its potential use in biomedical applications, such as implantable devices and tissue engineering scaffolds. We found that Young's modulus, ultimate tensile strength, and elongation at break were slightly lower in the wet condition as compared with those in the dry condition, which may result from water plasticization as previously reported for wet amorphous poly(lactide-*co*-glycolide).[218] Importantly, we found that PLA-PβMδVL-PLA retained elastomeric properties in wet environments, as hysteresis loss and tensile set were similar between dry and wet conditions.

5.3.3 The PLA-PβMδVL-PLA elastomer exhibits excellent in vitro *cytocompatibility*

Cytocompatibility of PLA-PβMδVL-PLA was first examined by live/dead assay. Three biocompatible polymers, PCL,[54] PGS,[191,219] and PLA,[53] and standard tissue culture polystyrene (TCPS) were evaluated as controls. NIH 3T3 fibroblasts cultured for 24 hours on PLA-PβMδVL-PLA films exhibited high viability and normal morphology, similar to cells cultured on TCPS, and cell coverage was uniform across each entire culture substrate (Figure 31a). Cells cultured on PGS showed high viability and normal morphology in some

regions (as shown in Figure 31a), but cell coverage was not uniform on PGS substrates. Live/dead assay revealed that cells cultured on PLA-PβMδVL-PLA have similar or better viability as compared with those cultured on the controls (Figure 31a), suggesting that PLA-PβMδVL-PLA is highly cytocompatible *in vitro.*

In vitro cytocompatibility of PLA-PβMδVL-PLA was further quantitatively examined by Alamar Blue assay. Both 3T3 fibroblasts and C2C12 myoblasts cultured for 24 hours on PLA-PβMδVL-PLA films showed similar Alamar Blue fluorescence signals to those on PLA or TCPS controls (Figure 31b). 3T3 cells cultured on PLA-PβMδVL-PLA showed a slightly lower signal than those on PCL, but C2C12 cells showed similar signals on these two polymers. Interestingly, both cell types showed higher Alamar Blue signals on PLA-PβMδVL-PLA than those on PGS, a widely reported biodegradable and elastomeric material for biomedical applications. It has been reported that PGS with low Young's modulus (<0.5 MPa) exhibits some level of cytotoxicity.[194,195] In the current study, PGS was prepared under high vacuum (101.5 kPa) at 130 °C for 72 hours, and Young's modulus in the range of 1.0–1.2 MPa was expected.[189,194,195] However, PGS synthesis and processing have been reported to be highly variable and similar conditions have resulted in different material properties when carried out in different labs.[195]

The Alamar Blue fluorescence signal is related to the total cell number at the time of evaluation and reflects combined effects of material cytocompatibility and cell adhesive property of a material. To evaluate material cytocompatibility, all substrates were coated with Matrigel to minimize differences in cell adhesion. In addition, culture medium was changed 4 hours after cell seeding to remove non-adherent cells, and Alamar Blue assay was performed at both 24 hours and 4 hours (as a normalization reference). At 4 hours the

Alamar Blue signal on PLA-PβMδVL-PLA was similar to those on the controls; at 24 hours the Alamar Blue signal on PLA-PβMδVL-PLA was similar to those on TCPS, PCL, and PLA, but higher than that on PGS (Figure 31c). The increase in cell number between 4 hours and 24 hours (the ratio of the Alamar Blue signals at the two time points) on PLA-PβMδVL-PLA was similar to that on TCPS, PCL, and PLA and higher than that on PGS (Figure 31d), suggesting that PLA-PβMδVL-PLA supports cell viability as well as the biocompatible controls used in the study.

5.3.4 The PβMδVL degradation product is non-cytotoxic

To use degradable polymers as implantable materials, not only must the polymers themselves be biocompatible, but their degradation products must also be non-cytotoxic. The hydrolysis product of the endblocks, PLA, has been well studied and is generally regarded as safe by the FDA.[220] However, cytotoxicity of the degradation product from hydrolysis of PβMδVL has not been evaluated previously. In the current study, we examined cytotoxicity of sodium 5-hydroxy-3-methyl-pentanoate, which is the final product of PβMδVL degradation at physiological pH. The PCL degradation product, sodium 6-hydroxy-caproate, was evaluated as a control. These two compounds were synthesized by hydrolysing β-methyl-δ-valerolactone and ε-caprolactone, respectively, in NaOH solution as previously reported (Figure 32).[211] The chemical structure and purity of the products were confirmed using ^{1}H NMR (Figures 33 and 34).

Dose response curves of cell viability were similar for the two degradation products (Figure 35). The TD_{50} values for sodium 5-hydroxy-3-methyl-pentanoate and sodium 6-hydroxycaproate are 203.7±1.05 mM and 172.3±1.05 mM, respectively. PCL is a widely accepted implantable material used in many FDA approved products[54] and its degradation

product has been reported to be non-cytotoxic.[221] The higher TD_{50} value for sodium 5-hydroxy-3-methyl-pentanoate indicates that the PβMδVL degradation product is also non-cytotoxic. In addition, the degradation product from hydrolysis of PLA, lactic acid, has a TD_{50} value of 46.18 mM and is generally regarded as safe,[220,222] further suggesting that the PβMδVL degradation product is non-cytotoxic.

5.3.5 PLA-PβMδVL-PLA can be readily micropatterned to support C2C12 cell alignment

The thermoplastic nature of PLA-PβMδVL-PLA was expected to allow the polymer to be readily processable into a wide range of geometries and to enable facile incorporation of various topographical features. To demonstrate this advantage in material processing, we fabricated PLA-PβMδVL-PLA substrates with microgrooves (10 μm in groove and ridge width; 1 μm in depth) by pressing a mold of the desired pattern on a pre-processed PLA-PβMδVL-PLA film at an elevated temperature. The pattern was successfully transferred to the PLA-PβMδVL-PLA film through this simple thermocompression method (Figure 36a).

PLA-PβMδVL-PLA substrates with microgroove topography were used to culture C2C12 cells, an immortalized cell line of murine skeletal myoblasts. Live/dead assay for cells cultured for 5 days in differentiation medium revealed high cell viability on both patterned and non-patterned PLA-PβMδVL-PLA (Figure 36b), further confirming cytocompatibility of the polymer. Cells cultured on patterned substrates aligned along the groove direction throughout the entire culture area (9 mm×9 mm), consistent with previous reports that C2C12 cells align along 10 μm grooves on other materials.[223] Cells cultured on non-patterned substrates showed random orientations (Figure 36b). These results

suggest that the topography introduced through the simple thermocompression method was retained in culture medium and mediated cell behavior.

C2C12 cells cultured on patterned PLA-PβMδVL-PLA were further examined by immunofluoescence staining for total myosin heavy chain (MHC, a muscle differentiation marker), and cells cultured on non-patterned PLA-PβMδVL-PLA and TCPS were evaluated as controls. MHC^+ myotubes were observed on all the culture substrates on day 7 (Figure 36c). Quantitative analyses of myotube length, myogenic fusion index, and myotube alignment angles were performed on immunochemically stained samples. No statistical difference was observed in myogenic fusion index between different culture substrates, but myotube length on patterned PLA-PβMδVL-PLA was greater than that on the two controls (Figure 36d,e). Furthermore, myotubes aligned along the groove direction with an average angle of 4.03° ± 2.21, while those on the controls oriented randomly (Figure 36f and 37). These results further confirmed that the topography introduced through thermocompression was retained in cell culture medium and mediated cellular contact guidance responses to facilitate myotube formation and alignment.

5.3.6 The PLA-PβMδVL-PLA elastomer is degradable in vitro *and* in vivo

PLA-PβMδVL-PLA is a polyester and was expected to be hydrolysable. We first examined degradability of the PLA-PβMδVL-PLA elastomer by incubating specimens in PBS at 37 °C over 8 weeks, and PCL and PGS were used as controls. The decrease in molar mass between 0 and 8 weeks was insignificant for both PLA-PβMδVL-PLA and PCL (Figure 38a; PGS is a thermoset and was not evaluated for changes in molar mass). At 8 weeks mass loss was approximately 0.5%, 4.5%, and 10.7% for PLA-PβMδVL-PLA, PCL, and PGS, respectively (Figure 38a, Figure 39).

Since it is known that lipase accelerates hydrolysis of polyesters,[224,225] we further examined degradation of these polymers in lipase solution (lipase from *Thermomyces lanuginosus*, 2000 U/mL). Both PCL and PGS were completely degraded in lipase solution at 4 weeks, while little mass loss was observed for PLA-PβMδVL-PLA at 8 weeks (Figure 38b). However, a significant decrease in molar mass was observed for PLA-PβMδVL-PLA in lipase solution (approximately 32% decrease between 0 and 8 weeks, p-value<0.05), suggesting that hydrolysis occurred (Figure 38b). The slower degradation of PLA-PβMδVL-PLA in lipase solution as compared with PCL and PGS is likely related to its chemical structure, as it has been reported that enzymatic hydrolysis with fungal lipases is slower for polyesters with methyl groups.[226] It is worth noting that the *in vitro* enzymatic hydrolysis rate of a polyester does not necessarily correlate with its *in vivo* degradation rate. It has been reported that PCL specimens placed in a solution containing lipase from *Pseudomonas cepacia* completely degraded within 4 days, while the shape of PCL products implanted in rats remained unchanged after 24 months.[227–229]

We further examined degradation of PLA-PβMδVL-PLA specimens implanted in the gluteal muscle of rats for 1, 4, and 8 weeks. PCL and PGS specimens implanted for 8 weeks were evaluated as controls. At 8 weeks post-implantation, mass loss of PLA-PβMδVL-PLA was small, while the decrease in molar mass was evident, suggesting that biodegradation occurred *in vivo* (Figure 40). Most PGS specimens implanted for 8 weeks degraded, consistent with previous studies reporting rapid degradation of PGS *in vivo*.[183] The PCL control implanted for 8 weeks showed negligible degradation. These results suggest that PLA-PβMδVL-PLA degrades more slowly than PGS and more rapidly than PCL *in vivo*.

5.3.7 The PLA-PβMδVL-PLA elastomer exhibits in vivo *biocompatibility*

Histopathology analysis performed for polymer specimens implanted under the fascia of the gluteal muscle revealed that PLA-PβMδVL-PLA has *in vivo* biocompatibility comparable to that of PCL and PGS controls, two widely accepted implantable materials.[54,183,224] At 4 and 8 weeks, all the samples were present within the perimysium and surrounded by a thin capsule, which generally consisted of an outer layer of dense fibrovascular connective tissue with scant individual inflammatory cells (neutrophils and/or eosinophils, and lesser lymphocytes) and an inner layer of less organized, loose fibrovascular connective tissue admixed with variable numbers of histiocytes (Figure 41 and Figure 42). The only notable difference between samples was that PGS specimens tended to stimulate a more robust lymphocytic inflammatory response at 4 weeks (with prominent perivascular infiltrates in the perimysium and the outer layer of the fibrous capsule). The more notable tissue response of PGS is likely related to its faster degradation and production of a large amount of acidic degradation products during a relatively short period of time.[183,230] Capsule thickness was quantitatively assessed at 1, 4, and 8 weeks and also showed comparable results for the three polymers (Figure 43). A descriptive and semi-quantitative report of the assessment of inflammation, granulation tissue formation, foreign body reaction, and foreign body giant cell formation is shown in Table 6. Overall, healing and biocompatibility are similar for the three polymers, suggesting that PLA-PβMδVL-PLA has favorable *in vivo* biocompatibility as an implantable material.

5.4 Conclusions

A PLA-PβMδVL-PLA triblock polymer having Young's modulus of approximately 1 MPa, which is similar to the stiffness of many soft tissues, was

synthesized. This material exhibits elastomeric properties in both dry and wet environments. Elongation at break is approximately 1000%, and specimens stretched with a strain of 50% could completely recover to their original shape after force is removed. The elastomer is degradable both *in vitro* and *in vivo*; it degrades more slowly than PGS and more rapidly than PCL *in vivo*. Both PLA-PβMδVL-PLA films and the PβMδVL degradation product show excellent cytocompatibility *in vitro*. The tissue responses of PLA-PβMδVL-PLA specimens implanted in the gluteal muscle of rats are similar to those of PLA and PGS controls, suggesting that PLA-PβMδVL-PLA has favorable *in vivo* biocompatibility as an implantable material. In addition, the thermoplastic nature of this elastomer enables facile material processing. These properties collectively make this material potentially highly valuable for applications such as medical devices and tissue engineering scaffolds.

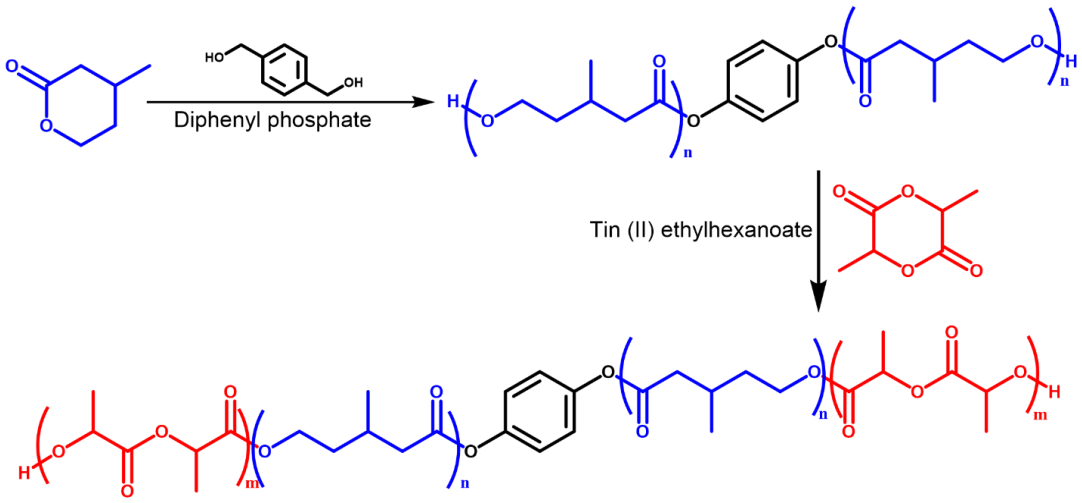

Figure 22. Synthesis of PLA-PβMδVL-PLA. PβMδVL was synthesized through ring opening polymerization of β-methyl-δ-valerolactone, followed by ring opening polymerization of lactic acid with the telechelic PβMδVL macroinitiator to yield PLA-PβMδVL-PLA.

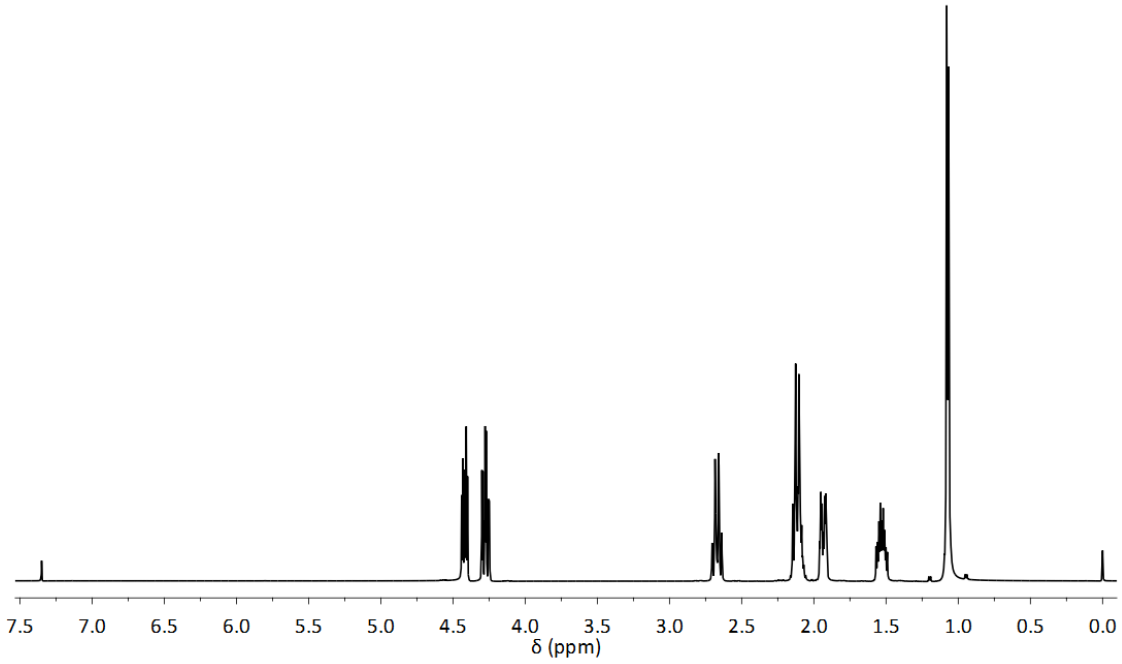

Figure 23. ^{1}H NMR spectrum of β-methyl-δ-valerolactone. ^{1}H NMR shifts for β-methyl-δ-valerolactone (500 MHz, CDCl3, 25 °C): δ 4.40 (−O-C**H$_2$**-CH$_2$−); 4.26 (−O-C**H$_2$**-CH$_2$−); 2.66 (−CO-C**H$_2$**-CH(CH$_3$)−); 2.12 (−CO-C**H$_2$**-CH(CH$_3$)−); 2.10 (−CO-CH$_2$-C**H**(CH$_3$)−); 1.95 (−CH(CH$_3$)-C**H$_2$**-CH$_2$-); 1.54 (−CH(CH$_3$)-C**H$_2$**-CH$_2$−); 1.08 (−CH(C**H$_3$**)-CH2-CH2−).

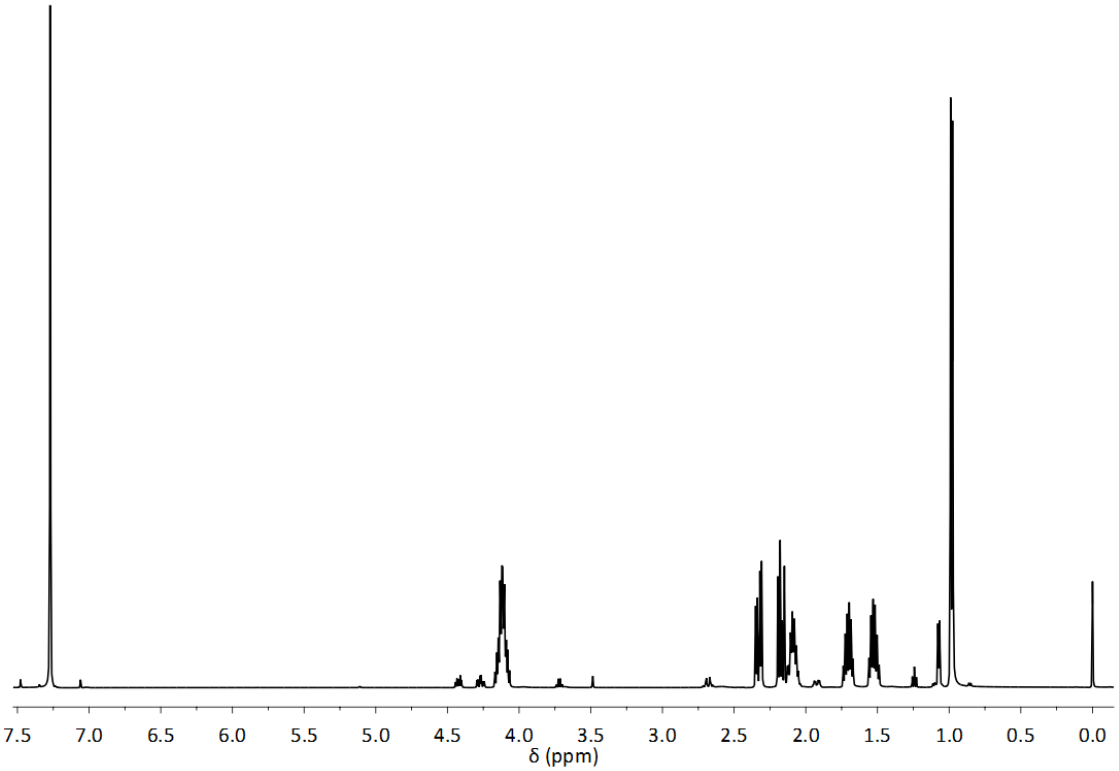

Figure 24. ^{1}H NMR spectrum of PβMδVL before purification. The percentage of monomer conversion is calculated from this spectrum according to Equation 7.

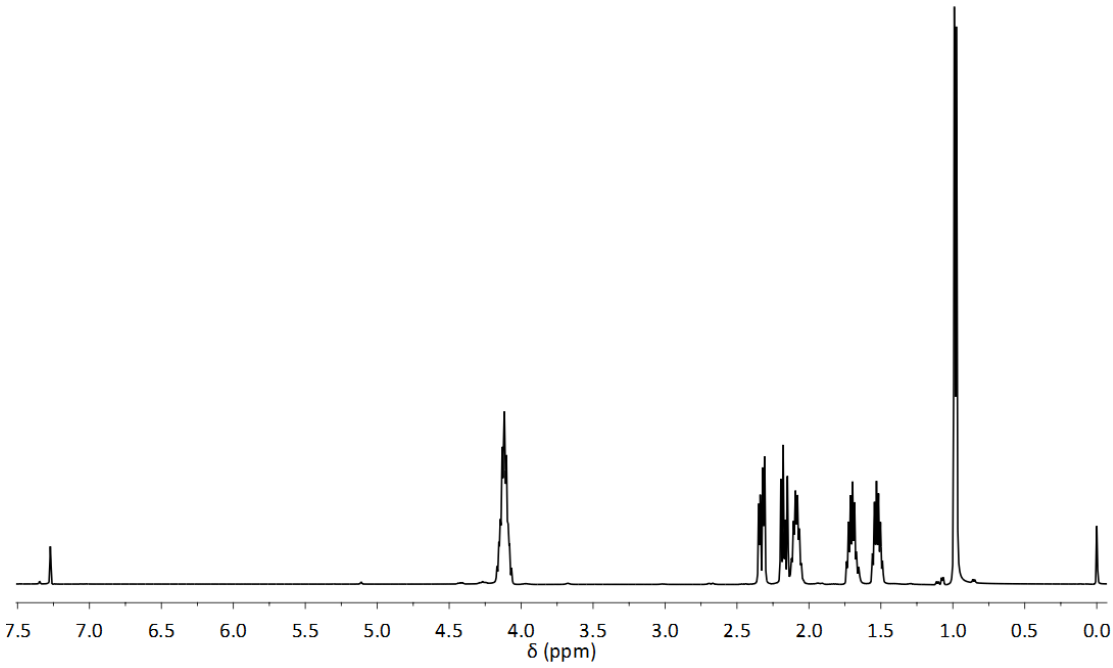

Figure 25. ^{1}H NMR spectrum of PβMδVL after purification. ^{1}H NMR shifts for PβMδVL (500 MHz, $CDCl_3$, 25 °C): δ 4.12 (−O-C**H₂**-CH_2−); 2.31 (−CO-C**H₂**-CH(CH_3)−); 2.18 (−CO-C**H₂**-CH(CH_3)−); 2.08 (−CH_2-C**H**(CH_3)-CH_2−); 1.70 (−CH(CH_3)−C**H₂**−CH_2−); 1.53 (−CH(CH_3)-C**H₂**-CH_2−); 0.98 (−CH_2-CH(C**H₃**)-CH_2−).

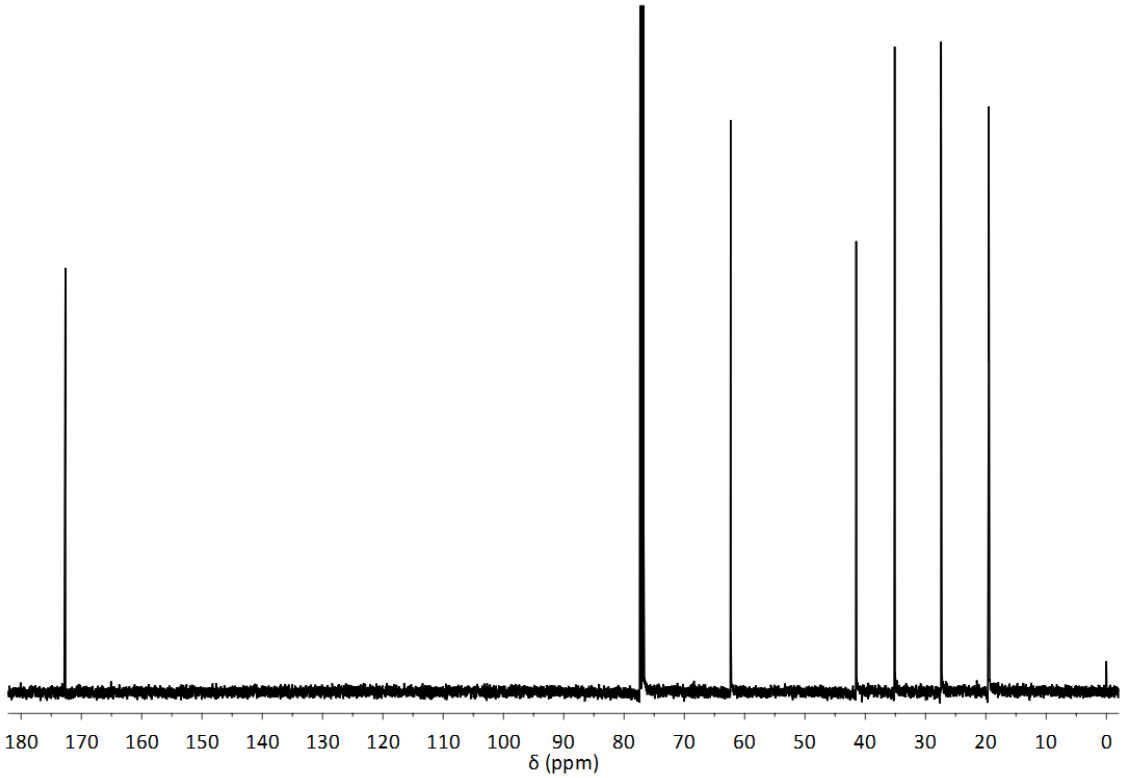

Figure 26. ^{13}C NMR spectrum of PβMδVL after purification. ^{13}C NMR shifts for PβMδVL (126 MHz, CDCl3, 25 °C): δ 172.63 (-CH_2-**C**O-O-); 62.30 (-CH_2-**C**H_2-O-); 41.50 (-CH(CH_3)-**C**H_2-CO-); 35.11 (-CH_2-**C**H_2-CH(CH_3)-); 27.42 (-CH_2-**C**H(CH_3)-CH_2-); 19.51 (-CH_2-CH(**C**H_3)-CH_2-).

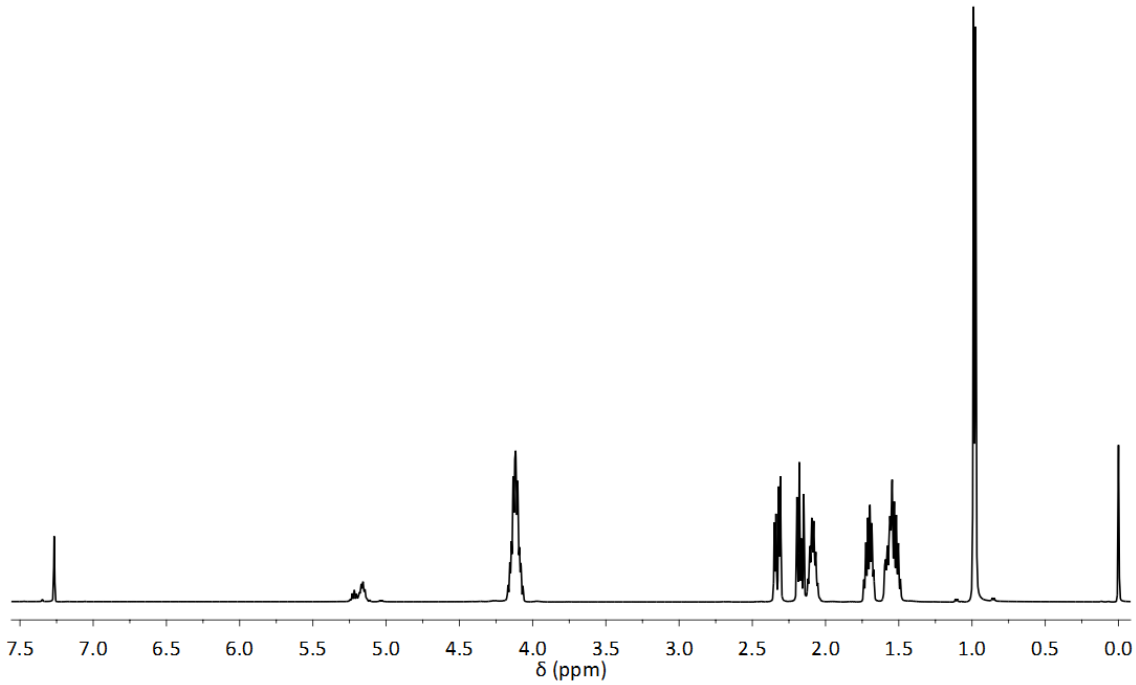

Figure 27. ^{1}H NMR spectrum of PLA-PβMδVL-PLA. ^{1}H NMR shifts for PLA-PβMδVL-PLA (500 MHz, CDCl3, 25 °C): δ 5.16 (−O−C**H**(CH_3)−CO−); 4.12 (−O-C**H_2**-CH_2−); 2.31 (−CO-C**H_2**-CH(CH_3)−); 2.18 (−CO-C**H_2**-CH(CH_3)−); 2.08 (−CH_2-C**H**(CH_3)-CH_2−); 1.70 (−CH(CH_3)−C**H_2**−CH_2−); 1.58 (−O−CH(C**H_3**)−CO−); 1.53 (−CH(CH_3)-C**H_2**-CH_2−); 0.98 (−CH_2-CH(C**H_3**)-CH_2−).

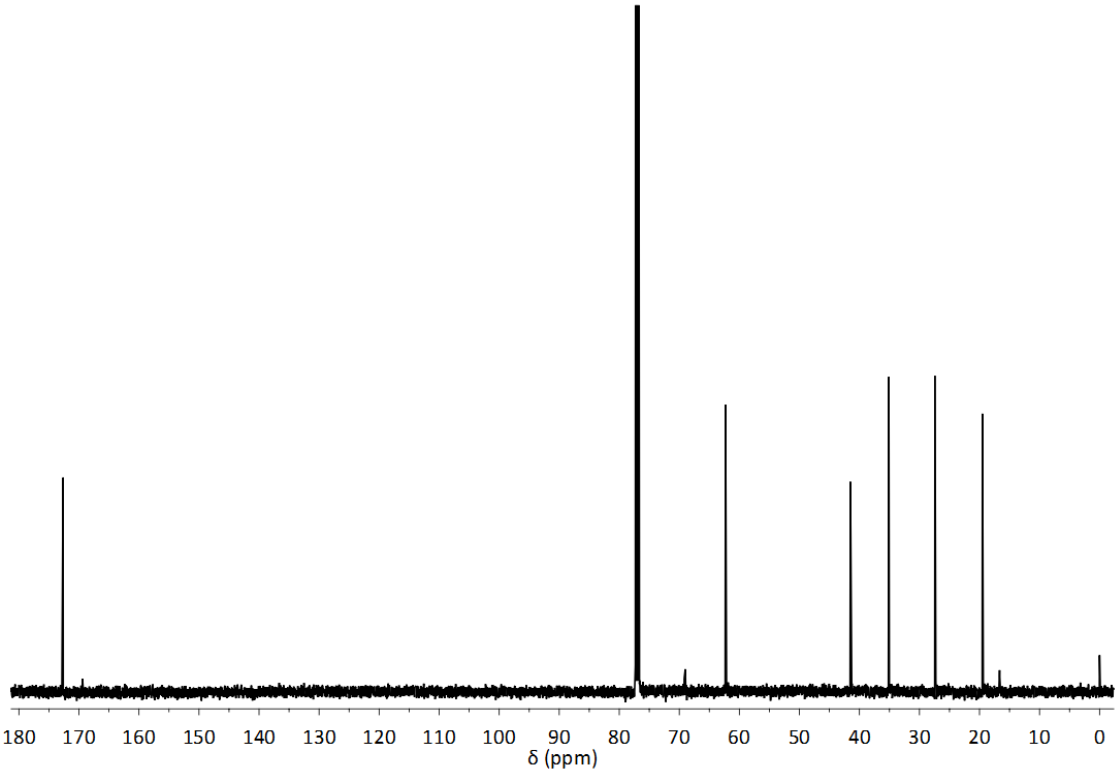

Figure 28. ^{13}C NMR spectrum of PLA-PβMδVL-PLA. ^{13}C NMR shifts for PLA-PβMδVL-PLA (126 MHz, CDCl3, 25 °C): δ 172.63 (-CH_2-**C**O-O-); 169.40 (-**C**O-CH(CH_3)-); 69.00 (-CO-**C**H(CH_3)-O); 62.30 (-CH_2-**C**H_2-O-); 41.50 (-CH(CH_3)-**C**H_2-CO-); 35.11 (-CH_2-**C**H_2-CH(CH_3)-); 27.42 (-CH_2-**C**H(CH_3)-CH_2-); 19.51 (-CH_2-CH(**C**H_3)-CH_2-); 16.65 (-CO-CH(**C**H_3)-O-).

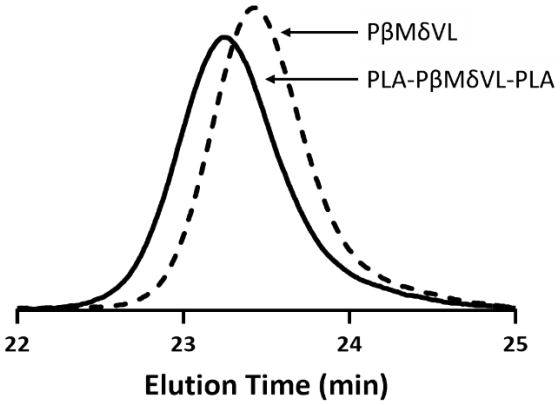

Figure 29. Size exclusion chromatogram overlay for PβMδVL and PLA-PβMδVL-PLA. The shift to a shorter elution time confirms addition of PLA endblocks to the PβMδVL midblock.

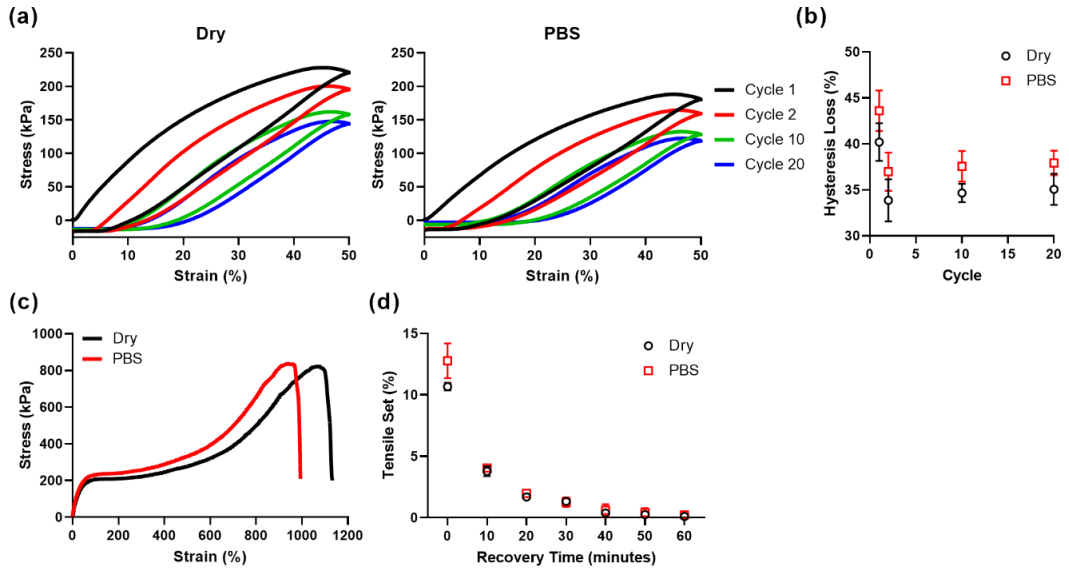

Figure 30. Mechanical properties of PLA-PβMδVL-PLA in dry and PBS conditions. (a) Representative stress-strain curves for tensile hysteresis tests. (b) Hysteresis loss calculated from tensile hysteresis tests. (c) Representative stress-strain curves for uniaxial tests.

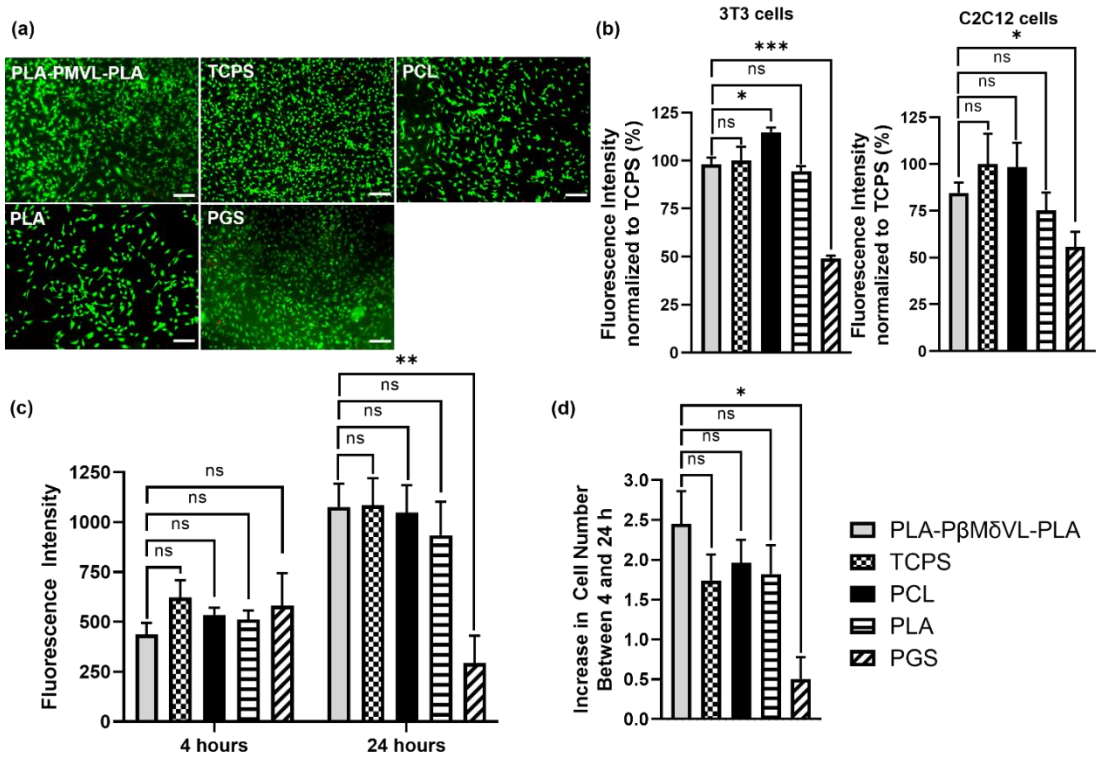

Figure 31. Evaluation of cytocompatibility of the PLA-PβMδVL-PLA polymer, with tissue culture polystyrene (TCPS), polycaprolactone (PCL), polylactic acid (PLA), and polyglycerol sebacate (PGS) as controls. (a) Live/dead assay for 3T3 cells cultured for 24 hours. Substrates were soaked in cell culture medium overnight prior to cell seeding. Scale bar is 200 µm (b) Alamar Blue assay for 3T3 cells and C2C12 cells cultured for 24 hours. Substrates were soaked in cell culture medium overnight prior to cell seeding. (c) Alamar Blue assay for 3T3 cells cultured on Matrigel-coated substrates for 4 and 24 hours. Non-adherent cells in all the samples were removed at 4 hours by a medium change. (d) Increase in cell number between 4 and 24 hours calculated from the data in (c). Error bars represent standard deviation, ns=not significant, ***p-value<0.001, **p-value<0.01, *p-value<0.05, Welch's one-way ANOVA followed by Dunnett's multiple comparison post hoc test, n=3.

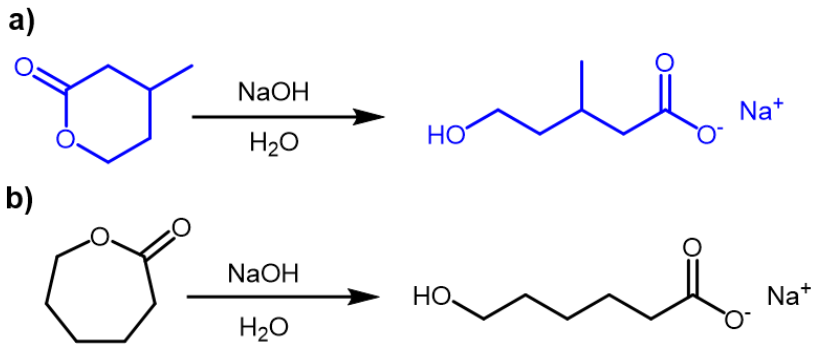

Figure 32. Synthesis of sodium 5-hydroxy-3-methylpentanoate (a) and sodium 6-hydroxycaproate (b).

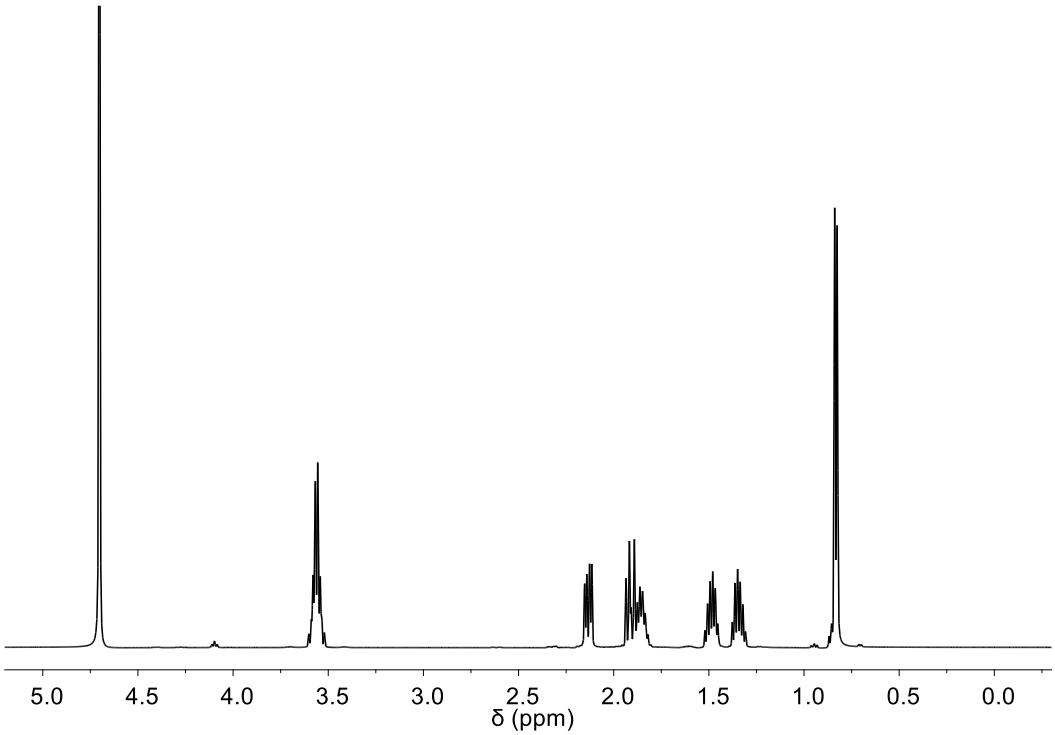

Figure 33. ^{1}H NMR of sodium 5-hydroxy-3-methylpentanoate synthesized from β-methyl-δ-valerolactone. ^{1}H NMR shifts for sodium 5-hydroxy-3-methylpentanoate (500 MHz, D2O, 25 °C): δ (500 MHz, D_2O, 25 °C): δ 3.56 (-OH-C**H$_2$**-CH_2); 2.12 (-$CH(CH_3)$-C**H$_2$**-CO-); 1.86-1.90 (-$CH(CH_3)$-C**H$_2$**-CO-) and (-CH_2-C**H**(CH_3)-CH_2-); 1.48 (-CH_2-C**H$_2$**-$CH(CH_3)$-); 1.35 (-CH_2-C**H$_2$**-$CH(CH_3)$-); 0.83 (-CH_2-CH(C**H$_3$**)-CH_2-).

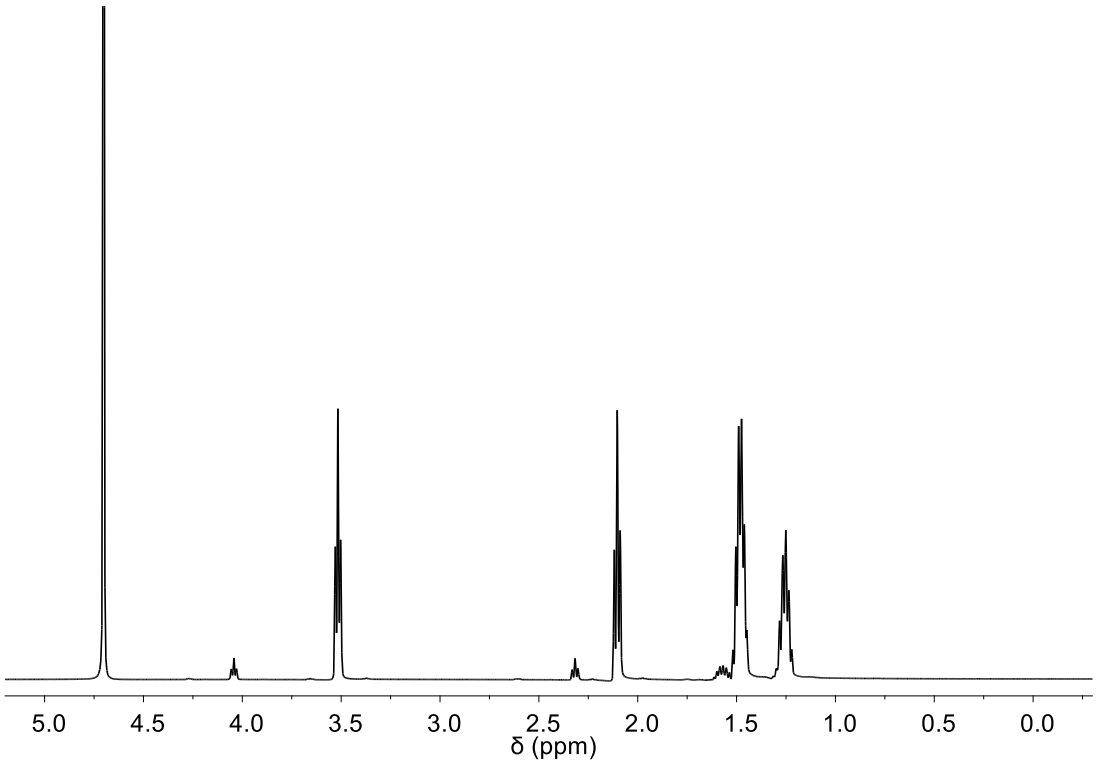

Figure 34. ^{1}H NMR of sodium 6-hydroxycaproate synthesized from ε-caprolactone. ^{1}H NMR shifts for sodium 6-hydroxycaproate (500 MHz, D2O, 25 °C): δ 3.51 (-HO-C**H$_2$**-CH$_2$-); 2.10 (-CH$_2$-C**H$_2$**-CO-); 1.49 (-OH-CH$_2$-C**H$_2$**-CH$_2$-); 1.47 (-CH$_2$-**CH$_2$**-CH$_2$-CO-); 1.25 (-CH$_2$-C**H$_2$**-CH$_2$).

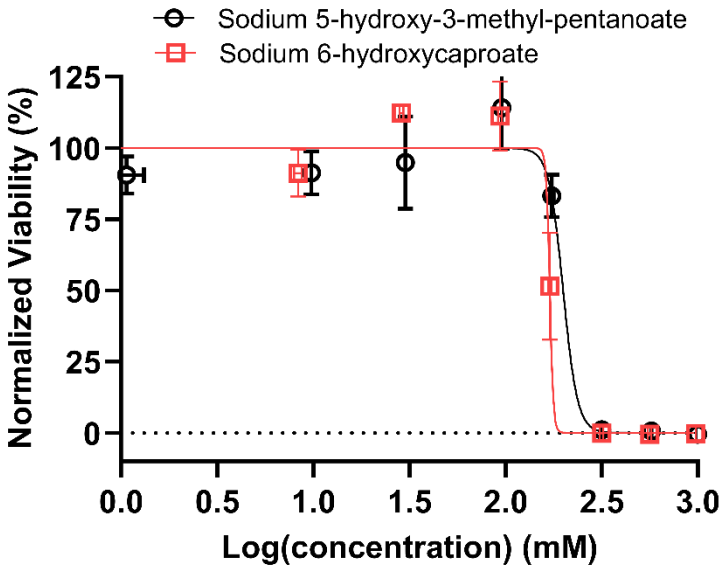

Figure 35. Dose response curve of cell viability when exposed to the degradation products of PβMδVL (sodium 5-hydroxy-3-methyl-pentanoate, black circles) and PCL (sodium 6-hydroxycaproate, red squares). Cell viability was normalized to a non-treated control. Nonlinear regression analysis was performed using GraphPad Prism 9.0 (presented as curves) and used to calculate TD_{50}. Error bars represent standard deviation. n = 3.

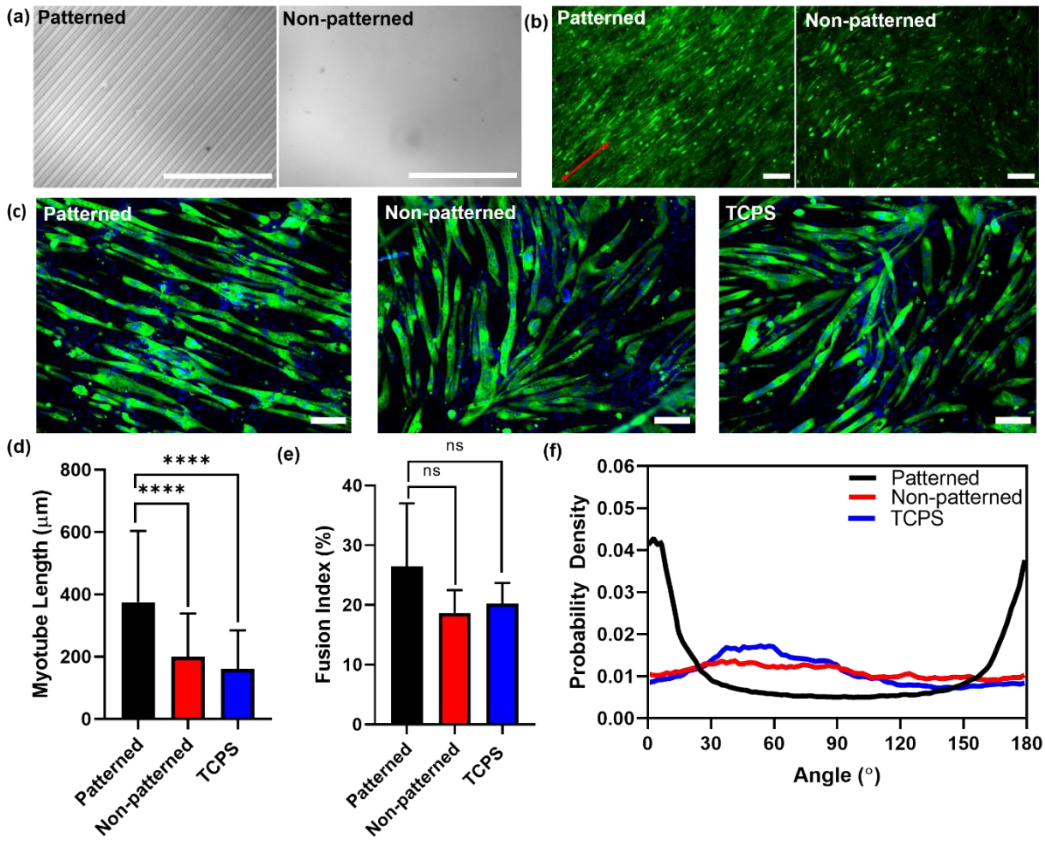

Figure 36. Micropatterned PLA-PβMδVL-PLA substrates support C2C12 cell alignment. (a) Bright-field images of patterned and non-patterned PLA-PβMδVL-PLA processed by thermocompression. (b) Live/dead assay for cells cultured on patterned and non-patterned PLA-PβMδVL-PLA (cells were cultured in differentiation medium for 5 days). Groove direction is indicated by the red arrow. (c) Immunofluorescent staining of total myosin heavy chain (green). Nuclei were counterstained with Hoechst 33342 nuclear stain (blue). (d) Myotube length. Error bars represent standard deviation. ****p-value<0.0001, Welch's one-way ANOVA followed by Games-Howell's multiple comparison post hoc test, n>299. (e) Fusion index. Error bars represent standard deviation. ns=not significant (p-value>0.05), Welch's one-way ANOVA followed by Dunnett's multiple comparison post hoc test, n=6. (f) Alignment angle. Scale bar in all images is 200 μm. Cells in (c), (d), and (e) were cultured in differentiation medium for 7 days.

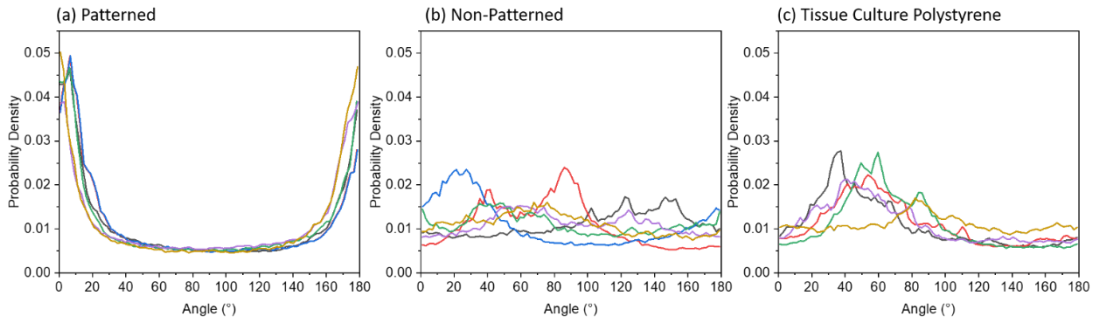

Figure 37. Probability density histograms for C2C12 myotube orientations on patterned PLA-PβMδVL-PLA (a), non-patterned PLA-PβMδVL-PLA (b), and tissue culture polystyrene (c).

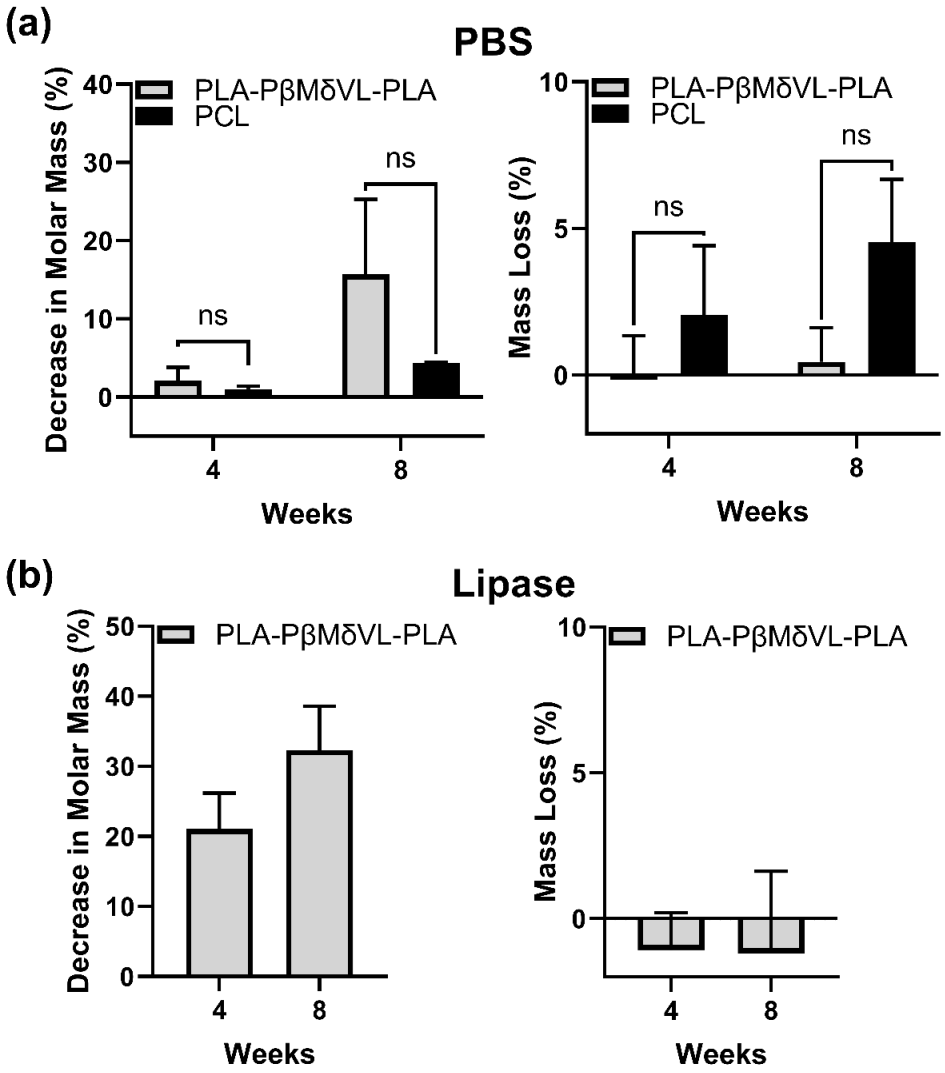

Figure 38. Degradation of PLA-PβMδVL-PLA and PCL in (a) PBS and (b) in lipase solution (*Thermomyces lanuginosus*). PCL was completely degraded at 4 weeks in lipase solution. Error bars represent standard deviation. ns=not significant (p-value is greater than 0.05), two-way ANOVA followed by Tukey's HSD multiple comparison post hoc test for (a), n=3.

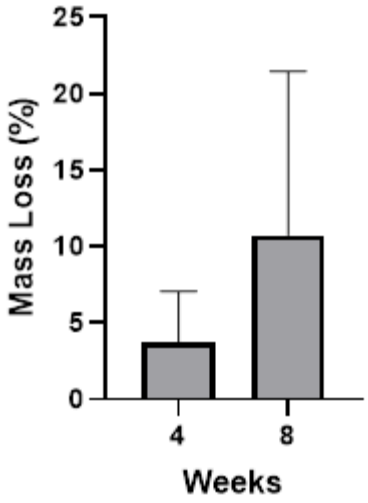

Figure 39. Mass loss of poly(glycerol sebacate) (PGS) in PBS at 4 and 8 weeks. PGS degraded completely at 4 weeks in a solution of *Thermomyces lanuginosus* lipase. PGS is a thermoset and thus was not evaluated for changes in molar mass.

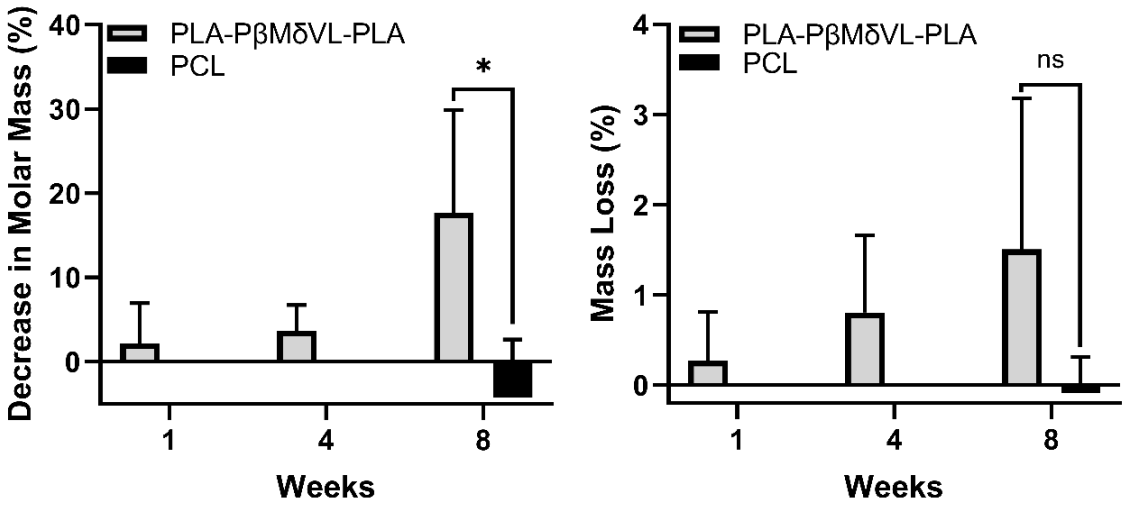

Figure 40. Degradation of PLA-PβMδVL-PLA implanted in the gluteal muscle of rats for 1, 4, and 8 weeks. PCL implanted for 8 weeks was evaluated as a control. Error bars represent standard deviation. ns=not significant, *p-value<0.05, Unpaired Welch's t-test, n=4.

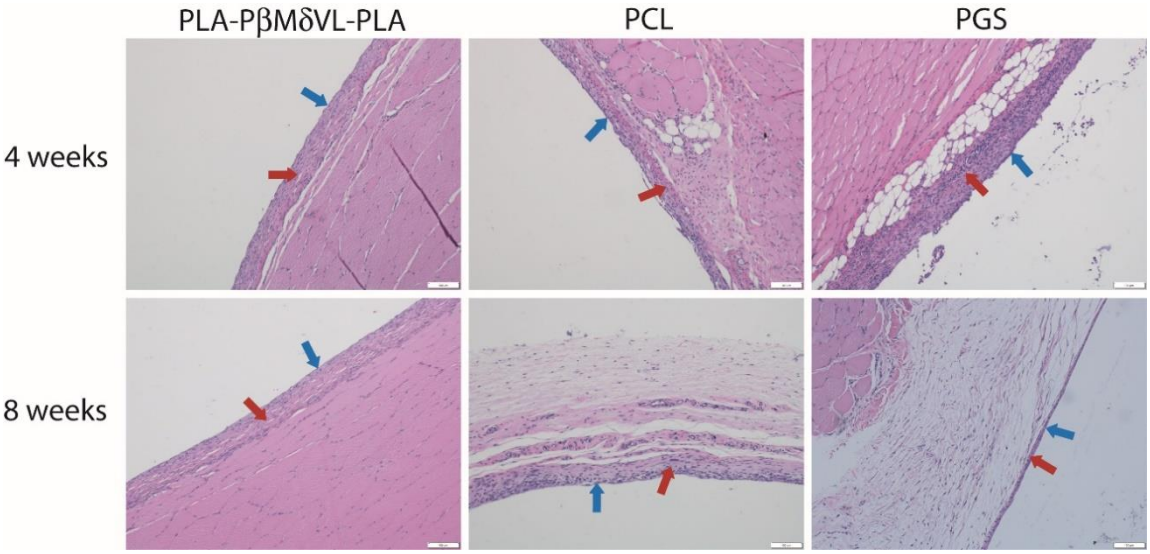

Figure 41. H&E stained images of PLA-PβMδVL-PLA, PCL, and PGS implanted under the fascia of the gluteal muscle. Scale bars: 100 μm. Blue arrows indicate implant-tissue interfaces; red arrows indicate capsules consisting of fibrovascular connective tissue.

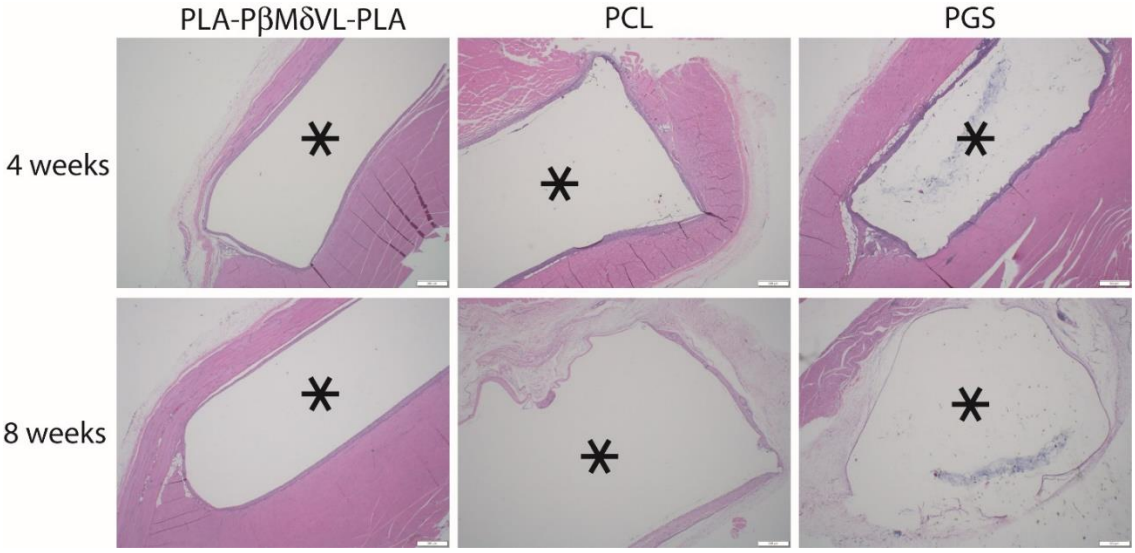

Figure 42. H&E stained images of PLA-PβMδVL-PLA, PCL, and PGS implanted under the fascia of the gluteal muscle. Scale bars: 500 μm. Asterisks indicate locations of polymer implants.

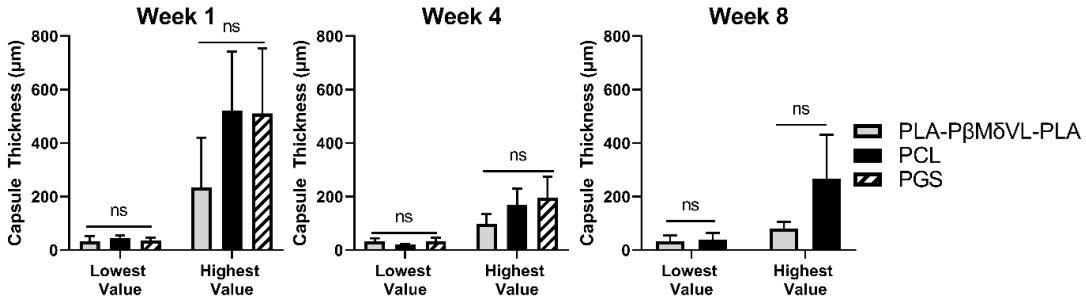

Figure 43. The range of capsule thicknesses for PLA-PβMδVL-PLA, PCL and PGS implanted in the gluteal muscle of rats. PGS samples were not measured at 8 weeks because the capsule area was not present in some samples due to rapid degradation of the material. Error bars represent standard deviation. ns=not significant (p-value is greater than 0.05), two-way ANOVA followed by Tukey's HSD multiple comparison post hoc test, n=3.

Table 6. Semi-quantitative scoring of pathologic findings.

Scoring: 0 = no response, 1 = minimal; 2 = mild; 3 = moderate; and 4 = marked.

Abbreviations: FVCT = fibrovascular connective tissue; FVT = fibrovascular tissue; MNGC = multinucleated giant cell.

A dash signifies that the sample could not be assessed due to the absence of identifiable evidence of the material being present.

		1 weeks												4 weeks										8 weeks									
		Sham			PLA-PβMδVL-PLA			PCL			PGS			Sham			PLA-PβMδVL-PLA			PCL			PGS											
Inflammation	Lymphoid Inflammation	0	0	0	0	0	0	1	1	0	1	0	0	1	0	0	0	1	0	0	1	2	3	3	0	0	0	0	1	2	1	1	3	-	2
	Granulocytic Inflammation	1	1	2	0	2	1	1	2	1	2	2	1	1	1	1	1	1	1	1	1	1	1	1	0	0	2	1	1	1	1	1	1	-	1
	Signs of infection	0	0	0	0	0	0	0	0	0	0	0	0	0	0	0	0	0	0	0	0	0	0	0	0	0	0	0	0	0	0	0	0	-	0
Muscle Damage	Loss of muscle/replacement with adipose tissue	0	0	0	0	0	0	0	0	1	0	0	1	2	1	1	1	1	2	2	2	1	1	2	1	0	1	1	0	0	1	2	1	1	0
	Myocyte Necrosis	1	1	2	1	2	1	2	2	2	2	2	2	2	0	1	2	2	1	1	0	2	1	1	1	2	1	2	1	2	1	2	2	2	2
	Myocyte Regeneration	2	2	0	2	1	0	1	3	2	1	1	2	0	0	0	1	2	0	0	2	0	0	1	2	2	2	2	2	1	1	2	2	2	2
	Interstitial Inflammation	1	0	2	1	2	1	4	3	3	3	3	2	1	1	2	1	1	1	1	0	3	3	2	1	2	0	1	1	2	1	2	2	1	2
Granulation Tissue	Dense FVCT	1	1	1	1	1	1	1	1	1	1	0	1	2	1	1	2	1	1	2	1	1	1	1	1	1	1	1	1	1	2	1	0	-	0
	Loose FVCT	0	1	2	2	2	2	2	2	3	2	2	2	1	1	2	1	1	2	1	2	2	3	1	0	0	1	1	1	1	1	1	1	-	1
	Edematous FVT	0	0	2	1	2	0	3	3	2	3	3	2	0	0	0	0	0	0	0	0	1	0	1	2	1	0	1	1	3	1	2	1	-	3
	Capsule Thickness	0	0	1	1	2	1	2	2	2	2	2	2	0	0	1	1	1	1	2	2	2	3	2	0	0	1	1	1	1	2	1	3	-	1
Foreign Body Response	Histiocytic Inflammation	0	1	2	2	3	1	4	3	3	3	3	2	1	1	1	2	1	2	1	2	3	2	3	0	0	2	1	1	2	1	2	3	-	2
	MNGC	0	1	1	0	1	0	1	1	2	1	1	2	1	0	2	1	1	2	1	2	1	1	0	0	0	3	1	1	2	0	2	1	-	0

Chapter 6: Conclusions

Biomaterials are indispensable to the medical field today and have been used in applications including biosensors, medical implants, and drug delivery devices. Overall, this thesis focused on the development and applications of two different types of biomaterials: gold nanoparticles (GNPs) and elastomeric polymers.

In Chapter 2, we demonstrated that when a pair of heterodimerizing coiled-coils was conjugated to the surface of GNPs, simply flipping the orientation of one of the coiled-coils led to two completely different particle properties: one driving the nanoparticles into large aggregates and the other keeping them colloidally stable. Future studies may include investigating the aggregation kinetics of self-assembling GNPs as a function of nanoparticle or solubilized coiled-coil concentration. Also, the coiled-coils presented here can be easily modified with bioactive ligands or targeting moieties via protein engineering, making these GNPs highly useful for many biomedical applications. For example, the colloidally stable GNPs could be further developed as detection technologies.[30–32,35,43] On the other hand, the self-assembling GNPs could be explored for use as a nanomaterial-based platform to cluster ligand receptors on cells. Clustering of cell ligands can be used to control cell behavior or function, and the self-assembling GNPs could be used to study this in cellular processes, including stem cell differentiation, cancer development, pathogen infection, and T-cell activation.[231]

In Chapter 3, protein-conjugated GNPs that exhibit both multivalency and self-assembly were designed as entry inhibitors of HIV-1. In this work, a coiled-coil "A" protein was fused to an HIV-1 gp120 targeting ligand (known as cysAlgp120). GNPs were

conjugated with heterodimerizing coiled-coil proteins, previously demonstrated to exhibit self-assembly, displaying an HIV-1 gp120 targeting ligand. The protein-conjugated GNPs were used to test inhibition of HIV-1 infection; however, the GNPs showed negligible inhibition. Future work may include exploring different peptide targeting ligands for HIV-1 (see section 3.4 for examples). Lastly, HIV-1 has few copies of the gp120 protein on its surface,[133,134] which may present challenges in developing self-assembling viral entry inhibitors to this virus. Therefore, future work may include exploring different viruses, such as influenza or SARS-CoV-2,[134,135,232] for which this platform may be more suitable.

In Chapter 4, a GNP immunolabelling strategy was used to elucidate the structure of HIV-1 and HTLV-1 Env, which are critical proteins for viral entry and are targets for vaccine development. In this work, we first demonstrated that V4-VLPs could be robustly labeled using the gold nanoparticle immunolabeling strategy, and the quantity of Env on V4-VLPs determined through this strategy was consistent with previous reports. These results suggested that the immunolabeling strategy was suitable for use with HIV-1 and HTLV-1. However, our experiments revealed that HIV-1 and HTLV-1 VLPs had no specific immunolabeling events, possibly due to the low quantity of Env. These findings indicate that GNP immunolabeling has potential for characterizing viruses or other biological systems that have relatively high levels of proteins on the surface. For example, SARS-CoV-2 and influenza virus are estimated to have ~50-100 spike proteins and ~400 hemagglutinin proteins, respectively.[134,135,232] Conversely, HIV-1 has ~7-14 Env proteins on its surface.[133,134] Future work may include adapting the GNP immunolabeling strategy developed here to complete structural evaluations of these viruses. Additionally, the GNP

immunolabeling strategy could be used as a facile method to characterize key proteins on emerging viruses.

In Chapter 5, a triblock polymer, PLA-PβMδVL-PLA, was synthesized and found to exhibit elasticity, degradability, biocompatibility, and processability. The elastomer retained elastomeric properties in aqueous environments and had a Young's modulus similar to soft tissues. PLA-PβMδVL-PLA was found to have good *in vitro* cytocompatibility and favorable *in vivo* biocompatibility as an implantable material. In addition, we demonstrated that PLA-PβMδVL-PLA is degradable both *in vitro* and *in vivo* and readily processable due to its thermoplastic nature. Future work may include exploring the effects of triblock copolymer architecture on the material degradation rate and mechanical properties. Additionally, introducing biologically active components or electroactivity within the polymer may render this material suitable for tissue engineering or other applications.[171,233,234] Overall, the elasticity, degradability, biocompatibility, and processability make this polymer valuable for use as an implantable material, and therefore this elastomer could be explored in the future for use in applications such as medical devices, drug delivery devices, and tissue engineering scaffolds.

In conclusion, this thesis demonstrates the development and applications of both GNPs and elastomeric polymers for use as biomaterials. The biomaterials developed have a myriad of potential future uses in a diverse range of biomedical applications, including biosensors, medical devices, viral inhibitors, and as tools for evaluating the function or structure of biological systems. Overall, the GNPs and elastomeric polymers reported here are strong contributions to the field of biomaterials and lay the groundwork for future discoveries in the biomedical field.

Bibliography

1. Biomaterials. *National Institute of Biomedical Imaging and Bioengineering* https://www.nibib.nih.gov/science-education/science-topics/biomaterials#pid-5111 (2017).

2. Tathe, A., Ghodke, M. & Nikalje, A. P. A brief review: Biomaterials and their application. *Int. J. Pharm. Pharm. Sci.* **2**, 19–23 (2010).

3. Ferraro, A. Biomaterials and therapeutic applications. *IOP Conf. Ser. Mater. Sci. Eng.* **108**, (2016).

4. Zong, J., Cobb, S. L. & Cameron, N. R. Peptide-functionalized gold nanoparticles: versatile biomaterials for diagnostic and therapeutic applications. *Biomater. Sci.* **5**, 872–886 (2017).

5. Teo, A. J. T. *et al.* Polymeric Biomaterials for Medical Implants and Devices. *ACS Biomater. Sci. Eng.* **2**, 454–472 (2016).

6. Kohane, D. S. & Langer, R. Polymeric Biomaterials in Tissue Engineering. *Pediatr. Res.* **63**, 487–491 (2008).

7. Amina, S. J. & Guo, B. A Review on the Synthesis and Functionalization of Gold Nanoparticles as a Drug Delivery Vehicle. *Int. J. Nanomedicine* **15**, 9823–9857 (2020).

8. Murthy, S. K. Nanoparticles in modern medicine: State of the art and future challenges. *Int. J. Nanomedicine* **2**, 129–141 (2007).

9. Dykman, L. & Khlebtsov, N. Gold nanoparticles in biomedical applications: recent advances and perspectives. *Chem. Soc. Rev.* **41**, 2256–2282 (2012).

10. Li, H. *et al.* Advances in the application of gold nanoparticles in bone tissue engineering. *J. Biol. Eng.* **14**, 1–15 (2020).

11. Miao, Z. *et al.* Surface-bioengineered gold nanoparticles for biomedical applications. *Curr. Med. Chem.* **25**, 1920–1944 (2018).

12. Arvizo, R., Bhattacharya, R. & Mukherjee, P. Gold nanoparticles: opportunities and challenges in nanomedicine. *Expert Opin Drug Deliv* **7**, 753–763 (2011).

13. Gao, J., Huang, X., Liu, H., Zan, F. & Ren, J. Colloidal stability of gold nanoparticles modified with thiol compounds: Bioconjugation and application in cancer cell imaging. *Langmuir* **28**, 4464–4471 (2012).

14. Ghosh, P., Han, G., De, M., Kim, C. K. & Rotello, V. M. Gold nanoparticles in delivery applications. *Adv. Drug Deliv. Rev.* **60**, 1307–1315 (2008).

15. Yang, Z. *et al.* Self-assembly of semiconducting-plasmonic gold nanoparticles with enhanced optical property for photoacoustic imaging and photothermal therapy. *Theranostics* **7**, 2177–2185 (2017).

16. Schulz, F. *et al.* Ligand Layer Engineering to Control Stability and Interfacial Properties of Nanoparticles. *Langmuir* **32**, 7897–7907 (2016).

17. Popovtzer, R. *et al.* Targeted Gold Nanoparticles Enable Molecular CT Imaging of Cancer. *NanoLetters* **8**, 4593–4596 (2008).

18. Kim, D., Park, S., Lee, J. H., Jeong, Y. Y. & Jon, S. Antibiofouling Polymer-Coated Gold Nanoparticles as a Contrast Agent for in Vivo X-ray Computed Tomography Imaging. *J. Am. Chem. Soc.* **129**, 7661–7665 (2007).

19. Stirling, J. W. Immuno- and Affinity Probes for Electron Microscopy: A Review of Labeling and Preparation Techniques. *J. Histochem. Cytochem.* **38**, 145–157 (1990).

20. Cavalera, S. *et al.* A multi-target lateral flow immunoassay enabling the specific and sensitive detection of total antibodies to SARS COV-2. *Talanta* **223**, 121737 (2021).

21. Pramanik, A. *et al.* The rapid diagnosis and effective inhibition of coronavirus using spike antibody attached gold nanoparticles. *Nanoscale Adv.* **3**, 1588–1596 (2021).

22. Lee, K. *et al.* Nanoparticle delivery of Cas9 ribonucleoprotein and donor DNA in vivo induces homology-directed DNA repair. *Nat. Biomed. Eng.* **1**, 889–901 (2017).

23. Paul, A. M. *et al.* Delivery of antiviral small interfering RNA with gold nanoparticles inhibits dengue virus infection in vitro. *J. Gen. Virol.* **95**, 1712–1722 (2014).

24. Li, C. M. *et al.* DNA-AuNP networks on cell membranes as a protective barrier to inhibit viral attachment, entry and budding. *Biomaterials* **77**, 216–226 (2016).

25. Shiang, Y.-C. *et al.* Highly efficient inhibition of human immunodeficiency virus type 1 reverse transcriptase by aptamers functionalized gold nanoparticles. *Nanoscale* **5**, 2756–2764 (2013).

26. Baganizi, D. R. *et al.* Peptide-Functionalized Gold Nanoparticles are Potent Inhibitors of Respiratory Syncytial Virus (RSV) Infection. *Adv. Mater. TechConnect Briefs* 127–130 (2016).

27. Wei, J. *et al.* Analysis of Influenza Virus Receptor Specificity Using Glycan-Functionalized Gold Nanoparticles. *ACS Nano* **8**, 4600–4607 (2014).

28. Rosi, N. L. & Mirkin, C. A. Nanostructures in biodiagnostics. *Chem. Rev.* **105**, 1547–1562 (2005).

29. Sato, K., Hosokawa, K. & Maeda, M. Colorimetric biosensors based on DNA-nanoparticle conjugates. *Anal. Sci.* **23**, 17–20 (2007).

30. Draz, M. S. & Shafiee, H. Applications of gold nanoparticles in virus detection. *Theranostics* **8**, 1985–2017 (2018).

31. Borghei, Y. S. *et al.* Visual detection of cancer cells by colorimetric aptasensor based on aggregation of gold nanoparticles induced by DNA hybridization. *Anal. Chim. Acta* **904**, 92–97 (2016).

32. Saha, K., Agasti, S. S., Kim, C., Li, X. & Rotello, V. M. Gold nanoparticles in chemical and biological sensing. *Chem. Rev.* **112**, 2739–2779 (2012).

33. Liu, J. & Lu, Y. A colorimetric lead biosensor using DNAzyme-directed assembly of gold nanoparticles. *J. Am. Chem. Soc.* **125**, 6642–6643 (2003).

34. Jazayeri, M. H., Aghaie, T., Avan, A., Vatankhah, A. & Ghaffari, M. R. S. Colorimetric detection based on gold nanoparticles (GNPs): An easy, fast, inexpensive, low-cost and short time method in detection of analytes (protein, DNA, and ion). *Sens. Bio-sensing Res.* **20**, 1–8 (2018).

35. Hamdy, M. E. *et al.* Development of gold nanoparticles biosensor for ultrasensitive diagnosis of foot and mouth disease virus. *J. Nanobiotechnology* **16**, 1–12 (2018).

36. Silva, G. A. Nanotechnology applications and approaches for neuroregeneration and drug delivery to the central nervous system. *Ann. N. Y. Acad. Sci.* **1199**, 221–230 (2010).

37. Liu, X., Atwater, M., Wang, J. & Huo, Q. Extinction coefficient of gold nanoparticles with different sizes and different capping ligands. *Colloids Surfaces B Biointerfaces* **58**, 3–7 (2007).

38. Mirkin, C. A., Letsinger, R. L., Mucic, R. C. & Storhoff, J. J. A DNA-based method for rationally assembling nanoparticles into macroscopic materials. *Lett. to Nat.* **382**, 607–609 (1996).

39. Ryadnov, M. G., Ceyhan, B., Niemeyer, C. M. & Woolfson, D. N. 'Belts and Braces': A peptide-based linker system of de novo design. *J. Am. Chem. Soc.* **125**, 9388–9394 (2003).

40. Boal, A. *et al.* Self-assembly of nanoparticles into structured spherical and network aggregates. *Nature* **404**, 746–8 (2000).

41. Mucic, R. C., Storhoff, J. J., Mirkin, C. A. & Letsinger, R. L. DNA-directed

synthesis of binary nanoparticle network materials. *J. Am. Chem. Soc.* **120**, 12674–12675 (1998).

42. Srivastava, S., Verma, A., Frankamp, B. L. & Rotello, V. M. Controlled assembly of protein-nanoparticle composites through protein surface recognition. *Adv. Mater.* **17**, 617–621 (2005).

43. Ahmed, S. R. *et al.* In situ self-assembly of gold nanoparticles on hydrophilic and hydrophobic substrates for influenza virus-sensing platform. *Sci. Rep.* **7**, 1–11 (2017).

44. Zhang, X., Sun, C. & Fang, N. Manufacturing at nanoscale: Top-down, bottom-up and system engineering. *J. Nanoparticle Res.* **6**, 125–130 (2004).

45. Won, S., Hindmarsh, S. & Gibson, M. I. Triggerable Multivalent Glyconanoparticles for Probing Carbohydrate-Carbohydrate Interactions. *ACS Macro Lett.* **7**, 178–183 (2018).

46. Bhat, S. & Kumar, A. Biomaterials and bioengineering tomorrow's healthcare. *Biomatter* **3**, (2013).

47. Kim, M. S. *et al.* Polymeric Scaffolds for Regenerative Medicine. *Polym. Rev.* **51**, 23–52 (2011).

48. Liang, Y., Li, L., Scott, R. A., Kiick, K. L. & Road, R. Polymeric Biomaterials: Diversse Functions Enabled by Advances in Macromolecular Chemistry. *Macromolecules* **50**, 483–502 (2017).

49. Olatunji, O. *Natural Polymers Industry Techniques and Applications*. (Springer International Publishing, 2016).

50. Song, R. *et al.* Current development of biodegradable polymeric materials for biomedical applications. *Drug Des. Devel. Ther.* **12**, 3117–3145 (2018).

51. Amini, A. R., Wallace, J. S. & Nukavarapu, S. P. Short-Term and Long-Term Effects of Orthopedic Biodegradable Implants. *J. Long Term Eff Med Implant.* **21**, 93–122 (2011).

52. Sheikh, Z. *et al.* Biodegradable Materials for Bone Repair and Tissue Engineering Applications. *Materials (Basel).* **8**, 5744–5794 (2015).

53. Nair, L. S. & Laurencin, C. T. Biodegradable polymers as biomaterials. *Prog. Polym. Sci.* **32**, 762–798 (2007).

54. Woodruff, M. A. & Hutmacher, D. W. The return of a forgotten polymer - Polycaprolactone in the 21st century. *Prog. Polym. Sci.* **35**, 1217–1256 (2010).

55. Carnicer-Lombarte, A. *et al.* Mechanical matching of implant to host minimises

foreign body reaction. *bioRxiv* 1–41 (2019) doi:10.1101/829648.

56. Prasadh, S., Chung, R. & Wong, W. Unraveling the mechanical strength of biomaterials used as a bone scaffold in oral and maxillofacial defects. *Oral Sci. Int.* **15**, 48–55 (2018).

57. Serrano, M. C., Chung, E. J. & Ameer, G. A. Advances and Applications of Biodegradable Elastomers in Regenerative Medicine. *Mater. Views* **20**, 192–208 (2010).

58. Nikitin, M. P., Zdobnova, T. A., Lukash, S. V, Stremovskiy, O. A. & Deyev, S. M. Protein assisted self-assembly of multifunctional nanoparticles. *PNAS* **107**, 5827–5832 (2010).

59. Eidelshtein, G., Fattal, M., Avishai, G. & Kempinski, B. Preparation , Characterization and Manipulation of Conjugates between Gold Nanoparticles and DNA. *nanomaterials* **6**, 1–8 (2016).

60. Liu, X., Huang, H., Jin, Q. & Ji, J. Mixed charged zwitterionic self-assembled monolayers as a facile way to stabilize large gold nanoparticles. *Langmuir* **27**, 5242–5251 (2011).

61. Holmlin, R. E., Chen, X., Chapman, R. G., Takayama, S. & Whitesides, G. M. Zwitterionic SAMs that Resist Nonspecific Adsorption of Protein from Aqueous Buffer. *Langmuir* **17**, 2841–2850 (2001).

62. Pillai, P. P., Huda, S., Kowalczyk, B. & Grzybowski, B. A. Controlled pH stability and adjustable cellular uptake of mixed-charge nanoparticles. *J. Am. Chem. Soc.* **135**, 6392–6395 (2013).

63. Keefe, A. J. & Jiang, S. Poly(zwitterionic)protein conjugates offer increased stability without sacrificing binding affinity or bioactivity. *Nat. Chem.* **4**, 59–63 (2012).

64. Wu, A., Cheng, W., Li, Z., Jiang, J. & Wang, E. Electrostatic-assembly metallized nanoparticles network by DNA template. *Talanta* **68**, 693–699 (2006).

65. Sastry, M., Kumar, A., Datar, S., Dharmadhikari, C. V & Ganesh, K. N. DNA-mediated electrostatic assembly of gold nanoparticles into linear arrays by a simple drop-coating procedure. *Appl. Phys. Lett.* **78**, 2943–2945 (2001).

66. Song, J., Park, S., Kim, S., Im, K. & Park, N. Electrostatic interaction driven gold nanoparticle assembly on three-dimensional triangular pyramid DNA nanostructures. *New J. Chem.* **41**, 9590–9593 (2017).

67. Sanchez-Iglesias, A. *et al.* Hydrophobic Interactions Modulate Self-Assembly of Nanoparticles. *ACS Nano* **6**, 11059–11065 (2012).

68. Ofir, Y., Samanta, B. & Rotello, V. M. Polymer and biopolymer mediated self-assembly of gold nanoparticles. *Chem. Soc. Rev.* **37**, 1909–30 (2008).

69. Mann, B. S., Shenton, W., Li, M. & Connolly, S. Biologically Programmed Nanoparticle Assembly. *Adv. Mater.* **4**, 147–150 (2000).

70. Loweth, C. J., Caldwell, W. B., Peng, X., Alivisatos, A. P. & Schultz, P. G. DNA-Based Assembly of Gold Nanocrystals. *Angew. Chem. Int. Ed.* **38**, 1808–1812 (1999).

71. Stevens, M. M., Flynn, N. T., Wang, C., Tirrell, D. A. & Langer, R. Coiled-Coil Peptide-Based Assembly of. *Adv. Mater.* **16**, 915–918 (2004).

72. Obana, M., Silverman, B. R. & Tirrell, D. A. Protein-Mediated Colloidal Assembly. *J. Am. Chem. Soc.* **139**, 14251–14256 (2017).

73. Schoen, A. P., Hommersom, B., Heilshorn, C. & Leunissen, M. E. Tuning colloidal association with specific peptide interactions. *Soft Matter* **9**, 6781–6785 (2013).

74. Connolly, S. A. & Fitzmaurice, D. J. Programmed assembly of gold nanocrystals in aqueous solution. *Adv. Mater.* **11**, 1202–1205 (1999).

75. Shenton, W., Davis, S. A. & Mann, S. Directed Self-Assembly of Nanoparticles into Macroscopic Materials Using Antibody- Antigen Recognition. *Adv. Mater.* **11**, 449–452 (1999).

76. Shen, W., Zhang, K., Kornfield, J. A. & Tirrell, D. A. Tuning the erosion rate of artificial protein hydrogels through control of network topology. *Nat. Mater.* **5**, 153–158 (2006).

77. Liu, B., Liu, Y., Riesberg, J. J. & Shen, W. Dynamic Presentation of Immobilized Ligands Regulated through Biomolecular Recognition. *J. Am. Chem. Soc.* **132**, 13630–13632 (2010).

78. Wang, X., Riesberg, J. J. & Shen, W. Reversible regulation of bioactive ligands presented on immobilized gold nanoparticles. *Soft Matter* **8**, 2812–2815 (2012).

79. Frens, G. Controlled Nucleation for the Regulation of the Particle Size in Monodisperse Gold Suspensions. *Nat. Phys. Sci.* **241**, 20–22 (1973).

80. Haiss, W., Thanh, N. T. K., Aveyard, J. & Fernig, D. G. Determination of Size and Concentration of Gold Nanoparticles from UV - Vis Spectra. *Anal. Chem.* **79**, 4215–4221 (2007).

81. Doniach, S. & Lipfert, J. Small and wide angle x-ray scattering from biological macromolecules and their complexes in solution. *Compr. Biophys.* **1**, 376–397 (2012).

82. Franke, D. *et al.* ATSAS 2.8: A comprehensive data analysis suite for small-angle scattering from macromolecular solutions. *J. Appl. Crystallogr.* **50**, 1212–1225 (2017).

83. Feigin, L. A. & Svergun, D. I. *Structure Analysis by Small-Angle X-Ray and Neutron Scattering*. (Plenum Press, 1987).

84. Liu, X., Atwater, M., Wang, J. & Huo, Q. Extinction coefficient of gold nanoparticles with different sizes and different capping ligands. **58**, 3–7 (2007).

85. Mucic, R. C., Storhoff, J. J., Mirkin, C. A. & Letsinger, R. L. DNA-directed synthesis of binary nanoparticle network materials [5]. *J. Am. Chem. Soc.* **120**, 12674–12675 (1998).

86. Park, C. *et al.* Cyclodextrin-covered gold nanoparticles for targeted delivery of an anti-cancer drug. *J. Mater. Chem.* **19**, 2310–2315 (2009).

87. Ghosh, S. K. & Pal, T. Interparticle Coupling Effect on the Surface Plasmon Resonance of Gold Nanoparticles : From Theory to Applications. *Chem. Rev.* **107**, 4797–4862 (2007).

88. Kennedy, S. B., Littrell, K., Thiyagarajan, P., Tirrell, D. A. & Russell, T. P. Controlled structure in artificial protein hydrogels. *Macromolecules* **38**, 7470–7475 (2005).

89. Urban, D. A. *et al.* Plasmonic nanoparticles and their characterization in physiological fluids. *Colloids Surfaces B Biointerfaces* **137**, 39–49 (2016).

90. Hinterwirth, H., Kappel, S., Waitz, T., Prohaska, T. & Lindner, W. Quantifying Thiol Ligand Density of Self-Assembled Monolayers on Gold Nanoparticles by Inductively Coupled Plasma-Mass Spectrometry. *ACS Nano* **7**, 1129–1136 (2013).

91. Smith, A. M. *et al.* Quantitative Analysis of Thiolated Ligand Exchange on Gold Nanoparticles Monitored by 1 H NMR Spectroscopy. *Anal. Chem.* **87**, 2771–2778 (2015).

92. Li, S., Peng, Z. & Leblanc, R. M. Method To Determine Protein Concentration in the Protein − Nanoparticle Conjugates Aqueous Solution Using Circular Dichroism Spectroscopy. (2015) doi:10.1021/acs.analchem.5b01451.

93. Mansfield, E., Tyner, K. M., Poling, C. M. & Blacklock, J. L. Determination of nanoparticle surface coatings and nanoparticle purity using microscale thermogravimetric analysis. *Anal. Chem.* **86**, 1478–1484 (2014).

94. Ryu, W.-S. Virus Life Cycle. in *Molecular Virology of Human Pathogenic Viruses* 31–46 (Academic Press, 2020).

95. Haqqani, A. A. & Tilton, J. C. Entry inhibitors and their use in the treatment of

HIV-1 infection. *Antiviral Res.* **98**, 158–170 (2013).

96. Briz, V., Poveda, E. & Soriano, V. HIV entry inhibitors: mechanisms of action and resistance pathways. *J. Antimicrob. Chemother.* **57**, 619–627 (2006).

97. Fasting, C. *et al.* Multivalency as a Chemical Organization and Action Principle. *Angew. Rev.* **51**, 10472–10498 (2012).

98. Krishnamurthy, V. M., Estroff, L. M. & Whitesides, G. M. Multivalency in Ligand Design. in *Fragment Based Approaches in Drug Disovery* (eds. Mannhold, R., Kubinyi, H. & Folkers, G.) 11–53 (Wiley VCH Verlag Gmbh & Co., 2006).

99. Muñoz, A. *et al.* Synthesis of giant globular multivalent glycofullerenes as potent inhibitors in a model of Ebola virus infection. *Nat. Chem.* **8**, 50–57 (2016).

100. Xiao, S. *et al.* Pentacyclic triterpenes grafted on CD cores to interfere with influenza virus entry: A dramatic multivalent effect. *Biomaterials* **78**, 74–85 (2016).

101. Tang, S. *et al.* Antiviral Agents from Multivalent Presentation of Sialyl Oligosaccharides on Brush Polymers. *ACS Macro Lett.* **5**, 413–418 (2016).

102. Park, S. *et al.* Probing Cell-Surface Carbohydrate Binding Proteins with Dual-Modal Glycan-Conjugated Nanoparticles. *J. Am. Chem. Soc.* **137**, 5961–5968 (2015).

103. Vonnemann, J. *et al.* Size Dependence of Steric Shielding and Multivalency Effects for Globular Binding Inhibitors. *J. Am. Chem. Soc.* **137**, 2572–2579 (2015).

104. Spaltenstein, A. & Whitesides, G. M. Polyacrylamides Bearing Pendant α-Sialoside Groups Strongly Inhibit Agglutination of Erythrocytes by Influenza Virus. *J. Am. Chem. Soc.* **113**, 686–687 (1991).

105. Mammen, M., Dahmann, G. & Whitesides, G. M. Effective Inhibitors of Hemagglutination by Influenza Virus Synthesized from Polymers Having Active Ester Groups. Insight into Mechanism of Inhibition. *J. Med. Chem* **38**, 4179–4190 (1995).

106. Reuter, J. D. *et al.* Inhibition of Viral Adhesion and Infection by Sialic-Acid-Conjugated Dendritic Polymers. *Bioconjug. Chem.* **10**, 271–278 (1999).

107. Bianculli, R. H., Mase, J. D. & Schulz, M. D. Antiviral Polymers : Past Approaches and Future Possibilities. *Macromolecules* **53**, 9158–9186 (2020).

108. Papp, I. *et al.* Inhibition of Influenza Virus Activity by Multivalent Glycoarchitectures with Matched Sizes. *ChemBioChem* **12**, 887–895 (2011).

109. Varga, N. *et al.* A multivalent inhibitor of the DC-SIGN dependent uptake of HIV-1 and Dengue virus. *Biomaterials* **35**, 4175–4184 (2014).

110. Papp, I. *et al.* Inhibition of Influenza Virus Infection by Multivalent Sialic-Acid-Functionalized Gold Nanoparticles. *small* **6**, 2900–2906 (2010).

111. Reina, G., Peng, S., Jacquemin, L., Andrade, F. & Bianco, A. Hard Nanomaterials in Time of Viral Pandemics. *ACSNano* **14**, 9364–9388 (2020).

112. Kim, J. *et al.* Porous gold nanoparticles for attenuating infectivity of influenza A virus. *J. Nanobiotechnology* 1–11 (2020) doi:10.1186/s12951-020-00611-8.

113. Sanna, V. *et al.* Inhibition of Human Immunodeficiency Virus-1 Integrase by β-Diketo Acid Coated Gold Nanoparticles. *ACS Med. Chem. Lett.* **11**, 857–861 (2020).

114. Bastian, A. R. *et al.* Mechanism of Multivalent Nanoparticle Encounter with HIV-1 for Potency Enhancement of Peptide Triazole Virus. *J. Biol. Chem.* **290**, 529–543 (2015).

115. Vonnemann, J., Sieben, C., Ludwig, K., Herrmann, A. & Haag, R. Virus inhibition induced by polyvalent nanoparticles of different sizes. *Nanoscale* **6**, 2353–2360 (2014).

116. Siegel, R. A. & Linstad, J. L. Cooperative Binding Isotherms for Nearest Neighbor Interacting Ligands on Platonic Solids : A Simple Model for Viral Capture Nanotherapy. *J. Phys. Chem. B* **114**, 14071–14076 (2010).

117. Wilen, C. B., Tilton, J. C. & Doms, R. W. HIV: Cell Binding and Entry. *Cold Spring Harb. Perspect. Med.* (2012).

118. Liu, B., Liu, Y., Riesberg, J. J. & Shen, W. Dynamic Presentation of Immobilized Ligands Regulated through Biomolecular Recognition. *J. Am. Chem. Soc.* **132**, 13630–13632 (2010).

119. Siehr, A., Xu, B., Siegel, R. A. & Shen, W. Colloidal stability versus self-assembly of nanoparticles controlled by coiled-coil protein interactions. *Soft Matter* **15**, 7122–7126 (2019).

120. Kelley, L. A., Mezulis, S., Yates, C. M., Wass, M. N. & Sternberg, M. J. The Phyre2 web portal for protein modeling, prediciton and analysis. *Nat. Protoc.* **10**, 845–858 (2016).

121. Haiss, W., Thanh, N. T. K., Aveyard, J. & Fernig, D. G. Determination of Size and Concentration of Gold Nanoparticles from UV-Vis Spectra. *Anal. Chem.* **79**, 4215–4221 (2007).

122. Maldonado, J. O. & Mansky, L. M. The HIV-1 Reverse Transcriptase A62V

Mutation Influences Replication Fidelity and Viral Fitness in the Context of Multi-Drug-Resistant Mutations. *Viruses* **10**, (2018).

123. Rawson, J. M. O., Landman, S. R., Reilly, C. S. & Mansky, L. M. HIV-1 and HIV-2 exhibit similar mutation frequencies and spectra in the absence of G-to-A hypermutation. *Retrovirology* **12**, 1–17 (2015).

124. Kim, J. H., Song, H., Austin, J. L. & Cheng, W. Optimized Infectivity of the Cell-Free Single-Cycle Human Immunodeficiency Viruses Type 1 (HIV-1) and Its Restriction by Host Cells. *PLoS One* **8**, e67170 (2013).

125. Ferrer, M. & Harrison, S. C. Peptide Ligands to Human Immunodeficiency Virus Type 1 gp120 Identified from Phage Display Libraries. *J. Virol.* **73**, 5795–5802 (1999).

126. Lopez-Garcia, P. *et al.* Structural Determinants of Coiled Coil Mechanics. *Phys. Chem. Chem. Phys.* 1–15 (2019).

127. Ghosh, P., Han, G., De, M., Kim, C. K. & Rotello, V. M. Gold nanoparticles in delivery applications. *Adv. Drug Deliv. Rev.* **60**, 1307–1315 (2008).

128. Vodicka, M. A. *et al.* Indicator Cell Lines for Detection of Primary Strains of Human and Simian Immunodeficiency Viruses. *Virology* **233**, 193–198 (1997).

129. Tsai, S.-W. *et al.* Internalized Gold Nanoparticles Do Not Affect the Osteogenesis and Apoptosis of MG63 Osteoblast-Like Cells: A Quantitative , In Vitro Study. *PLoS One* **8**, e76545 (2013).

130. Shukla, R. *et al.* Biocompatibility of Gold Nanoparticles and Their Endocytotic Fate Inside the Cellular Compartment: A Microscopic Overview. *Langmuir* **21**, 10644–10654 (2005).

131. Fan, J. H., Hung, W. I., Li, W. T. & Yeh, J. M. Biocompatibility Study of Gold Nanoparticles to Human Cells. *Int. Fed. Med. Biol. Eng. Proc.* **23**, 870–873 (2009).

132. Daraee, H. *et al.* Application of gold nanoparticles in biomedical and drug delivery. *Artif. Cells, Nanomedicine, Biotechnol.* **44**, 410–422 (2016).

133. Zhu, P. *et al.* Distribution and three-dimensional structure of AIDS virus envelope spikes. *Nature* **441**, 847–852 (2006).

134. Checkley, M. A., Luttge, B. G. & Freed, E. O. HIV-1 envelope glycoprotein biosynthesis, trafficking, and incorporation. *J. Mol. Biol.* **410**, 582–608 (2011).

135. Schiller, J. & Chackerian, B. Why HIV Virions Have Low Numbers of Envelope Spikes: Implications for Vaccine Development. *PLoS Pathog.* **10**, e1004254 (2014).

136. Stano, A. *et al.* Dense Array of Spikes on HIV-1 Virion Particles. *J. Virol.* **91**, 1–19 (2017).

137. Wang, C. *et al.* Artificial peptides conjugated with cholesterol and pocket-specific small molecules potently inhibit infection by laboratory-adapted and primary HIV-1 isolates and enfuvirtide-resistant HIV-1 strains. *J. Antimicrob. Chemother.* **69**, 1537–1545 (2014).

138. Kazmierski, W. M., Kenakin, K. M. & Gudmundsson, K. S. Peptide, Peptidomimetic and Small-molecule Drug Discovery Targeting HIV-1 Host-cell Attachment and Entry through gp120, gp41, CCR5 and CXCR4. *Chem. Biol. Drug Des.* **67**, 13–26 (2006).

139. Cheng, K., El-boubbou, K. & Landry, C. C. Binding of HIV-1 gp120 Glycoprotein to Silica Nanoparticles Modified with CD4 Glycoprotein and CD4 Peptide Fragments. *ACS Appl. Mater. Interfaces* **4**, 235–243 (2012).

140. Kagiampakis, I. *et al.* Potent Strategy To Inhibit HIV-1 by Binding both gp120 and gp41. *Antimicrob. Agents Chemother.* **55**, 264–275 (2011).

141. Dervillez, X. *et al.* Peptide Ligands Selected with CD4-Induced Epitopes on Native Dualtropic HIV-1 Envelope Proteins Mimic Extracellular Coreceptor Domains and Bind to HIV-1 gp120 Independently of Coreceptor Usage. *J. Virol.* **84**, 10131–10138 (2010).

142. Hedestam, G. B. K. *et al.* The challenges of eliciting neutralizing antibodies to HIV-1 and to influenza virus. *Nat. Rev. Microbiol.* **6**, 143–155 (2008).

143. UNAIDS Global HIV statistics. *Fact Sheet- World AIDS Day 2020* aidsinfo.unaids.org (2020).

144. UNAIDS. Global HIV and AIDS statistics — 2018 fact sheet. 1–6 (2018).

145. Why do we need a vaccine to prevent HIV? *HIV Vaccines* HIV.gov (2021).

146. Wyatt, R. The HIV-1 Envelope Glycoproteins: Fusogens, Antigens, and Immunogens. *Science (80-.).* **280**, 1884–1888 (2002).

147. Sattentau, Q. Envelope Glycoprotein Trimers as HIV-1 Vaccine Immunogens. *Vaccines* **1**, 497–512 (2013).

148. Arrildt, K. T., Joseph, S. B. & Swanstrom, R. The HIV-1 Env protein: A coat of many colors. *Curr. HIV/AIDS Rep.* **9**, 52–63 (2012).

149. Merk, A. & Subramaniam, S. HIV-1 envelope glycoprotein structure. *Curr. Opin. Struct. Biol.* **23**, 268–276 (2013).

150. Kwong, P. D. *et al.* Structure of an HIV gp120 envelope glycoprotein in complex

with CD4 receptor and a neutralizing human antibody. *Nature* **393**, 648–659 (1998).

151. Liu, J., Bartesaghi, A., Borgnia, M. J., Sapiro, G. & Subramaniam, S. Molecular architecture of native HIV-1 gp120 trimers. *Nature* **455**, 109–113 (2008).

152. Weissenhorn, W., Dessen, A., Harrison, S. C., Skehel, J. J. & Wiley, D. C. Atomic structure of the ectodomain from HIV-1 gp41. *Nature* **387**, 426–430 (1997).

153. Tran, E. E. H. *et al.* Structural mechanism of trimeric HIV-1 envelope glycoprotein activation. *PLoS Pathog.* **8**, 37 (2012).

154. Buttler, C. A. *et al.* Single molecule fate of HIV-1 envelope reveals late-stage viral lattice incorporation. *Nat. Commun.* **9**, (2018).

155. Murakami, T. Retroviral Env Glycoprotein Trafficking and Incorporation into Virions. *Mol. Biol. Int.* 1–11 (2012) doi:10.1155/2012/682850.

156. Pinon, J. D. *et al.* Human T-Cell Leukemia Virus Type 1 Envelope Glycoprotein gp46 Interacts with Cell Surface Heparan Sulfate Proteoglycans. *J. Virol.* **77**, 9922–9930 (2003).

157. Amar, L. *et al.* Prevalence of human T cell lymphotropic virus 1 infection in Canada. *Curr. Oncol.* **26**, (2019).

158. Iwami, S., Takeuchi, J. S., Nakaoka, S. & Mammano, F. Cell-to-cell infection by HIV contributes over half of virus infection. *Elife* **4**, 1–16 (2015).

159. Hoshino, H. Cellular factors involved in HTLV-1 entry and pathogenicity. *Front. Microbiol.* **3**, 1–12 (2012).

160. Kobe, B., Center, R. J., Kemp, B. E. & Poumbourios, P. Crystal structure of human T cell leukemia virus type 1 gp21 ectodomain crystallized as a maltose-binding protein chimera reveals structural evolution of retroviral transmembrane proteins. *Proc. Natl. Acad. Sci.* **96**, 4319–4324 (1999).

161. Kuo, C.-W. S., Mirsaliotis, A. & Brighty, D. W. Antibodies to the Envelope Glycoprotein of Human T Cell Leukemia Virus Type 1 Robustly Activate Cell-Mediated Cytotoxic Responses and Directly Neutralize Viral Infectivity at Multiple Steps of the Entry Process. *J. Immunol.* **187**, 361–367 (2011).

162. Martin, J. L., Cao, S., Maldonado, J. O., Zhang, W. & Mansky, L. M. Distinct Particle Morphologies Revealed through Comparative Parallel Analyses of Retrovirus-Like Particles. *J. Virol.* **90**, 8074–8084 (2016).

163. Gulati, N. M., Torian, U., Gallagher, J. R. & Harris, A. K. Immunoelectron Microscopy of Viral Antigens. *Curr. Protoc. Microbiol.* **53**, 1–18 (2019).

164. Piludu, M., Medda, L., Monduzzi, M. & Salis, A. Gold nanoparticles: A powerful tool to visualize proteins on ordered mesoporous silica and for the realization of theranostic nanobioconjugates. *Int. J. Mol. Sci.* **19**, 7–9 (2018).

165. Scarff, C. A., Fuller, M. J. G., Thompson, R. F. & Iadanza, M. G. Variations on Negative Stain Electron Microscopy Methods: Tools for Tackling Challenging Systems. *J. Vis. Exp.* **132**, 1–8 (2018).

166. Thompson, R. F., Walker, M., Siebert, C. A., Muench, S. P. & Ranson, N. A. An introduction to sample preparation and imaging by cryo-electron microscopy for structural biology. *Methods* **100**, 3–15 (2016).

167. Zhu, P. *et al.* Electron tomography analysis of envelope glycoprotein trimers on HIV and simian immunodeficiency virus virions. *Proc. Natl. Acad. Sci.* **100**, 15812–15817 (2003).

168. Martin, J. L. *et al.* Disparate Contributions of Human Retrovirus Capsid Subdomains to Gag-Gag Oligomerization, Virus Morphology, and Particle Biogenesis. *J. Virol.* **91**, 1–21 (2017).

169. Chojnacki, J. *et al.* Envelope glycoprotein mobility on HIV-1 particles depends on the virus maturation state. *Nat. Commun.* **8**, (2017).

170. Chojnacki, J., Staudt, T., Glass, B., Bingen, P. & Engelhardt, J. Maturation-Dependent HIV-1 Surface Protein Redistribution Revealed by Fluorescence Nanoscopy. *Science (80-.).* **338**, 524–529 (2012).

171. Chen, Q., Liang, S. & Thouas, G. A. Elastomeric biomaterials for tissue engineering. *Prog. Polym. Sci.* **38**, 584–671 (2013).

172. Ye, H., Zhang, K., Kai, D., Li, Z. & Loh, X. J. Polyester elastomers for soft tissue engineering. *Chem. Soc. Rev.* **47**, 4545–4580 (2018).

173. Yoda, R. Elastomers for biomedical applications. *J. Biomater. Sci. Polym. Ed.* **9**, 561–626 (1998).

174. Amsden, B. Curable, biodegradable elastomers: Emerging biomaterials for drug delivery and tissue engineering. *Soft Matter* **3**, 1335–1348 (2007).

175. Athanasiou, K. A., Niederauer, G. G. & Agrawal, C. M. Sterilization, toxicity, biocompatibility and clinical applications of polylactic acid/polyglycolic acid copolymers. *Biomaterials* **17**, 93–102 (1996).

176. Oh, J. K. Polylactide (PLA)-based amphiphilic block copolymers: synthesis, self-assembly, and biomedical applications. *Soft Matter* **7**, 5096–5108 (2011).

177. Stewart, S. A., Dominguez-Robles, J., Donnelly, R. F. & Larrañeta, E. Implantable Polymeric Drug Delivery Devices: Clinical Applications. *Polymers (Basel).* **10**,

(2018).

178. Kang, Y., Yang, J., Khan, S., Anissian, L. & Ameer, G. A. A new biodegradable polyester elastomer for cartilage. *J. Biomed. Mater. Res. Part A* **77**, 331–339 (2006).

179. Chen, Q., Zhu, C. & Thouas, G. A. Progress and challenges in biomaterials used for bone tissue engineering: bioactive glasses and elastomeric composites. *Prog. Biomater.* **1**, 1–22 (2012).

180. Engelberg, I. & Kohn, J. Physico-mechanical properties of degradable polymers used in medical applications: A comparative study. *Biomaterials* **12**, 292–304 (1991).

181. Liu, H. & Webster, T. J. Mechanical properties of dispersed ceramic nanoparticles in polymer composites for orthopedic applications. *Int. J. Nanomedicine* **5**, 299–313 (2010).

182. Chou, S. & Woodrow, K. A. Relationships between mechanical properties and drug release from electrospun fibers of PCL and PLGA blends. *J. Mech. Behav. Biomed. Mater.* **65**, 724–733 (2017).

183. Wang, Y., Ameer, G. A., Sheppard, B. J. & Langer, R. A tough biodegradable elastomer. *Nat. Biotechnol.* **20**, 602–606 (2002).

184. Akhtar, R., Sherratt, M. J., Cruickshank, J. K. & Derby, B. Characterizing the elastic properties of tissues. *Mater. Today* **14**, 96–105 (2011).

185. Liu, J., Zheng, H., Poh, P. S. P., Machens, H. G. & Schilling, A. F. Hydrogels for engineering of perfusable vascular networks. *Int. J. Mol. Sci.* **16**, 15997–16016 (2015).

186. Freed, L. E. *et al.* Advanced Tools for Tissue Engineering: Scaffolds, Bioreactors, and Signaling. *Tissue Enginering Part A* **12**, (2006).

187. Cohn, D. & Salomon, A. H. Designing biodegradable multiblock PCL/PLA thermoplastic elastomers. *Biomaterials* **26**, 2297–2305 (2005).

188. Yang, J., Webb, A. R., Pickerill, S. J., Hageman, G. & Ameer, G. A. Synthesis and evaluation of poly(diol citrate) biodegradable elastomers. *Biomaterials* **27**, 1889–1898 (2006).

189. Chen, Q. Z. *et al.* Characterisation of a soft elastomer poly(glycerol sebacate) designed to match the mechanical properties of myocardial tissue. *Biomaterials* **29**, 47–57 (2008).

190. Mazza, E. & Ehret, A. E. Mechanical biocompatibility of highly deformable biomedical materials. *J. Mech. Behav. Biomed. Mater.* **48**, 100–124 (2015).

191. Rai, R., Tallawi, M., Grigore, A. & Boccaccini, A. R. Synthesis, properties and biomedical applications of poly(glycerol sebacate) (PGS): A review. *Prog. Polym. Sci.* **37**, 1051–1078 (2012).

192. Lee, L. Y. *et al.* Biodegradable elastomer for soft tissue engineering. *Eur. Polym. J.* **45**, 3249–3256 (2009).

193. You, Z. & Wang, Y. Bioelastomers in Tisssue Engineering. in *Biomaterials for Tissue Engineering Applications A Review of the Past and Future Trends* (eds. Burdick, J. A. & Mauck, R. L.) 75–118 (SpringerWienNewYork, 2011).

194. Li, Y., Huang, W., Cook, W. D. & Chen, Q. A comparative study on poly(xylitol sebacate) and poly(glycerol sebacate): Mechanical properties, biodegradation and cytocompatibility. *Biomed. Mater.* **8**, 1–10 (2013).

195. Li, Y., Cook, W. D., Moorhoff, C., Huang, W. C. & Chen, Q. Z. Synthesis, characterization and properties of biocompatible poly(glycerol sebacate) pre-polymer and gel. *Polym. Int.* **62**, 534–547 (2013).

196. Annabi, N. *et al.* Elastomeric recombinant protein-based biomaterials. *Biochem. Eng. J.* **77**, 110–118 (2013).

197. Zhang, Y. N. *et al.* A Highly Elastic and Rapidly Crosslinkable Elastin-Like Polypeptide-Based Hydrogel for Biomedical Applications. *Adv. Funct. Mater.* **25**, 4814–4826 (2015).

198. Welsh, E. R. & Tirrell, D. A. Engineering the Extracellular Matrix: A Novel Approach to Polymeric Biomaterials . I . Control of the Physical Properties of Artificial Protein Matrices Designed to Support Adhesion of Vascular Endothelial Cells. *Biomacromolecules* **1**, 23–30 (2000).

199. Annabi, N. *et al.* Engineering a highly elastic human protein-based sealant for surgical applications. *Sci. Transl. Med.* **9**, eaai7466 (2018).

200. Li, Y., Thouas, A., Chen, Q. & Chen, Q. Biodegradable soft elastomers: synthesis/properties of materials and fabrication of scaffolds. *RSC Adv.* **2**, 8229–8242 (2012).

201. Lee, S.-H. *et al.* Elastic biodegradable poly(glycolide-co-caprolactone) scaffold for tissue engineering. *J. Biomed. Mater. Res. A* **66**, 29–37 (2003).

202. Wang, L., Zhang, Z. & Chen, H. Preparation and characterization of biodegradable thermoplastic Elastomers (PLCA/PLGA blends). *J. Polym. Res.* **17**, 77–82 (2010).

203. Li, L., Raghupathi, K., Song, C., Prasad, P. & Thayumanavan, S. Self-assembly of random copolymers. *Chem. Commun.* **50**, 13417–13432 (2014).

204. Xiong, M., Schneiderman, D. K., Bates, F. S., Hillmyer, M. A. & Zhang, K.

Scalable production of mechanically tunable block polymers from sugar. *Proc. Natl. Acad. Sci. U. S. A.* **111**, 8357–8362 (2014).

205. Schneiderman, D. K. High Performance Materials from Renewable Aliphatic Polyesters. (University of Minnesota, 2016).

206. Brutman, J. P., Hoe, G. X. De, Schneiderman, D. K., Le, T. N. & Hillmyer, M. A. Renewable, Degradable, and Chemically Recyclable Cross-Linked Elastomers. *Ind. Eng. Chem. Res.* **55**, 11097–11106 (2016).

207. Qian, H., Wohl, A. R., Crow, J. T., Macosko, C. W. & Hoye, T. R. A Strategy for Control of "Random" Copolymerization of Lactide and Glycolide: Application to Synthesis of PEG-b-PLGA Block Polymers Having Narrow Dispersity. *Macromolecules* **44**, 7132–7140 (2011).

208. Xu, B., Magli, A., Anugrah, Y., Koester, S. J. & Perlingeiro, R. C. R. Nanotopography-responsive myotube alignment and orientation as a sensitive phenotypic biomarker for Duchenne Muscular Dystrophy. *Biomaterials* **183**, 54–66 (2018).

209. Du, Y., Xue, Y., Ma, P. X., Chen, X. & Lei, B. Biodegradable, Elastomeric, and Intrinsically Photoluminescent Poly(Silicon-Citrates) with High Photostability and Biocompatibility for Tissue Regeneration and Bioimaging. *Adv. Healthc. Mater.* **5**, 382–392 (2016).

210. *Standard Test Methods for Vulcanized Rubber and Thermoplastic Elastomers — Tension (D412-16). ASTM Standard D412-16* (ASTM International, 2015). doi:10.1520/D0412-16.2.

211. Frohlich, T. *et al.* Synthesis of Thymoquinone−Artemisinin Hybrids : New Potent Antileukemia, Antiviral, and Antimalarial Agents. *ACS Med. Chem. Lett.* **9**, 534–539 (2018).

212. Murphy, D. P., Nicholson, T., Jones, S. W. & O'Leary, M. F. MyoCount: A software tool for the automated quantification of myotube surface area and nuclear fusion index. *Wellcome Open Res.* **4**, 2–11 (2019).

213. Wang, L., Wang, C., Wu, S., Fan, Y. & Li, X. Influence of the mechanical properties of biomaterials on degradability, cell behaviors and signaling pathways: Current progress and challenges. *Biomater. Sci.* **8**, 2714–2733 (2020).

214. Handorf, A. M., Zhou, Y., Halanski, M. A. & Li, W. J. Tissue stiffness dictates development, homeostasis, and disease progression. *Organogenesis* **11**, 1–15 (2015).

215. McKee, C. T., Last, J. A., Russell, P. & Murphy, C. J. Indentation versus tensile measurements of young's modulus for soft biological tissues. *Tissue Eng. - Part B Rev.* **17**, 155–164 (2011).

216. Pukacki, F. *et al.* The mechanical properties of fresh and cryopreserved arterial homografts. *Eur. J. Vasc. Endovasc. Surg.* **20**, 21–24 (2000).

217. De Hoe, G. X. *et al.* Sustainable Polyester Elastomers from Lactones: Synthesis, Properties, and Enzymatic Hydrolyzability. *J. Am. Chem. Soc.* **140**, 963–973 (2018).

218. Wu, L., Zhang, J., Jing, D. & Ding, J. 'Wet-state' mechanical properties of three-dimensional polyester porous scaffolds. *J. Biomed. Mater. Res. - Part A* **76**, 264–271 (2006).

219. Nijst, C. L. E. *et al.* Synthesis and Characterization of Photocurable Elastomers from Poly(glycerol-co-sebacate). *Biomacromolecules* **8**, 3067–3073 (2007).

220. Pappalardo, D., Mathisen, T. & Finne-Wistrand, A. Biocompatibility of Resorbable Polymers: A Historical Perspective and Framework for the Future. *Biomacromolecules* **20**, 1465–1477 (2019).

221. Sukanya, V. S. & Mohanan, P. V. Degradation of Poly(ε-caprolactone) and bio-interactions with mouse bone marrow mesenchymal stem cells. *Colloids Surfaces B Biointerfaces* **163**, 107–118 (2018).

222. Fentem, J., Curren, R. & Liebsch, M. *Guidance Document on Using In Vitro Data to Estimate In Vivo Starting Doses for Acute Toxicity*. https://ntp.niehs.nih.gov/iccvam/docs/acutetox_docs/guidance0801/iv_guide.pdf (2001).

223. Murray, L. M., Nock, V., Evans, J. J. & Alkaisi, M. M. The use of substrate materials and topography to modify growth patterns and rates of differentiation of muscle cells. *J. Biomed. Mater. Res. Part A* **104**, 1638–1645 (2016).

224. Pomerantseva, I. *et al.* Degradation behavior of poly(glycerol sebacate). *J. Biomed. Mater. Res. Part A* **91**, 1038–1047 (2009).

225. Tokiwa, Y. & Suzuki, T. Hydrolysis of polyesters by lipases. *Nature* **270**, 76–78 (1977).

226. Nakayama, A., Kawasaki, N., Arvanitoyannis, I., Iyoda, J. & Yamamoto, N. Synthesis and degradability of a novel aliphatic polyester: poly(β-methyl-δ-valerolactone-co-L-lactide). *Polymer (Guildf).* **36**, 1295–1301 (1995).

227. Ma, G., Song, C., Sun, H., Yang, J. & Leng, X. A biodegradable levonorgestrel-releasing implant made of PCL/F68 compound as tested in rats and dogs. *Contraception* **74**, 141–147 (2006).

228. Sun, H., Mei, L., Song, C., Cui, X. & Wang, P. The in vivo degradation, absorption and excretion of PCL-based implant. *Biomaterials* **27**, 1735–1740 (2006).

229. Gan, Z., Yu, D., Zhong, Z., Liang, Q. & Jing, X. Enzymatic degradation of poly(ε-caprolactone)/poly(DL-lactide) blends in phosphate buffer solution. *Polymer (Guildf).* **40**, 2859–2862 (1999).

230. Loh, X. J., Abdul Karim, A. & Owh, C. Poly(glycerol sebacate) biomaterial: synthesis and biomedical applications. *J. Mater. Chem. B* **3**, 7641–7652 (2015).

231. Zhang, K., Gao, H., Deng, R. & Li, J. Emerging Applications of Nanotechnology for Controlling Cell-Surface Receptor Clustering. *Angew. Chemie - Int. Ed.* **58**, 4790–4799 (2019).

232. Klein, S. *et al.* SARS-CoV-2 structure and replication characterized by in situ cryo-electron tomography. *bioRxiv* **19**, 1–11 (2020).

233. Bolívar-Monsalve, E. J. *et al.* Engineering bioactive synthetic polymers for biomedical applications: a review with emphasis on tissue engineering and controlled release. *Mater. Adv.* (2021) doi:10.1039/d1ma00092f.

234. Zhao, X., Dong, R., Guo, B. & Ma, P. X. Dopamine-Incorporated Dual Bioactive Electroactive Shape Memory Polyurethane Elastomers with Physiological Shape Recovery Temperature, High Stretchability, and Enhanced C2C12 Myogenic Differentiation. *ACS Appl. Mater. Interfaces* **9**, 29595–29611 (2017).

235. Coronavirus disease (COVID-19) pandemic. *World Health Organization* https://www.who.int/emergencies/diseases/novel-coronavirus-2019 (2021).

236. Buchrieser, J. *et al.* Syncytia formation by SARS-CoV-2-infected cells. *EMBO J.* **39**, 1–12 (2020).

237. Ryu, G. & Shin, H.-W. SARS-CoV-2 Infection of Airway Epithelial Cells. *Immune Netw.* **21**, e3-19 (2021).

238. Bussani, R. *et al.* Persistence of viral RNA, pneumocyte syncytia and thrombosis are hallmarks of advanced COVID-19 pathology. *EBioMedicine* **61**, (2020).

239. Zhang, H., Penninger, J. M., Li, Y., Zhong, N. & Slutsky, A. S. Angiotensin converting enzyme 2 (ACE2) as a SARS-CoV-2 receptor: molecular mechanisms and potential therapeutic target. *Intensive Care Med.* **46**, 586–590 (2020).

240. Huang, Y., Yang, C., Xu, X., Xu, W. & Liu, S. Structural and functional properties of SARS-CoV-2 spike protein : potential antivirus drug development for COVID-19. *Acta Pharmacol. Sin.* **41**, 1141–1149 (2020).

241. Hoffmann, M. *et al.* SARS-CoV-2 Cell Entry Depends on ACE2 and TMPRSS2 and Is Blocked by a Clinically Proven Article SARS-CoV-2 Cell Entry Depends on ACE2 and TMPRSS2 and Is Blocked by a Clinically Proven Protease Inhibitor. *Cell* **181**, 271–280 (2020).

242. Zhang, Z. *et al.* SARS-CoV-2 spike protein dictates syncytium-mediated lymphocyte elimination. *Cell Death Differ.* (2020) doi:10.1038/s41418-021-00782-3.

243. Hörnich, B. F., Großkopf, A. K., Schlagowski, S., Stahl-hennig, C. & Hahn, S. SARS-CoV-2 and SARS-CoV Spike-Mediated Cell-Cell Fusion Differ in Their Requirements for Receptor Expression and Proteolytic Activation. *J. Virol.* **95**, e00002-21 (2021).

244. Koenig, P. A. *et al.* Structure-guided multivalent nanobodies block SARS-CoV-2 infection and suppress mutational escape. *Science (80-.).* **371**, 1–15 (2021).

245. Xia, S. *et al.* Inhibition of SARS-CoV-2 (previously 2019-nCoV) infection by a highly potent pan-coronavirus fusion inhibitor targeting its spike protein that harbors a high capacity to mediate membrane fusion. *Cell Res.* **30**, 343–355 (2020).

246. Fan, X., Cao, D., Kong, L. & Zhang, X. Cryo-EM analysis of the post-fusion structure of the SARS-CoV spike glycoprotein. *Nat. Commun.* **11**, 1–10 (2020).

247. Pokhrel, S., Kraemer, B. R. & Mochly-Rosen, D. Natural variants in SARS-CoV-2 S protein pinpoint structural and functional hotspots; implications for prophylaxis strategies. *BioRxiv* (2021) doi:https://doi.org/10.1101/2021.01.04.425340.

248. Sasaki, M. *et al.* SARS-CoV-2 variants with mutations at the S1/S2 cleavage site are generated in vitro during propagation in TMPRSS2-deficient cells. *PLOS Pathog.* 1–17 (2021) doi:10.1371/journal.ppat.1009233.

249. Li, Z. *et al.* Development and clinical application of a rapid IgM-IgG combined antibody test for SARS-CoV-2 infection diagnosis. *J. Med. Virol.* **92**, 1518–1524 (2020).

250. Zhang, M., Xu, B., Siehr, A. & Shen, W. Efficient release of immunocaptured cells using coiled-coils in a microfluidic device. *RSC Adv.* **9**, 29182–29189 (2019).

251. Lichtenberg, J. Y., Ling, Y. & Kim, S. Non-Specific Adsorption Reduction Methods in Biosensing. *sensors* **19**, 1–17 (2019).

252. Peterson, S. L., Mcdonald, A., Gourley, P. L. & Sasaki, D. Y. Poly (dimethylsiloxane) thin films as biocompatible coatings for microfluidic devices: Cell culture and flow studies with glial cells. *J. Biomed. Mater. Res. Part A* **72**, 10–18 (2004).

253. Zhang, W., Choi, D. S., Nguyen, Y. H., Chang, J. & Qin, L. Studying Cancer Stem Cell Dynamics on PDMS Surfaces for Microfluidics Device Design. *Sci. Rep.* **3**, 1–8 (2013).

254. Boxshall, K. *et al.* Simple surface treatments to modify protein adsorption and cell

attachment properties within a poly(dimethylsiloxane) micro-bioreactor. *Surf. Interface Anal.* **38**, 198–201 (2006).

255. Liu, W. *et al.* Microfluidic device as a new platform for immunofluorescent detection of viruses. *Lab Chip* **5**, 1327–1330 (2005).

256. Zhang, H. & Chiao, M. Anti-fouling Coatings of Poly(dimethylsiloxane) Devices for Biological and Biomedical Applications. *J. Med. Biol. Eng.* 143–155 (2015) doi:10.1007/s40846-015-0029-4.

257. Hellmich, W. *et al.* Poly(oxyethylene) Based Surface Coatings for Poly(dimethylsiloxane) Microchannels. *Langmuir* **21**, 7551–7557 (2005).

258. Bar-on, Y. M., Flamholz, A., Phillips, R. & Milo, R. SARS-CoV-2 (COVID-19) by the numbers. *Elife* **9**, 1–15 (2020).

259. Bangs Laboraties, Inc. Product Data Sheet 644: PolyLink Protein Coupling Kit. www.bangslabs.com (2018).

260. Bangs Laboraties, Inc. TechNote 202: Microsphere Aggregation. www.bangslabs.com (2013).

261. Bangs Laboraties, Inc. TechNote 203: Washing Microspheres. www.bangslabs.com (2017).

262. Yoshii, E. Cytotoxic effects of acrylates and methacrylates: Relationships of monomer structures and cytotoxicity. *J. Biomed. Mater. Res.* **37**, 517–524 (1997).

263. Lerman, M. J., Lembong, J., Muramoto, S., Gillen, G. & Fisher, J. P. The Evolution of Polystyrene as a Cell Culture Material. *Tissue Eng. - Part B Rev.* **24**, 359–372 (2018).

264. Khalili, A. A. & Ahmad, M. R. A Review of Cell Adhesion Studies for Biomedical and Biological Applications. *Int. J. Mol. Sci.* **16**, 18149–18184 (2015).

265. Spielmann, H. *et al.* Interlaboratory Assessment of Alternatives to the Draize Eye Irritation Test in Germany. *Toxicol. Vitr.* **5**, 539–542 (1991).

Appendix 1. Effects of SARS-CoV-2 spike protein mutations on syncytia formation

A1.1 Introduction

The current pandemic caused by severe acute respiratory syndrome coronavirus 2 (SARS-CoV-2) has resulted in over 170 million confirmed cases and 3 million deaths worldwide (as of June 1, 2021).[235] SARS-CoV-2 infection results in symptoms ranging from a flu-like illness to severe pneumonia. SARS-CoV-2 infects ciliated cells, alveolar pneumocytes, epithelial progenitor cells, and other cell types in the airway and lungs.[236,237] Destruction of the epithelial lining in the lungs and presence of large, multinucleated pneumocytes in patients infected with SARS-CoV-2 is linked with the disease severity of COVID-19.[236] Specifically, post-mortem lung tissues in ~50% of patients infected with COVID-19 (41 patients) showed fused pneumocytes that were confirmed to have SARS-CoV-2 RNA and spike glycoprotein (denoted as S). This demonstrated that COVID-19 infection leads to the formation of cell syncytia—large fused multinucleated cells—in critical cases.[238]

SARS-CoV-2 entry into cells is initiated by interactions between SARS-CoV-2 S and its receptor, angiotensin-converting enzyme 2 (ACE2).[239] Next, the transmembrane

protease serine 2, TMPRSS2, or other surface/endosomal proteases cleave and prime S. The S protein, a trimer composed of three S1-S2 subunits, then undergoes conformational changes that result in fusion with the host cell membrane.[240,241]

The S protein expressed at the plasma membrane of cells can result in the formation of large, multinucleated syncytia in the presence of the ACE2 receptor.[236,242] This has been reported for other coronaviruses, including SARS-CoV-1 and MERS-CoV, in cell culture and tissues from infected individuals.[236] Cell culture experiments have shown that SARS-CoV-2 infection results in the expression of S at the cell surface and fusion with neighboring cells expressing the ACE2 protein. Expression of S and ACE2 alone is sufficient to trigger syncytia formation even without other viral proteins,[236,242] and therefore, the expression of S and ACE2 in cell culture can be used as an assay to examine different mutations in S, as differences in syncytia formation result.[242] In addition, the expression of TMPRSS2 allows for evaluation of different mutations that affect cleavage and priming of S,[243] and the effects of fusion inhibitors or antiviral therapies can be examined using this cell syncytia assay.[244,245]

Here, different mutations in the S protein were examined for their effects on syncytia formation (i.e., cell-cell fusion) using a fluorescence-based assay. The mutations included F1148R, D1146A, E1151K, and R1000E. The amino acids F1148, D1146, and E1151 are in the heptad repeat structure and the linker region upstream of the heptad repeat structure in the SARS-CoV-2 S, while R1000 is in the central helix region.[246] Based on structural analysis of S, the amino acids R1000 and E1151 are expected to form a salt-bridge. Mutations at these sites are expected to disrupt the salt-bridge and destabilize the S post-fusion structure. These mutations are expected to inhibit fusion by destabilizing the S

post-fusion structure, and this assay could help identify critical amino acids for this conformational change.

Various mutations in the cleavage site of S were also examined using this assay. As previously mentioned, S needs to be primed and cleaved to mediate fusion and entry. The mutations P812R, R815P, RR682-3SS, and RR682-3SS P812R, which are in the furin cleavage site,[247] were evaluated using this cell-cell fusion assay, and the effects of the fusion inhibitor, Camostat, and the Cathepsin inhibitor, E64D, were assessed.

A1.2 Experimental Section

A1.2.1 Cell-cell fusion assay for mutations in SARS-CoV-2 S

Vero cells were maintained in Dulbecco's modified Eagle's medium (DMEM; Cellgro) plus 10% FetalClone III (FC3; Hyclone) and 1% penicillin/streptomycin (Pen-Strep; Invitrogen). 24-hours before transfection, Vero cells were seeded at a density of 100,000 cells per well in 500 µL of Vero cell medium without antibiotics (DMEM with 10% FC3) in a 24 well plate. Cells were transfected with plasmid DNA using Lipofectamine 2000 (ThermoFisher Scientific) following the manufacturer's instructions. For transfection, 0.4 µg of the plasmid encoding mCherry, 0.3 µg of the plasmid encoding hACE2, and 0.3 µg of the plasmid encoding wild-type S (WT S) or S mutants were used. A control without spike (ΔS) was completed by transfecting cells with 0.4 µg and 0.3 µg of the plasmids encoding mCherry and hACE2, respectively. 24- and 48-hours post-transfection, the cells were counterstained with Hoechst 33342 nuclear stain (1:1000 volume dilution in PBS) for 10 minutes. The cells were then washed with PBS three times for one minute each. Samples were imaged with a 5× objective on a Zeiss Axio Observer

inverted fluorescence microscope equipped with 550/650 and 365/445 excitation/emission filters. Each condition was completed in triplicate.

A1.2.2 Image analysis of cell syncytia

Image analysis was completed in FIJI (ImageJ) to determine the cell syncytia size. 8-bit images were processed by first applying the *Phansalkar Auto Local* thresholding method with a radius of 10. The *analyze particles function* provided by FIJI was then used to determine the area of cells. Fluorescence regions with an area smaller than 150 μm^2 and cells on the edge of images were excluded from analyses. The condition without SARS-CoV-2 S was used to determine the background level of syncytia formation. A small percentage of cells with an area greater than 1000 μm^2 were observed for ΔS, so the percent of cells with an area greater than 1000 μm^2 were reported. A total of 9 non-overlapping image areas for each condition were analyzed.

A1.2.3 Cell-cell fusion assay for mutations in SARS-CoV-2 S cleavage site

Vero cells (p24) were seeded at a density of 100,000 cells per well in 500 µL medium without antibiotics (DMEM with 10% FC3) in a 24 well plate. 24-hours post-seeding, cells were transfected with plasmid DNA using Lipofectamine 2000 (ThermoFisher Scientific) following the manufacturer's instructions. For transfection, 0.4 µg mCherry plasmid, 0.1 µg hACE2 plasmid, 0.1 µg TMPRSS2 plasmid (when added), and 0.4 µg pCG-SARS-CoV-2 S (WT S) plasmid or S mutant plasmids were used. At 3 hours post-transfection, Camostat or E64D prepared in DMSO were added at concentrations of 100 and 40 µM, respectively. At 36 hours post-transfection, the cells were imaged with a 5× objective on a Zeiss Axio Observer inverted fluorescence

microscope equipped with 550/650 excitation/emission filters. Each condition was completed in duplicate.

A1.3 Results and Discussion

A1.3.1 Mutations in SARS-CoV-2 S prevent the formation of cell syncytia

Mutations in the S protein, F1148R, D1146A, E1151K, and R1000E, were examined using the cell-cell fusion assay and compared to wild-type S (WT S) and without expression of S (ΔS). As shown in Figure 44, Vero cells were transfected with plasmid DNA encoding the following: mCherry (to confirm transfection and visualize cell syncytia), SARS-CoV-2 S (WT or mutants), and human ACE2 (hACE2). The cells were examined at 24- and 48-hours post-transfection.

After 24 hours, syncytia were observed for WT S and the S mutants D1146A and E1151K, while the S mutants F1148R and R1000E did not show syncytia and were similar to the ΔS condition (Figure 45). At 48 hours post-transfection, larger syncytia were observed (Figure 46). Again, the WT S, D1146A mutant, and E1151K mutant showed large syncytia. The F1148R and R1000E mutants did not form cell syncytia and were similar in size to the ΔS condition.

The images collected at 48 hours were used to quantify cell size. From this, the percentage of cells with an area greater than 1000 μm^2 was determined for each condition (this area was used because the ΔS condition had a low percentage of cells (~6%) with a size greater than 1000 μm^2) (Figure 47). These results suggest Vero cells readily form small syncytia, as some syncytia were observed without S protein. ΔS, F1148R, and R1000E had a significantly lower percentage of cells with an area greater than 1000 μm^2, as compared

to WT S. Although some large syncytia were observed, the D1146A mutation had a significantly lower percentage of cells with an area greater than 1000 μm^2.

These findings suggest that F1148R and R1000E mutants strongly disrupt binding between the S protein and ACE2. In contrast, the D1146A mutant resulted in fewer large syncytia, suggesting this mutation may disrupt binding to a small extent, and the E1151K mutant does not affect the formation of syncytia. Other quantitative assays, such as cell entry or immunofluorescence assays, may provide more insight into the S protein mutations. Overall, these results suggest that the mutants F1148R and R1000E may affect the post-fusion structure of S, although additional studies should be completed to assess whether these mutations result in the expression of functional S at the plasma membrane.

A1.3.2 Mutations in the SARS-CoV-2 S cleavage site prevent the formation of cell syncytia

SARS-CoV-2 entry is initiated by interactions between S and its receptor ACE2, followed by cleavage and priming of S with the surface protease TMPRSS2. Two different entry pathways have been proposed for SARS-CoV-2, including early and late pathways.[248] Early entry involves direct fusion with the cell membrane, which TMPRSS2 mediates. In contrast, late entry involves endocytosis of the virus, which requires cathepsin, a lysosomal protease.[248] Camostat mesylate and E64D, known inhibitors of SARS-CoV-2 viral entry, inhibit early and late viral infection, respectively.[248]

In this assay, Vero cells were transfected with plasmids encoding mCherry, S, and hACE2 (Figure 48). Also, cells were transfected either with or without TMPRSS2, as shown in Figures 49 and 50, respectively. After 3 hours post-transfection, Camostat and E64D were added, followed by imaging the cell syncytia 36 hours post-transfection. Images of cell syncytia with TMPRSS2 are shown in Figure 49 with or without inhibitors

(Camostat or E64D). The mutant, R815P, inhibited syncytia formation in the presence of TMPRSS2, while P812R, RR682-3SS, and RR682-3SS formed syncytia similar to pCG-SARS-CoV-2 (WT S) when TMPRSS2 was expressed. pCG-SARS-CoV-2 S, RR682-3SS, and RR682-3SS P812R had very small to no syncytia with the addition of Camostat. The syncytia for P812R were slightly smaller in the presence of Camostat but not completely inhibited from forming. With E64D, all cell syncytia looked similar to those without inhibitors. Without TMPRSS2 (Figure 50), pCG-SARS-CoV-2 S, P812R, and RR682-3SS P812R showed the formation of large syncytia. RR682-3SS and R815P did not show syncytia. With the addition of E64D, the syncytia observed for P812R and RR682-3SS were smaller.

In the presence of TMPRSS2, Camostat inhibited cell syncytia with pCG-SARS-CoV-2 S, but E64D did not affect the cell syncytia. This is consistent with previous work showing that TMPRSS2-mediated fusion is the dominant pathway for fusion.[248] RR682-3SS and RR682-3SS P812R were similar to WT S. Also, RR682-3SS did not form cell syncytia without the presence of TMPRSS2, suggesting that this mutation relies on TMPRSS2 for cell fusion. The P812R mutant did not appear to have a preferential pathway for entry and fusion, as neither E64D nor Camostat completely prevented the formation of syncytia. Additionally, the P812R mutant restored the formation of the cell syncytia without TMPRSS2 in the RR682-3SS P812R mutant (the RR682-3SS mutant did not have cell syncytia without TMRPSS2). The R815P mutation, a critical cleavage site for SARS-CoV-2, disrupted the formation of cell syncytia both with and without TMRPSS2, suggesting that this mutation prevents fusion via both pathways. Overall, this work identifies key mutations in SARS-CoV-2 S critical to disrupting syncytia formation.

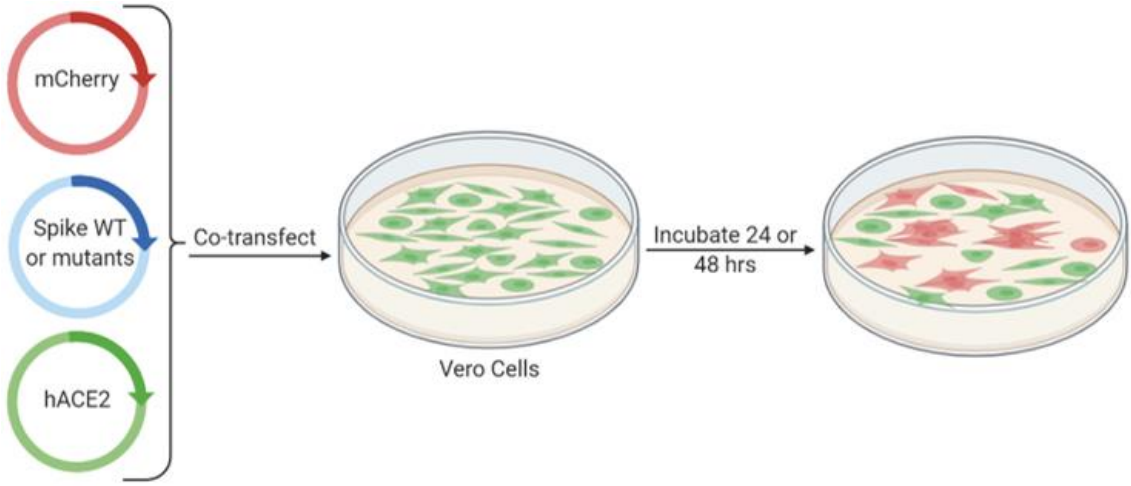

Figure 44. Cell-cell fusion assay used to evaluate mutations in SARS-CoV-2 S. The fusion assay was completed by transfecting Vero cells with plasmids for mCherry, spike (S, either wild-type (WT) or mutants), and human-ACE2 (hACE2) cell receptor. After 24 or 48 hours, the cell syncytia were imaged using fluorescence microscopy. This image was adapted from "AAV Production by Triple Transfection", by BioRender.com (2021). Retrieved from https://app.biorender.com/biorender-templates.

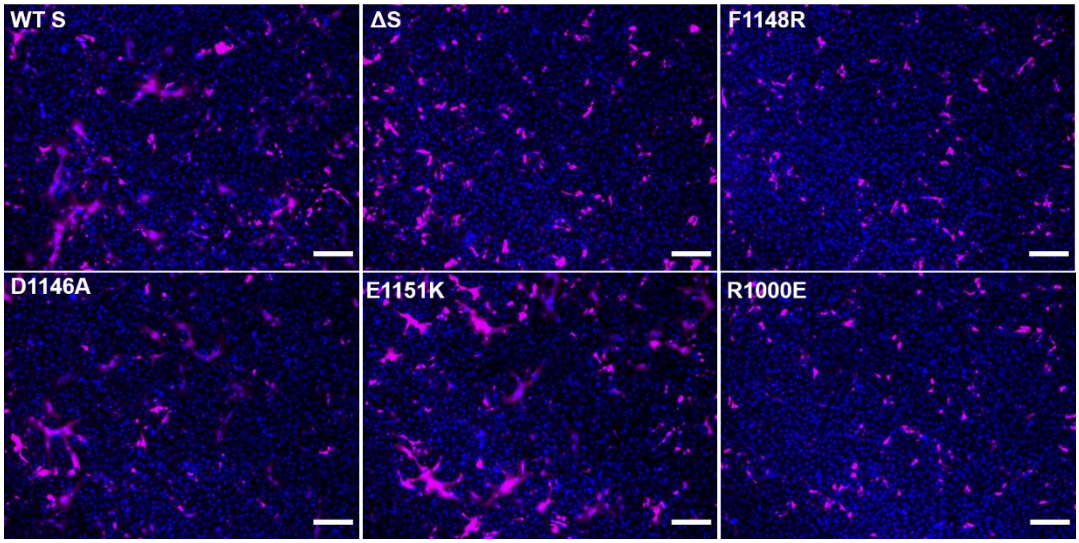

Figure 45. The cell-cell fusion assay 24 hours post-transfection SARS-CoV-2 S mutants. The pink color is the mCherry protein present in cell syncytia, and the blue color corresponds to the cell nuclei counterstain, Hoechst 33342. Scale bar is 200 µm.

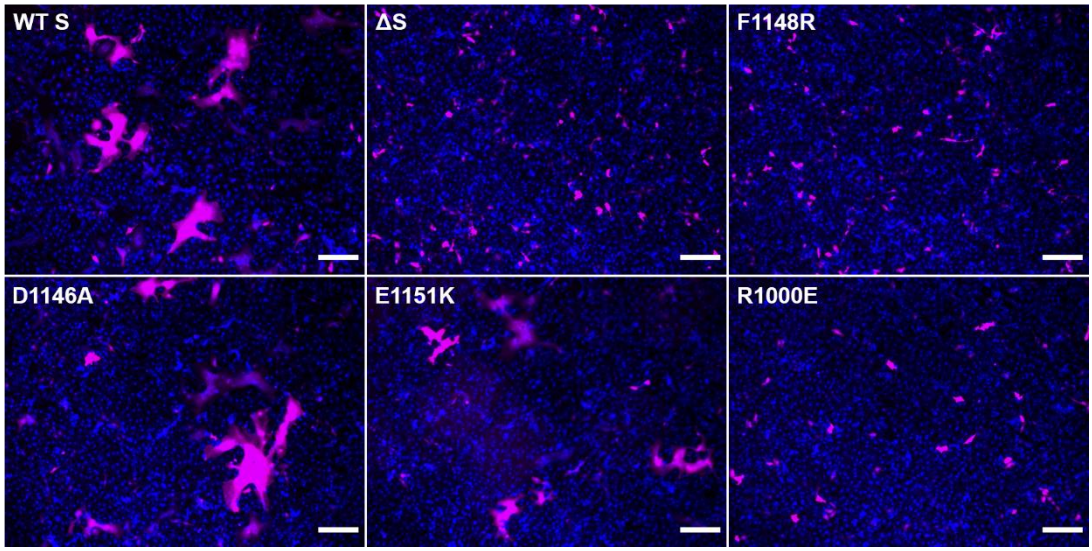

Figure 46. The cell-cell fusion assay 48 hours post-transfection SARS-CoV-2 S mutants. The pink color is the mCherry protein present in cell syncytia, and the blue color corresponds to the cell nuclei counterstain, Hoechst 33342. Scale bar is 200 µm.

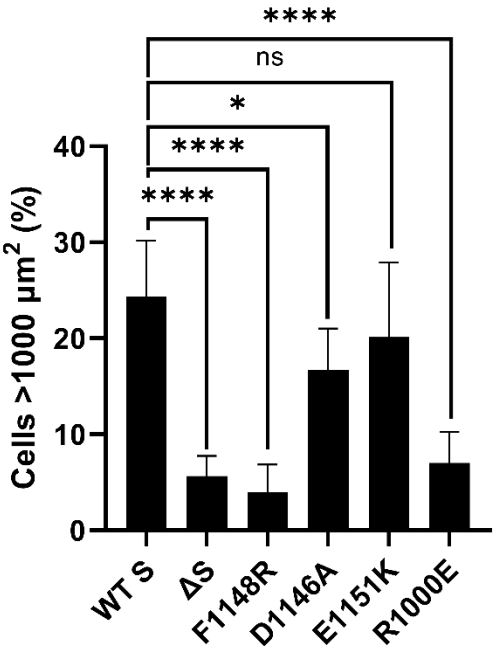

Figure 47. Percentage of cells with an area greater than 1000 μm^2 at 48 hours post-transfection. The percentage of cells with an area greater than 1000 μm^2 were analyzed for each mutant. Error bars represent standard deviation, ns=not significant, *p-value<0.05, ****p-value<0.05, ****p-value<0.0001, Welch's 1-way ANOVA with Dunnett's test, n=9.

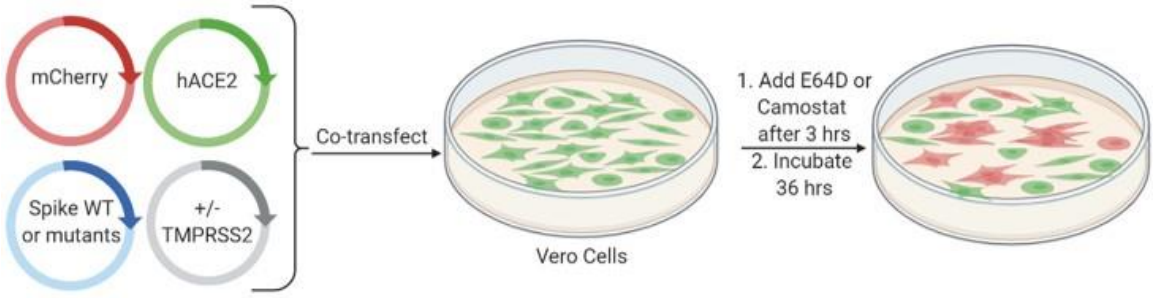

Figure 48. Cell-cell fusion assay used to assess mutations in the SARS-CoV-2 S cleavage site. The assay was completed by transfecting Vero cells with plasmids for mCherry, spike (either wild-type (WT) or mutants), human-ACE2 (hACE2) cell receptor, and TMPRSS2. Either E64D or Camostat were added 3 hours post-transfection. After 36 hours, the cell syncytia were imaged using fluorescence microscopy. This image was adapted from "AAV Production by Triple Transfection", by BioRender.com (2021). Retrieved from https://app.biorender.com/biorender-templates.

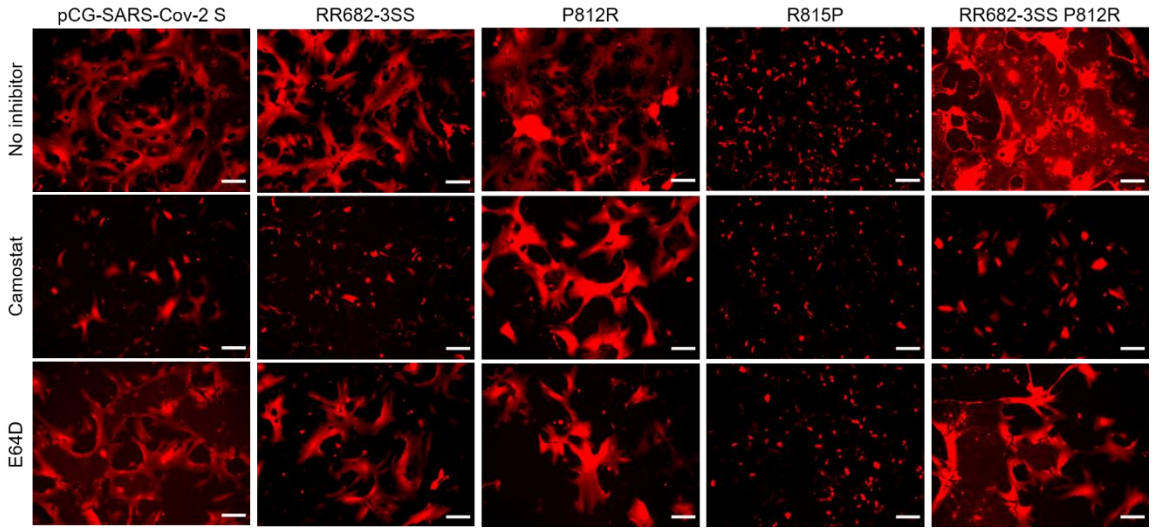

Figure 49. Fusion assay for SARS-CoV-2 S cleavage mutants (36 hours post-transfection). Cells were transfected with TMPRSS2. The red color corresponds to expression of mCherry in transfected cells. The fusion assay was completed with either no inhibitor, Camostat, or E64D. Scale bar is 200 µm.

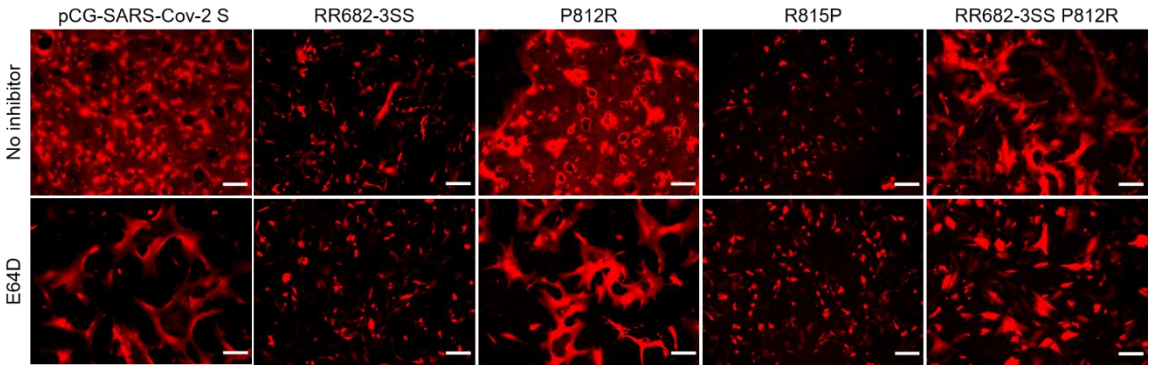

Figure 50. Fusion assay for SARS-CoV-2 S cleavage mutants (36 hours post transfection). TMPRSS2 was not transfected in this assay. The red color corresponds to expression of mCherry in transfected cells. The fusion assay was completed with either no inhibitor or E64D. Scale bar is 200 µm.

Appendix 2: Development of microfluidic SARS-CoV-2 detection device

A2.1 Introduction

The development of SARS-CoV-2 detection methods was imperative at the beginning of the COVID-19 pandemic to prevent virus transmission and assure timely treatment of infected individuals.[249] Additionally, the development of fast and portable assays is essential for easy access to testing. Therefore, we designed a microfluidic-based SARS-CoV-2 detection device coupled with a cell phone-based fluorescent detection system. As shown in Figure 51, the goal of this work was first to develop a poly(dimethylsiloxane) (PDMS) microfluidic channel conjugated with antibodies targeting the SARS-CoV-2 spike protein (S), a large number of which cover the surface SARS-CoV-2 (Figure 51a).[240] It was expected that samples containing SARS-CoV-2 would be specifically captured by the S antibody, thus concentrating the virus in the microfluidic channel (Figure 51b). Next, fluorescent microspheres were conjugated with SARS-CoV-2 S antibodies, and these microspheres would allow for specific detection of SARS-CoV-2 using fluorescent microscopy (Figure 51c). Ultimately, this microfluidic device would be coupled with a cell phone-based detection device.

The work presented here had two specific aims with the overall goal of developing a microfluidic channel: (1) the preparation and evaluation of a microfluidic channel decorated with SARS-CoV-2 S antibody for specific capture of SARS-CoV-2 and (2) the development of SARS-CoV-2 S antibody conjugated fluorescent beads for detection of SARS-CoV-2.

A2.2 Materials and Methods

A2.2.1 Preparation of PDMS microfluidic device and PDMS disks

The PDMS microfluidic device was prepared as previously reported.[250] Briefly, a silicon master was first prepared with a 50 mm long, 2 mm wide, and 75 µm high ridge. PDMS (Sylgard 184 PDMS precursor and the curing agent mixed at a 10:1 weight ratio) was cast against the master to form a microchannel, vacuumed in a desiccator for 1 hr to remove air bubbles, and cured at 37 °C for 24 hours. The PDMS channel was then removed from the master and further cured for an additional 72 hours at 80 °C. An inlet and outlet were punched using a 1.0 mm biopsy punch at each end of the channel. The PDMS channel and a glass slide were sonicated in 70% ethanol for 20 minutes and Milli-Q water for 10 minutes. The channel and slide were rinsed with water and 100% ethanol, followed by drying with filtered air and stored in a vacuum desiccator until further use. The PDMS channel and glass slide were then plasma treated for 2 mins and bonded to form the microfluidic device (Figure 52).

PDMS disks were first used to evaluate antibody conjugation and specific capture of SARS-CoV-2 via S antibody. PDMS disks were prepared by casting Sylgard 184 PDMS precursor and the curing agent at a 10:1 ratio in a 10 cm petri dish, vacuuming in a desiccator for 1 hr to remove air bubbles, and curing at 37 °C for 24 hours followed by 80 °C for 72 hours. PDMS disks were then punched from the 10 cm dish using an 8 mm biopsy punch. PDMS disks were sonicated and washed as described above, and plasma treated for 2 minutes immediately before use.

A2.2.2 Conjugation of antibodies to PDMS

The antibody conjugation to PDMS was described previously.[250] A solution of 3-glycidoxypropyltrimethoxysilane (3-GPTMS, Sigma Aldrich) was prepared with 4.5 mL 100% ethanol, 0.1 mL acetic acid, and 1 mL 3-GPTMS. PDMS disks were placed in a 24 well plate and incubated in 3-GPTMS solution for 16 hours. PDMS disks were then washed with ethanol and PBS (1X, HyClone, pH 7.2). The SARS-CoV-2 S antibody, 1A9 (GeneTex), was diluted at a 1:100 volume ratio in PBS with a final concentration of 10 μg mL^{-1} (0.8 mL of antibody solution was added to each well). PDMS surfaces were then passivated with 5% BSA (Fisher Scientific) in PBS for 1 hr before use.

A2.2.3 Production of fluorescent SARS-CoV-2 virus-like particles

Fluorescent SARS-CoV-2 virus-like particles (VLPs) displaying the SARS-CoV-2 S protein were used in this work. HEK-293T17 cells and all plasmids were provided by Prof. Louis Mansky's laboratory at the University of Minnesota. HEK-293T17 cells were maintained in Dulbecco's modified Eagle's medium (DMEM; Cellgro) plus 10% FetalClone III (FC3; Hyclone) and 1% penicillin/streptomycin (Pen-Strep; Invitrogen). VLPs were produced via transient transfection of HEK-293T17 cells using GenJet following the manufacturer's instructions. Briefly, 10 mL 293T17 cells were seeded at a density of 9×10^6 cells/mL in a 10-cm dish. 24 hours after cell seeding, the medium was changed and replaced with 5 mL of medium one hour before transfection. For each 10-cm dish, 15 μL of GenJet was added to 235 μL of serum-free medium, and 4 μg of HIV-1 Gag plasmid, 0.5 μg HIV-1 mcherry Gag plasmid, and 0.5 μg SARS-CoV-2 S plasmid were added to a final volume of 250 μL per plate. The GenJet and plasmid DNA solutions were mixed and added to the cells. After 24 hours post-transfection, the supernatant was

collected, centrifuged at 1800 rpm for 5 minutes, and filtered using a 0.22 μm filter. The VLPs were then centrifuged over an Optiprep gradient using high speed ultracentrifugation, as previously described.[162]

A2.2.4 Conjugation of antibodies to fluorescent microspheres

0.1 μm red carboxylate-modified polystyrene microspheres (FluoSpheres, Invitrogen) were conjugated with SARS-CoV-2 S antibody using the PolyLink Protein Coupling Kit (Bangs Laboratories) following the manufacturer's instructions with slight modifications. Namely, BSA, Tween-20, and multiple sonication steps were introduced to minimize microsphere aggregation. Microspheres were diluted in PolyLink coupling buffer [either 1:2 or 1:4 (volume:volume) dilution with a final volume of 100 μL] and centrifuged at 14krcf for 10 mins. The supernatant was then removed, and 32 μL of PolyLink coupling buffer was added, followed by sonication for 10 mins and centrifugation as described above. 13.6 μL of PolyLInk coupling buffer was added, followed by sonication for 10 mins. Next, 10 mg of 1-ethyl-3-(3-dimethyl aminopropyl)carbodiimide (EDAC) was prepared in 50 μL of PolyLink coupling buffer and immediately added to the microspheres at a ratio of 0.035 μL EDAC solution per μL of initial microsphere solution. The EDAC solution with microspheres was sonicated for 15 mins to activate the EDAC. AlexaFluor 488 conjugated goat anti-mouse secondary antibody (Invitrogen, 0.4 μL antibody per μL of initial microsphere solution) was diluted in PolyLink coupling buffer containing bovine serum albumin (BSA; the final concentration of BSA after antibody dilution was 0.1%), and 40 μL was added to the microspheres. Samples were incubated for 1 hr and sonicated every 10 mins. 100 μL of 0.1% Tween-20 in PolyLink wash/storage buffer was then added to the microspheres, followed by centrifugation at 14krcf for 10 mins, removing

supernatant resuspension in PolyLink wash/storage buffer with 100 µL 0.1% Tween-20. This washing step was repeated twice.

A2.2.5 Fluorescent imaging

All images were acquired using a Zeiss LSM 700 confocal microscope with a Plan-Apochromat 100×/1.40-NA oil objective.

A2.3 Results and Discussion

A2.3.1 Microfluidic device for SARS-CoV-2 capture shows non-specific binding

The PDMS microfluidic channel was conjugated with antibodies for SARS-CoV-2 S through epoxy chemistry, as shown in Figure 53. The device was then evaluated for specific capture of fluorescent SARS-CoV-2 VLPs. PDMS disks conjugated with antibodies were first tested for the specific capture of SARS-CoV-2 VLPs. PDMS disks after epoxy conjugation or addition of SARS-CoV-2 S antibodies were evaluated for specific capture of VLPs, as shown in Figure 54. PDMS surfaces (either epoxy or antibody conjugated PDMS) were passivated with BSA for 1 hour for this experiment. BSA has previously been shown to minimize non-specific binding to PDMS.[251] Next, red fluorescent VLPs were added to PDMS disks for 10 minutes and washed once with PBS before imaging. From the images, the VLPs can be observed on antibody conjugated PDMS surfaces after passivation (Figure 54, top). Additionally, epoxy conjugated PDMS surfaces were also evaluated to determine if the capture of VLPs was specific. However, non-specific adsorption of VLPs was observed on the epoxy conjugated PDMS surface (Figure 54, bottom).

Ultimately, methods need to be developed to minimize non-specific adsorption of VLPs to the PDMS surface based on this microfluidic device design. BSA has previously

been used to minimize non-specific adsorption,[251–253]. Previous experiments had been completed to assess the effects of different solutions on non-specific adsorption of VLPs on unmodified PDMS surfaces, including BSA (10% in PBS),[252,253] Tween-20 (5% in water),[254] casein (0.2% in PBS),[255] and Pluronic F-127 (10% in water).[254] BSA, Tween-20, and Casein were found to minimize non-specific adsorption on unmodified PDMS surfaces. However, after epoxy conjugation, we observed non-specific adsorption even with the addition of BSA, and, therefore, different methods for surface passivation should be tested. Possible approaches may include chemically conjugating the surface to prevent non-specific adsorption, such as modification with poly(ethylene glycol) or oligo(ethylene glycol).[251,256,257]

A2.3.2 Antibodies are conjugated to fluorescent microspheres using EDAC coupling

Conjugation of antibodies to fluorescent microspheres was attempted. A commercial kit based on carbodiimide coupling chemistry to conjugate proteins to carboxylated microspheres was used for these experiments. A microsphere size of 0.1 μm was used here to match the size of the SARS-CoV-2 virus.[258] An antibody conjugated with AlexaFluor 488 was used to assess the procedure for antibody conjugation, in which red and green fluorescent colocalization indicated that the antibody was bound to the microspheres. The overall protocol for conjugation of microspheres was as follows: (1) washing microspheres, (2) addition and activation of EDAC, (3) antibody conjugation to microspheres, and (4) washing antibody conjugated microspheres to remove excess antibody. First, different surfactants were tested during the antibody conjugation step, and fluorescence microscopy was used to assess for: (1) fluorescent colocalization (indicating antibodies were bound) and (2) the degree of microsphere aggregation. The addition of

0.1% BSA solution during antibody conjugation did not minimize aggregation, but fluorescent colocalization was observed, suggesting antibodies were bound to the microspheres (Figure 55a). The addition of 0.1% Tween-20 minimized microsphere aggregation; however, the presence of Tween-20 prevented the conjugation of antibodies (Figure 55b). Therefore, an optimized procedure was used here for two different microsphere concentrations, in which BSA and Tween-20 were added during the antibody conjugation and washing steps, respectively. Yellow and red colocalization was observed using this procedure (Figure 56), suggesting antibodies were bound to the microspheres. However, the microspheres aggregated during this procedure. Further optimization is necessary to minimize aggregation, and additional experiments are required to determine the optimal microsphere and antibody concentrations.[259] Different surfactants and surfactant concentrations may be used to reduce aggregation.[259] Also, small microspheres (<1 μm) are easily aggregated during washing procedures involving centrifugation.[260] Thus, alternative washing procedures, such as using the commercially available VivaSpin devices, may help minimize microsphere aggregation.[261]

A2.4 Conclusions

In this work, we developed a microfluidic-based device for the detection of SARS-CoV-2. This device was expected to capture SARS-CoV-2 through interactions between antibodies targeting the S protein and SARS-CoV-2 S, followed by detection with fluorescent microspheres targeting SARS-CoV-2 S. A microfluidic channel was developed, and conjugation of the channel with SARS-CoV-2 S antibody was completed. However, non-specific adsorption of SARS-CoV-2 VLPs was observed on PDMS surfaces, and more work needs to be completed to reduce this. Additionally, a protocol was

developed for antibody conjugation to fluorescent microspheres; however, more work needs to be completed to minimize the observed microsphere aggregation.

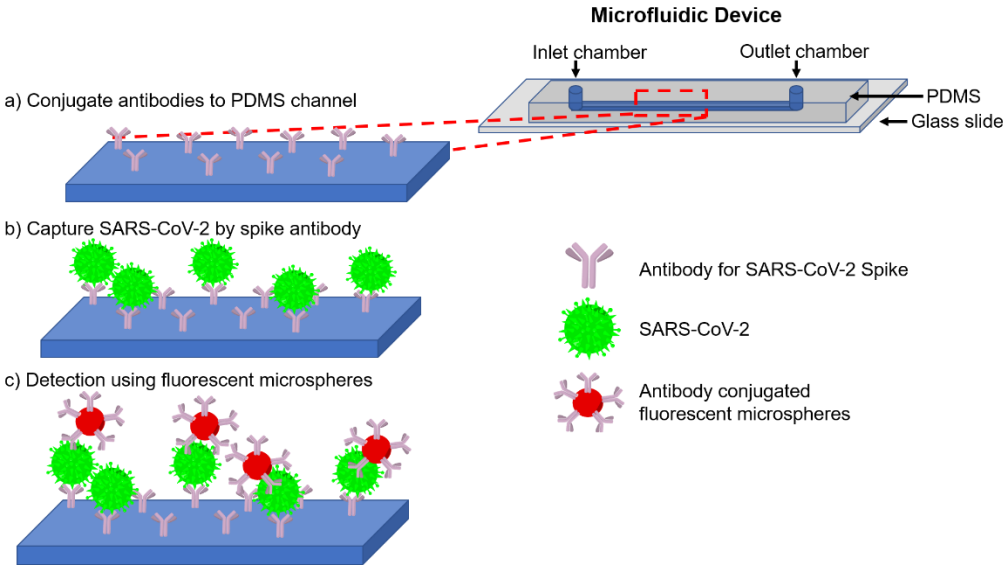

Figure 51. Overview of microfluidic device for detection of SARS-CoV-2. The microfluidic device is shown on the top right. (a) Antibodies (Ab) targeting SARS-CoV-2 S are conjugated to the microfluidic channel. (b) Samples containing virus would be introduced to the channel, and SARS-CoV-2 would be captured by the antibody. (c) SARS-CoV-2 S antibody conjugated fluorescent microspheres would be used to detect SARS-CoV-2 using fluorescence.

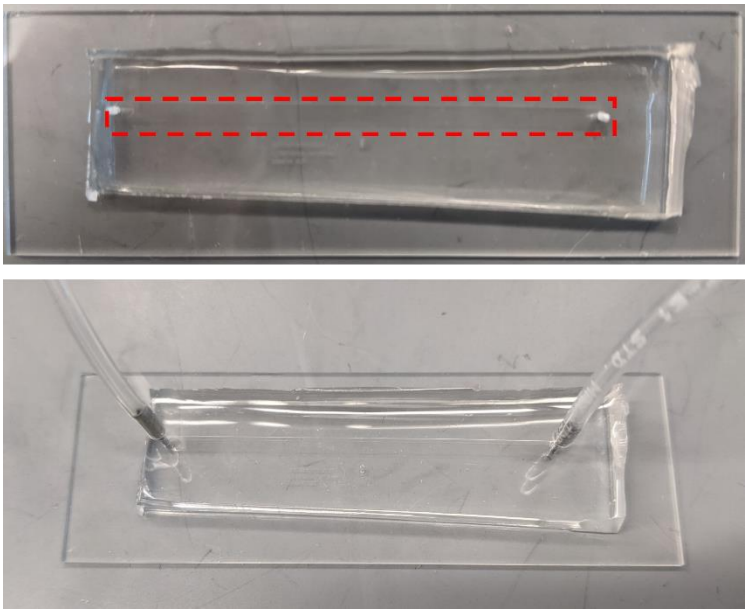

Figure 52. The fabricated microfluidic device. The PDMS channel adhered to a glass slide is shown, and the channel is outlined in red (top). The PDMS microfluidic device with the inlet and outlet channels connected to tubing (bottom).

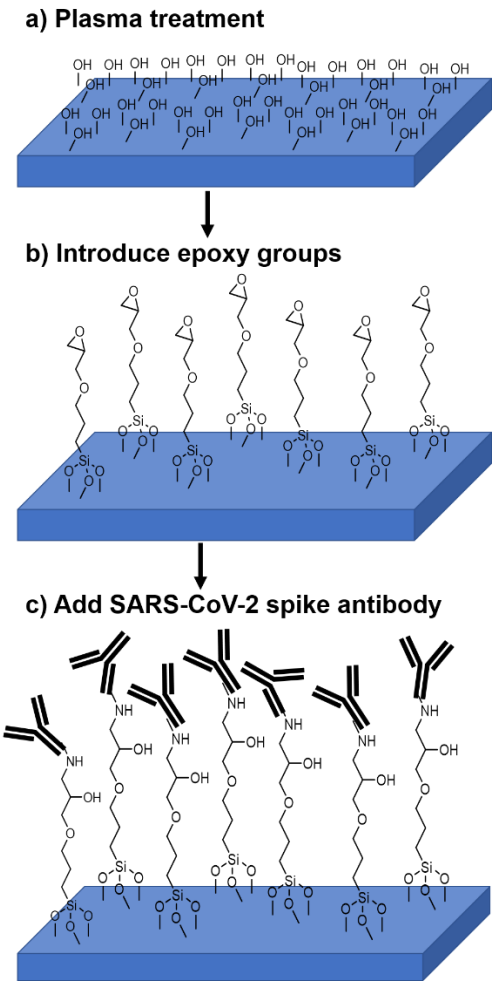

Figure 53. Surface modification of PDMS microchannel with antibodies. (a) Plasma treatment is completed to introduce hydroxyl groups. (b) 3-glycidoxypropyltrimethoxysilane (3-GPTMS) is added to introduce reactive epoxy groups as sites for antibody binding. (c) Addition of SARS-CoV-2 S antibodies which react with the epoxy groups to form an antibody conjugated PDMS channel.

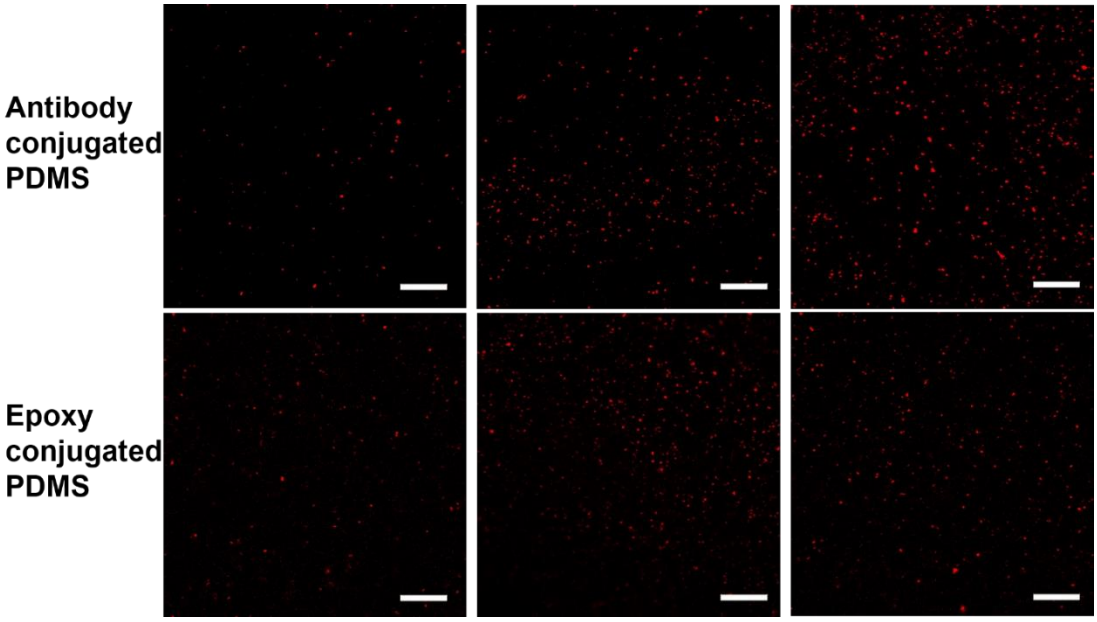

Figure 54. SARS-CoV-2 VLPs captured on PDMS. Antibody conjugated PDMS (top) and epoxy conjugated PDMS (bottom) both show VLPs (shown in red) on the surfaces, suggesting non-specific adsorption of VLPs. Scale bar is 10 μm.

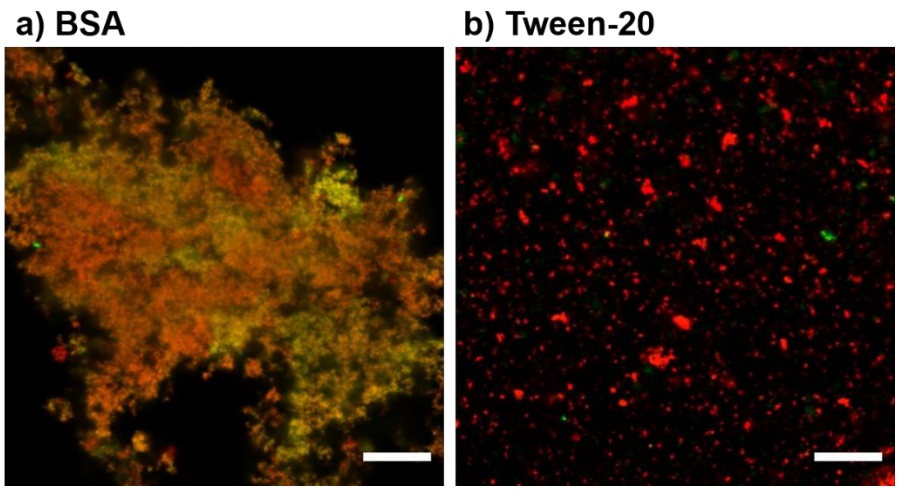

Figure 55. The effects of surfactants, BSA and Tween-20, on antibody conjugation to microspheres. BSA or Tween-20 were added during the antibody conjugation step. (a) BSA solution allowed for conjugation of microspheres (red) with antibody (green) but resulted in aggregation of microspheres. (b) Tween-20 minimized the aggregation of microspheres but prevented the conjugation of antibodies (green) to microspheres (red). Scale bar is 10 μm.

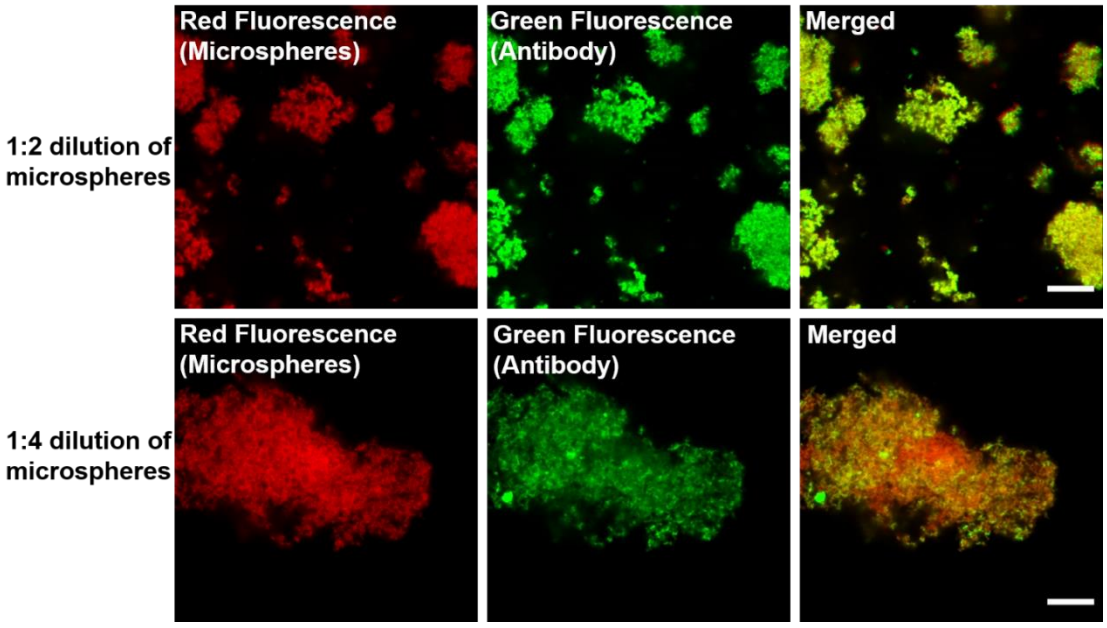

Figure 56. Effect of microsphere concentration on antibody conjugation. A 1:2 dilution of the microspheres resulted in antibody conjugation, but the microspheres were aggregated (top). A 1:4 dilution of microspheres resulted in antibody conjugation with larger aggregates (bottom). Scale bar is 10 μm.

Appendix 3. Cytocompatibility of PLLA-PMCL-PLLA elastomers

This work was reprinted with permission from Reisman, L.; Siehr, A.; Horn, J.; Batiste, D.C.; Kim, H.J.; De Hoe, G.X.; Ellison, C.J.; Shen, W.; White, E.M.; and Hillmyer, M.A. "Respirometry and Cell Viability Studies for Sustainable Polyesters and Their Hydrolysis Products." *ACS Sustainable Chem. Eng.* **2021**, (9) 2736-2744. pubs.acs.org/doi/10.1021/acssuschemeng.0c08026.

A3.1 Introduction

Significant research effort has been directed toward the development of sustainable plastics that are high-performance, bioderived, and/or degrade into nontoxic byproducts in natural or engineered environments (i.e., industrial composting facilities). In this work, the triblock copolymer, poly(L-lactide)-co-poly(γ-methyl-ε-caprolactone)-co-poly(L-lactide) (PLLA-PMCL-PLLA) was examined for potential use as a nontoxic, compostable material and for use in biomedical applications. We report the low cytotoxicity of poly(γ-methyl-ε-caprolactone) (PMCL)-based materials and the hydrolysis product of PMCL, sodium 6-hydroxy-4-methylcaproate. The concentration of sodium 6-hydroxy-4-methylcaproate that leads to 50% cell death (TD_{50}) is 179 mM, a value that is similar to that of the hydrolysis product of polycaprolactone and higher than that of the hydrolysis product of polylactide.

A3.2 Experimental Section

A3.2.1 Preparation of PLLA−PMCL−PLLA Films

PLLA−PMCL− PLLA films were processed using a Carver hydraulic press (Carver 5370 AutoFour/4819 ASTM Molding Laboratory Press). The polymer (1 g) was placed on a Teflon sheet and pressed at 180 °C with 700 lbs for 3 min followed by pressing with 3000

lbs for 5 min. The film was then rapidly cooled in a water-injected press. Circular samples were cut from this film using a biopsy punch. Polycaprolactone (PCL, Sigma Aldrich, average Mn = 45 kDa) control films were fabricated in a similar manner.

A3.2.2 Live/Dead Staining for Cells Cultured on Polymer Films

Polymer films (0.3 mm thick and 8 mm in diameter) were each attached to a cover glass through a thin layer of vacuum grease (the cover glass and vacuum grease were autoclaved) and then placed in a 24 well tissue culture plate. The films were soaked in Pen−Strep (5%) for 2 hours for sterilization, followed by washing with phosphate-buffered saline (PBS) three times. NIH 3T3 fibroblasts were seeded on the polymer films at a density of 50,000 cells per well, and cultured in Dulbecco's modified Eagle medium (DMEM) supplemented with 10% fetal bovine serum and 1% Pen−Strep in a tissue incubator (37 °C, 5% carbon dioxide, 100% relative humidity). At 24 hours post-seeding, the cells were stained with the live/dead reagents, ethidium homodimer and calcein AM (0.1% v/v), for 30 min in the dark. Each sample was then flipped upside down onto a cover glass slide and imaged on a Zeiss Axio Observer inverted microscope with a 5× objective. Cells seeded directly on the bottom surface in the culture plate [tissue culture polystyrene (TCPS)] and cells seeded on PCL films were examined as controls.

A3.2.3 Alamar Blue Assay for Cells Cultured on Polymer Films

Polymer films (0.3 mm thick and 6 mm in diameter) were each attached to the bottom of a well in a 96 well tissue culture by applying a thin layer of autoclaved vacuum grease underneath the films. The polymer films were soaked in Pen−Strep (5%) for 2 hours for sterilization and washed with PBS three times followed by incubation in the cell culture medium overnight prior to cell seeding. Fibroblasts were seeded at a density of 5000 cells

per well and cultured for 24 hours, followed by the Alamar Blue assay to determine cell viability. Fibroblasts seeded on the TCPS and PCL films were examined as controls. To perform the Alamar Blue assay, the cell culture medium was replaced with phenol red-free DMEM containing 10% v/v Alamar Blue reagent (Bio-Rad), followed by incubation for 4 hours. The medium of each sample (100 μL) was transferred to a new 96-well plate, and the fluorescence signal with excitation/emission at 560/590 nm was measured using a BioTek Cytation 3 Cell Imaging MultiMode plate reader. Because the Alamar Blue signal is dependent on the total cell number, the differences in cell adhesion properties between PLLA−PMCL−PLLA and the controls were expected to cause errors in evaluating their relative cytotoxicity. To address this issue, the Alamar Blue assay was also performed for samples cultured for 4 hours as a normalization reference, and a medium change was conducted at 4 hours for the samples to be evaluated at 24 hours (the cells not adhered to material surfaces at 4 hours would be removed during the medium change). The Alamar Blue signal at 24 hours normalized to that at 4 hours for each material reveals the increase in the cell number between 4 and 24 hours. A higher value of cell number increase represents a lower level of material cytotoxicity. The experiments were performed in triplicate, and statistical analysis was conducted by unpaired t-tests.

A3.2.4 Cytotoxicity Evaluation of Polymer Hydrolysis Products

The cytotoxicity of sodium 6-hydroxy-4-methylcaproate (the hydrolysis product of PMCL) and sodium 6-hydroxycaproate (the hydrolysis product of PCL) was evaluated by determining the median toxic dose, TD_{50} (the concentration resulting in 50% cell viability), from a dose−response curve of cell viability as previously reported.[262] Fibroblasts were seeded in a 96 well cell culture plate at a density of 5000 cells per well and cultured for 24

hours. The culture medium was then replaced with serum-free DMEM containing the test compound at various concentrations, followed by an additional incubation in the tissue culture incubator for 24 hours. A control in which no compound was added in serum-free DMEM was performed. Cell viability was evaluated using the Alamar Blue assay, and the fluorescence intensity of each sample containing a test compound was normalized to that of the control. A dose−response curve of normalized cell viability was plotted and the TD_{50} was determined using GraphPad Prism 8. The experiments were performed in triplicate.

A3.3 Results and Discussion

A3.3.1 Cytotoxicity of Polymer Films

The cytotoxicity of PLLA−PMCL−PLLA was first evaluated using a qualitative live/dead staining assay for fibroblasts cultured on polymer films for 24 hours. Two well-known noncytotoxic materials, PCL[220] and standard TCPS,[263] were investigated as controls. Fluorescent images revealed that the cells cultured on PLLA−PMCL−PLLA films were highly viable, as many green cells were observed and the ratio of green to red cells was large (Figure 57a). In addition, the spread morphology was indicative of healthy cells and good cell adhesion,[264] similar to the cells cultured on TCPS (Figure 57c). The cells cultured on PCL films showed a slightly rounded morphology (Figure 57b). These results suggest that PLLA−PMCL−PLLA is noncytotoxic.

The cytotoxicity of PLLA−PMCL−PLLA was further quantitatively evaluated using the AlamarBlue assay for fibroblasts cultured on polymer films for 24 hours, with PCL and TCPS as controls. To reveal different cell adhesion properties between the three materials and eliminate their effects on cytotoxicity evaluation, the AlamarBlue assay was also performed for cells cultured for 4 hours post-seeding on each material. For the samples

evaluated at 24 hours, a medium change was performed at 4 hours to remove nonadherent cells, so that the AlamarBlue signal at 24 hours normalized to that at 4 hours represents the increase in the cell number between 4 and 24 hours. The number of cells adhered on PLLA−PMCL−PLLA at 4 hours is smaller than that on PCL or TCPS, but the increase in the cell number between 4 and 24 hours is greater than that on PCL and similar to that on TCPS (Figure 58). Because a greater increase in the cell number indicates a lower level of cytotoxicity, these results suggest that PLLA−PMCL−PLLA is similar to TCPS and better than PCL in terms of cytocompatibility.

A3.3.2 Cytotoxicity of Polymer Hydrolysis Products

The dose−response curves of cell viability when exposed to sodium 6-hydroxy-4-methylcaproate and sodium 6-hydroxycaproate, the respective hydrolysis products of PMCL and PCL, were similar (Figure 59). The TD_{50} (median toxic dose) values determined from these curves were 179.1 ± 2.2 mM for sodium 6-hydroxy-4-methylcaproate and 171.7 ± 1.9 mM for sodium 6-hydroxycaproate. PCL has been used in many FDA-approved, implantable medical devices.[54] The hydrolysis product is sodium 6-hydroxycaproate[220] and has been reported to be noncytotoxic.[221] Sodium 6-hydroxy-4-methylcaproate has a slightly higher TD_{50} than that of sodium 6-hydroxycaproate suggesting that the PMCL hydrolysis product is also noncytotoxic and MCL-based polymers could potentially be used for implantable medical devices. Importantly, the TD_{50} value of sodium 6-hydroxy-4-methylcaproate is approximately four times higher than that of lactic acid (46.18 mM),[265] the hydrolysis product of PLA. PLA is a widely recognized sustainable and degradable plastic, and it has been used in FDA-approved implantable medical devices.[53] The

significantly higher TD_{50} value of sodium 6-hydroxy-4-methylcaproate as compared with the hydrolysis product of PLA further confirms the excellent cytocompatibility of PMCL.

A3.4 Conclusions

Overall, this work has demonstrated the PLLA-PMCL-PLLA copolymers and the hydrolysis products of PMCL are noncytotoxic. This has important implications for use of this material as a compostable material. Additionally, PMCL based elastomers may be potential candidates as sustainable polymers for medical device applications based on these results.

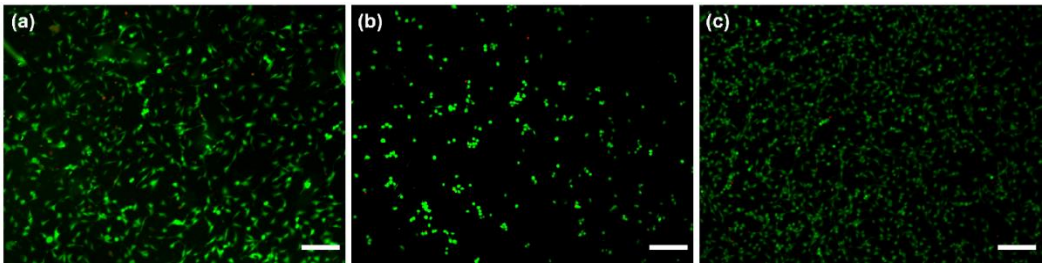

Figure 57. Live/dead assay for NIH 3T3 fibroblasts cultured for 24 hours on (a) PLLA−PMCL−PLLA, (b) PCL, and (c) TCPS. Green and red represent live and dead cells, respectively. Scale bar is 200 μm.

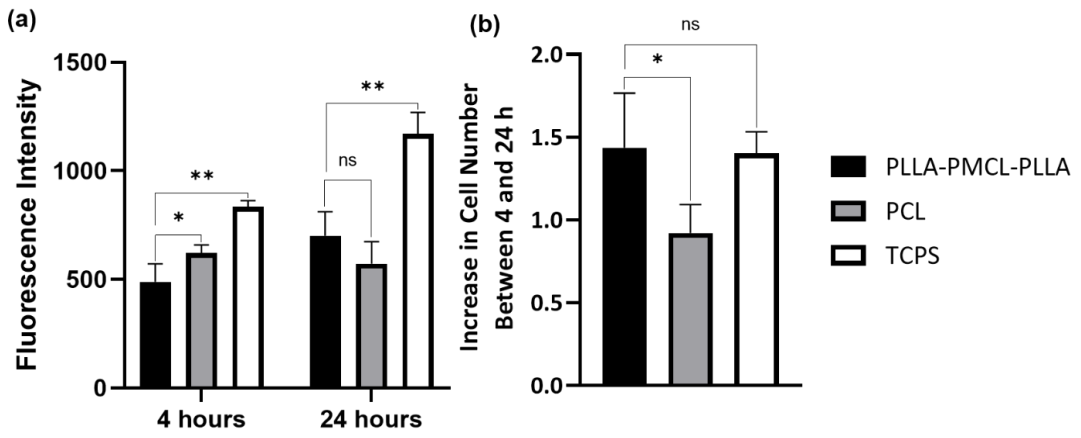

Figure 58. AlamarBlue assay for fibroblasts cultured on PLLA−PMCL−PLLA, PCL, and TCPS. (a) AlamarBlue fluorescence intensity measured at 4 and 24 hours post-cell seeding. (b) Increase in the cell number between 4 and 24 hours as calculated by normalizing the AlamarBlue signal at 24 hours to that at 4 hours. Error bars represent standard deviations, n = 3. **p-value < 0.01, *p < 0.1, and ns = not significant.

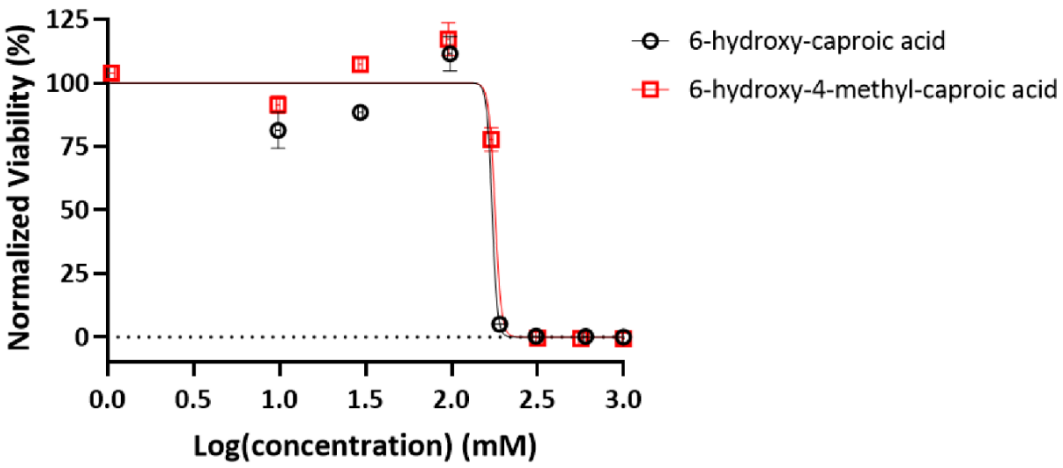

Figure 59. Dose–response curves of cell viability when exposed to the hydrolysis products of PMCL (red squares) and PCL (black circles). The cell viability is normalized to a nontreated control. The curves represent the nonlinear regression analysis by GraphPad Prism 8 to determine the TD_{50} value. Error bars represent standard deviation, n = 3.